FUNDAMENTAL GROWTH PROCESSES ON DIFFERENT GALLIUM ARSENIDE SURFACES IN METAL-ORGANIC VAPOR PHASE EPITAXY

vorgelegt von
Dipl.-Phys. Markus Pristovsek
aus Berlin

Vom Fachbereich 4 (Physik)
der Technischen Universität
zur Verleihung des akademischen Grades
DOKTOR DER NATURWISSENSCHAFTEN
genehmigte Dissertation

Promotionsausschuss:
Vorsitzender: Prof. Dr. Andreas Knorr
Berichter: Prof. Dr. Wolfgang Richter
Berichter: Prof. Dr. Karl Jacobi

Tag der wissenschaftliche Aussprache: 1.11.2000

BERLIN 2001
D83

FUNDAMENTAL GROWTH PROCESSES ON DIFFERENT GALLIUM ARSENIDE SURFACES IN METAL-ORGANIC VAPOR PHASE EPITAXY

by

Markus Pristovsek

In this work the homo-epitaxial growth on different (hkl) surfaces of gallium arsenide in Metal-Organic Vapor Phase Epitaxy (MOVPE) was investigated in-situ by Reflectance Anisotropy Spectroscopy (RAS). The RAS measurements were correlated to other electron based surface science measurements on samples transferred from a special MOVPE system without contamination into in an Ultra-High Vacuum (UHV) system in order to interpret the in-situ RAS spectra.

First, the well-ordered reconstructions on each of the surfaces were measured, and many new reconstructions were discovered. Then arsenic desorption experiments were performed, and reaction rates and activation energies were determined. The high-index surfaces with the largest tilt to the (001) surface had the lowest activation energies and the highest reaction rates for arsenic desorption. Probably the bonds are more strained on the high-index surfaces, and thus the arsenic comes off more easily.

On the (113), ($\overline{1}13$) and (001) surfaces RAS spectra were taken also during growth at different temperatures and with different tri-methyl gallium (TMGa) and AsH_3 partial pressures. The RAS spectra were compared to each other. For usual growth parameters three different types of RAS spectra, called phases, were found. On the (001) surface, at very low V/III ratios and lower temperatures using TMGa – conditions important for intrinsic high carbon doping – a fourth phase was observed. The phase boundaries mainly depended on temperatures and partial pressures, but not on surface orientation. Only the use of tri-ethyl gallium (TEGa) instead of TMGa shifted the phase boundaries on the (001) surface about 120-200 K to lower temperatures. Thus the surface during growth depends mainly on the precursor chemistry.

Therefore, the adsorption of TEGa was compared to the one of TMGa. Exposing the (001) surface to TMGa at low temperatures causes the same RAS spectra as during growth at very low V/III ratios. This reconstruction is methylene terminated and very inert to further TMGa adsorption. However, with TEGa no such adsorbate terminated surface was found.

During growth at low V/III ratios with TMGa, three different regimes of carbon incorporation were observed. At very low V/III ratios below one the carbon incorporation is always around $3 \cdot 10^{19}\,\mathrm{cm}^{-3}$. At high V/III ratios the carbon doping level is constant too, but it depends on growth temperature. However, in between a power law dependence of the carbon incorporation on the V/III ratio was measured, and the surfaces were relatively rough. This behaviour was successfully explained by a change of the reconstruction of the growing surface between a methylene terminated surface at very low V/III ratios and a methyl terminated surface at higher V/III ratios.

Parts of this work have been published in:

K. Ploska, J.-T. Zettler, W. Richter, F. Reinhardt, J. Rumberg, M. Pristovsek, M. Zorn, D. Westwood, R. Williams. *Surface processes before and during growth of GaAs(001)* J. Crystal Growth **145** (1994) 44–52

J.-T. Zettler, J. Rumberg, K. Ploska, K. Stahrenberg, M. Pristovsek, W. Richter, M. Wassermeier, P. Schützendüwe, J. Behrend, L. Däweritz. *Reflectance Anisotropy Oscillations during MOCVD and MBE Growth of GaAs (001)* phys. stat. sol. (a) **152** (1995) 35–47

K. Ploska, M. Pristovsek, W. Richter, J. Jönsson, I. Kamiya, J.-T. Zettler. *Metalorganic Vapour Phase Epitaxial Growth on Vicinal GaAs (001) Surfaces Studied by Reflectance Anisotropy Spectroscopy* phys. stat. sol. (a) **152** (1995) 49–59

J.-T. Zettler, T. Wethkamp, M. Zorn, M. Pristovsek, C. Meyne, K. Ploska, W. Richer. *Growth oscillations with monolayer periodicity monitored by ellipsometry during MOVPE of GaAs (001)* Appl. Phys. Lett. **67** (1995) 3783–3785

J.-T. Zettler, W. Richter, K. Ploska, M. Zorn, J. Rumberg, C. Meyne, M. Pristovsek. *Real time diagnostics of semiconductor surface modifications by RAS* in *Semiconductor Characterization – Present Status and Future Needs* Ed. by W. Bullis, D. Seiler, A. Diebold (AIP Press Woodbury NY 1996) 537–543

J.-T. Zettler, M. Pristovsek, T. Trepk, A. Shkrebtii, E. Steimetz, M. Zorn, W. Richter. *Response of the surface dielectric function to dynamic surfaces modifications: application of reflectance anisotropy spectroscopy and spectroscopic ellipsometry* Thin Solid Films **313-314** (1998) 537–543

M. Pristovsek, H. Menhal, J.-T. Zettler, T. Schmidtling, N. Esser, W. Richter, C. Setzer, J. Platen, K. Jacobi. *Reconstructions of the GaAs (113) surface* J. Crystal Growth **195** (1998) 1–5

H. Hardtdegen, M. Pristovsek, H. Menhal, J.-T. Zettler, W. Richter, D. Schmitz. *in-situ characterization of GaAs growth in nitrogen atmosphere during MOVPE: a comparison to hydrogen atmosphere* J. Crystal Growth **195** (1998) 211–216

M. Pristovsek, H. Menhal, T. Schmidtling, N. Esser, W. Richter. *Comparative study of the GaAs (113), (115), (001), (11$\bar{5}$), (11$\bar{3}$), and (110) surfaces by atomic force microscopy, low energy electron diffraction, and reflectance anisotropy spectroscopy* Microelectronics Journal **30** (1999) 449–453

M. Pristovsek, T. Trepk, M. Klein, J.-T. Zettler, W. Richter. *Dynamic Study of the Surfaces of (001) Gallium Arsenide in Metal-organic Vapour Phase Epitaxy during Arsenic Desorption* J. Appl. Phys. **87** (2000) 1245–1250

M. Pristovsek, F. Poser, J.-T. Zettler, W. Richter. *Diffusion of Ga on GaAs (113) in [1-10] direction in MOVPE* Appl. Surf. Sci. **166** (2000) 433–436

M. Pristovsek, B. Han, J.-T. Zettler, W. Richter. *in-situ Investigation of GaAs (001) Intrinsic Carbon p-Doping in Metal-organic Vapour Phase Epitaxy* J. Crystal Growth **221** (2000) 194–155

Contents

Preface

Crystal growth has fascinated mankind for a long time. Order that originates from the chaos of solutions or melts, this was nothing else than a reflection of the creating power of god. And if the alchemists could make crystals, which were rarely found in nature, surely they could find the philosopher's stone?

Today the growth of crystals is much more prosaic, and also better understood. Though the optimization of the epitaxy (ordered growth on ordered seed crystals) of semiconductor layers for device structures, as well as the preparation, has still some alchemical traces in it ("A growth interruption of six seconds makes the dot's luminescence much brighter ... ")

Undoubtedly there has been huge progress in understanding epitaxy in the last fifty years, when surface science on an atomic scale first became possible. And the "end of surface science" is still far away, as every new answer seems to produce two more questions. Additionally, there are many aspects or missed phenomena which are waiting to be rediscovered, as quantum dots and, more recently, nitride semiconductors have proven.

The growing knowledge of the growth process owes a good part to the development of new methods to measure at atomic scales. For a long time only indirect or diffraction based methods were available such as LEED (Low Energy Electron Diffraction), but nowadays the imaging of a real surface using STM (Scanning Tunneling Microscope) is quite a normal task. Another important tool was the development of surface sensitive optical methods such as RAS (Reflectance Anisotropy Spectroscopy) for surface science even in growth environments used for production, where traditional surface science tools failed to work.

The tremendous success of semiconductor science has made computers smaller and faster. So fast, that in recent years computational surface science has achieved huge success in doing simulations of realistic systems of 100 or more atoms. Even more important, the results of these calculations are getting closer to the experiments. The cooperation between calculations and experiments has been and certainly will be very fruitful. This is a big step forward towards further understanding of basic growth mechanisms themselves, because theory can give insight into details, that are simply not accessible to experiments.

This work bases also on many works at the end of the 60s, when controlled epitaxy was first achieved. At that time a huge parameter space had to be scanned, i.e. different temperatures, precursors, partial pressures, substrates and their orientations, and last but not least the different growth methods themselves were checked. Today, these old results have received interest again, as the quest for higher carrier confinement in low dimensional structures have meant that different crystal orientations (high index surfaces) and extreme growth parameters are tried again. Many of these old results have been understood only recently, as it is now known that semiconductor surfaces spontaneously rearrange themselves (forming reconstructions) to minimize dangling bonds and surface energy.

The aim of this work is to explain the homo-epitaxy of gallium arsenide in Metal-Organic Vapor Phase Epitaxy (MOVPE) on the (001) and several high-index surfaces with respect to the current state of knowledge of the MOVPE process.

I

Surfaces and Growth

1 Static Crystal Surface

1.1 The Surface

The growth of any single crystal starts with a seed. For epitaxy of two-dimensional layers, the seed crystal is called the substrate. The usual substrate is a single crystal, which is cut along a high symmetry axis and has a polished surface. Because it is a real surface, it is misoriented to some degree referring to the intended cutting direction. Thus wide terraces appear, divided by mono-atomic steps to compensate for the misorientation.

An intentionally misoriented surface is called a *vicinal* surface, in contrast to an ideally flat *exact oriented* surface. The distance of steps, called terrace width L, depends only on the misorientation angle α and the lattice constant along the surface (a_0):

$$L(\alpha, a_0) = \frac{a_0}{\tan \alpha}. \tag{1.1}$$

For the vicinal (001) GaAs surface the resulting terrace width is plotted in figure 1.1.

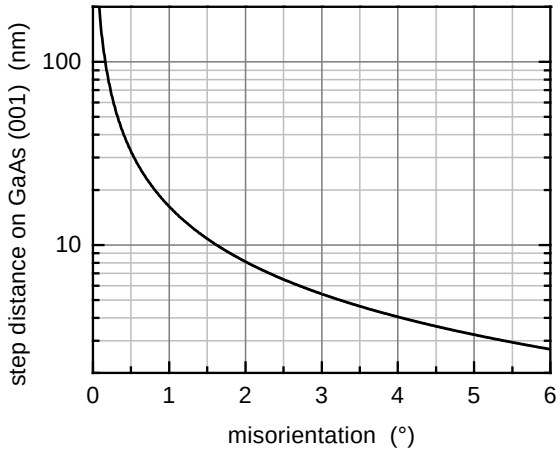

Figure 1.1: *Step distance on (001) GaAs as a function of the angle of misorientation.*

Figure 1.2 shows the surface of an ideal single crystal with a monoatomic step. Each of the boxes corresponds to a monomer, i.e. a single constituent of the crystal. Besides the ideal surface sites five other sites with larger numbers of near neighbors exist. In table 1.1 the number of near neighbors for these sites on a cubic (001) surface are listed.

Depending on the number of near neighbors the binding energy changes. A monomer, caught by a surface hole or a step hole, is bound very tightly, in contrast to a monomer that just sits on an ideal surface site. For this reason any holes are immediately filled at the beginning of growth. Even more, holes are very unlikely to be formed during growth in great numbers, because a lot of atoms must be previously attached to other sites in exactly the right order. Thus, on real surfaces holes appear only rarely and can be neglected.

The number of nearest neighbor sites depends strongly on crystal symmetry and orientation of the surface. For example on a cubic (111) surface a monomer has three nearest neighbor bonds, whereas on the cubic surface, in figure 1.2, a monomer has just a single near neighbor.

Figure 1.3 shows all important high-index surfaces of the face centered cubic gallium arsenide (001) crystal, which are perpendicular to the $[1\bar{1}0]$ direction. Many different surfaces exist.

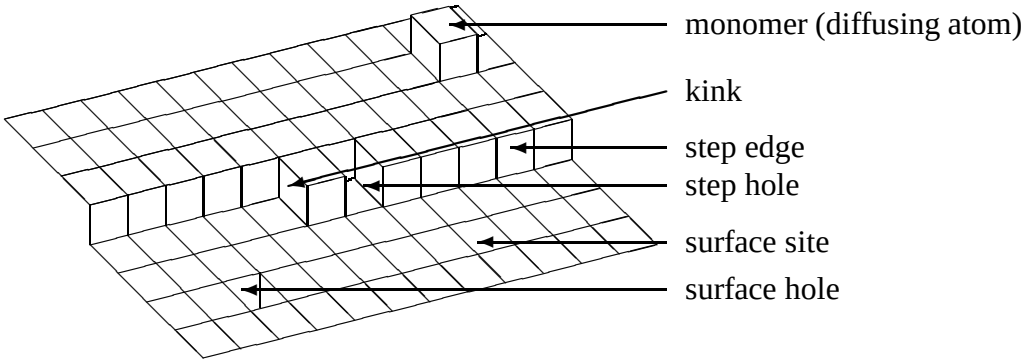

Figure 1.2: *The different sites for an atom on a surface.*

	site	neighbor next	neighbor 2nd	binding strength
1.	monomer	1	8	weak
2.	along a monomer	2	8	
3.	step-edge	2	10	
4.	kink	3	10	↓
5.	step hole	4	10	
6.	surface hole	5	12	strong

Table 1.1: *Number of nearest neighbors on a cubic (001) surface of different surface sites.*

In this work the (001), (113), (115), (110), $(\overline{113})$ and $(\overline{115})$ will be investigated. Therefore some notations have to be made in order to prevent confusion.

It is obvious from figure 1.3 that for a binary compound crystal of A and B constituents (like gallium arsenide) the $(11\underline{1})$ and $(\overline{111})$ surfaces (and hence also the (113) and $(\overline{113})$ surfaces) are not identical. A $(\overline{111})$ surface corresponds to a (111) surface, on which all A atoms are exchanged by B atoms. On the (111) surface an A atom has three back-bonds and only one bond forward. Hence, it is bound very tightly to this surface and the (111)

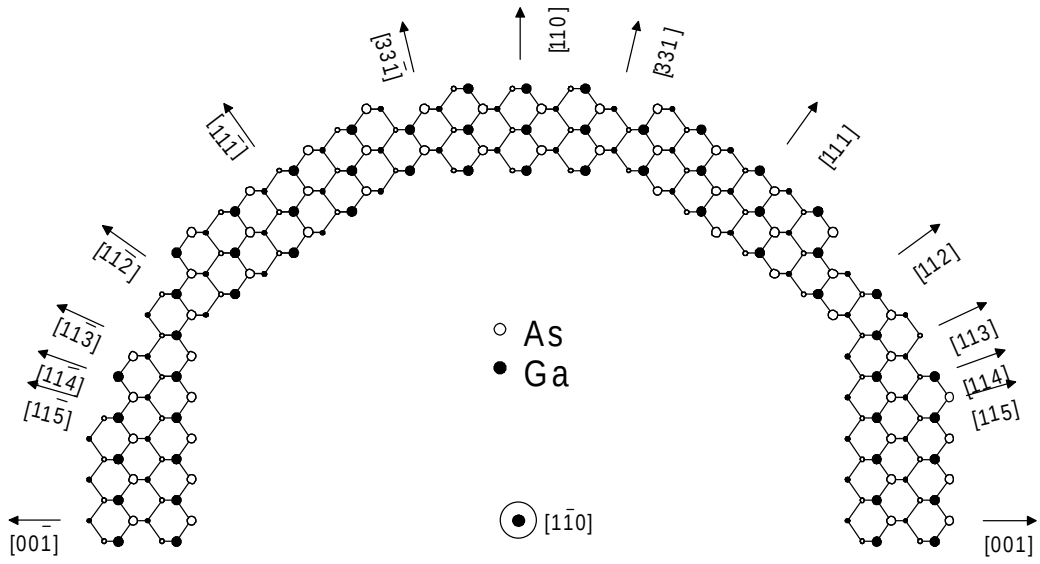

Figure 1.3: *High-index surfaces perpendicular to the [1$\bar{1}$0] direction of gallium arsenide.*

surface is expected to be terminated more or less completely by A atoms. The situation is reversed on the $(11\bar{1})$ (or $(\bar{1}\bar{1}\bar{1})$) surface, where it is terminated by B atoms. For this reason the (111) surface is often called "(111)A" and the $(\bar{1}\bar{1}\bar{1})$ "(111)B" or, even wrong, "$(\bar{1}\bar{1}\bar{1})$B". (For gallium arsenide A is gallium, B is arsenic, thus there is also the variation of (111)Ga and (111)As or $(\bar{1}\bar{1}\bar{1})$As.) However, this denomination is neither physically correct (as for GaN where a $(\bar{1}\bar{1}\bar{1})$=(111)B=(111)N is gallium terminated), nor do the (111)A and (111)B surfaces behave nearly as identically as suggested. Therefore, the correct naming scheme of (111) and $(\bar{1}\bar{1}\bar{1})$ is used throughout this work.

Additionally, throughout this work the following convention for brackets is used: square brackets name [hkl] directions, round ones name (hkl) surfaces, and all equivalent surfaces have the form $\{hkl\}$. If more than one surface is present on a sample, the additional surfaces are called facets and are also designated (hkl) or $\{hkl\}$. Equivalent surfaces to $\{\bar{h}kl\}$ on GaAs are the $(\bar{h}kl)$, $(h\bar{k}l)$, $(hk\bar{l})$ and $(\bar{h}\bar{k}\bar{l})$ surfaces; and for $\{hkl\}$ are $(hk\bar{l})$, $(\bar{h}kl)$, $(h\bar{k}l)$ and $(\bar{h}\bar{k}\bar{l})$. Note that the (110) and the $(1\bar{1}0)$ surfaces are identical, since the (110) cannot be mathematically distinguished from the $(\bar{1}10)$=$\{110\}$ surface. Therefore, simply for mathematical reasons only a single type of $\{110\}$ surface exists.

1.2 Surface Reconstruction

So far no assumption about the inner structure of a crystal surface was made. However, many different kinds of structures on a crystal surface can be found. In the most simple model, the atoms on the surface are at the same positions as in the bulk; therefore, such a surface is called *truncated bulk structure*. Indeed, a truncated bulk structure is found on the surface of many materials like metals, rare gas crystals, or crystals of complex molecules, in all cases when the binding forces are small or the components forming the crystal are large.

However, on many ionic or covalent crystals the binding energies are quite high. Usually the surfaces of such crystals deviate from a truncated bulk structure, and the atoms rearrange themselves to lower the surface energy. Usually the symmetry (size of surface unit mesh) or the stoichiometry of the surface is changed with respect to a truncated bulk structure. This rearrangement is called *reconstruction*. Since a surface can form several reconstructions, a naming scheme is used based on the size of the surface unit mesh for the main axes of the surface compared to the bulk. For example (2x4) on a (001) GaAs surface means two times the size along $[1\bar{1}0]$ and four times along [110]. If several reconstructions with the same symmetry exist, they are differentiated by a Greek letter. Additional information may be encoded in another letter, like p (primitive), c (centered) or d (disordered).

The driving force for the appearance of reconstructions is the minimization of the surface free energy. In a crystal usually only bonding orbitals are filled by sharing electrons with neighboring atoms, so that every atoms "feels" eight electrons. In the case of GaAs, the gallium can contribute three, and the arsenic five electrons. Since there are four bonds on any atom in the fcc structure, one can simply say that gallium contributes $\frac{3}{4}$ electron and arsenic $\frac{5}{4}$ to each bond. On a surface some of these orbitals have unpaired electrons (*dangling bonds*). These are energetically very unfavorable and therefore chemically very active. Strictly speaking the dangling bonds which correspond to bonding orbitals should be filled and the ones that correspond to anti-bonding orbitals should be empty.

On most III-V and II-VI semiconductor surfaces (e.g. GaAs or ZnSe) there is a simple criteria for which dangling bonds are bonding and anti-bonding: Group V(VI) dangling bonds correspond to bonding orbitals (they want to be filled), while group III(II) dangling bonds correspond to anti-bonding orbitals (they want to get rid of their electrons). This means for GaAs gallium dangling bonds are empty and arsenic dangling bonds are filled.

This is the essence of the so-called *electron counting rule* [1]. Usually reconstructions that satisfy the electron counting rule are more stable than the ones that do not.

The easiest way for a surface to fulfill this rule, i.e. to empty all anti-bonding orbitals, is to redistribute the electrons of the dangling bonds. Such a surface termination with only redistributed electrons is called *relaxation*. On a relaxed surface the electrons usually are redistributed between next neighbor atoms. However, a surface relaxation is often forbidden, either for geometrical reasons, or simply due to a lack of electrons or empty bonding orbitals. Then the atoms must rearrange themselves to change the total number of dangling bonds. The atoms must leave their normal places to form a reconstruction, which may contain vacancies, single ad-atoms, dimers, or rarely also trimers and tetramers. (A dimer denotes a bond between two atoms on the surface, which is different compared to the bulk bonding arrangement.)

Of course the stability of a single crystal surface depends not only on the right number of electrons per unit mesh. Other factors like strain or the chemical environment have to be taken into account too. All these requirements together are reflected by the free energy of a surface. A real surface has to minimize its free surface energy. For different conditions different reconstructions can meet this criteria.

On compound crystals the concentrations of the compounds at the surface have to be considered too. This simply means that with arsenic rich conditions a reconstruction is favored which incorporates more arsenic atoms.

1.2.1 Chemical Potential

The concentration of the compounds on the surface can be characterized by the chemical potential μ. In the case of gallium arsenide there are three chemical potentials to be taken into account. These are the one of bulk GaAs $\mu_{GaAs_{bulk}}$, of arsenic μ_{As} and of gallium μ_{Ga} at the surface. The first is constant, while the latter two can change on the surface. Their upper limit is given by the chemical potential of a bulk of the component, e.g. $\mu_{As_{bulk}} > \mu_{As}$, otherwise an arsenic crystal would form (or gallium droplets at the other extreme). The sum of $\mu_{Ga} + \mu_{As}$ must yield $\mu_{GaAs_{bulk}}$, otherwise arsenic or gallium would be evaporated from the GaAs crystal.

Since $\mu_{Ga_{bulk}}$ and $\mu_{As_{bulk}}$ are constant, it is convenient to use the difference of the μ to their bulk values:

$$\begin{aligned} \mu_{Ga} < \mu_{Ga_{bulk}} \quad &\Rightarrow \quad \Delta\mu_{Ga} := \mu_{As} - \mu_{As_{bulk}} < 0 \\ \mu_{As} < \mu_{As_{bulk}} \quad &\Rightarrow \quad \Delta\mu_{As} := \mu_{As} - \mu_{As_{bulk}} < 0 \end{aligned}$$

Applying the above discussed limits to the various μ, one obtains:

$$\begin{aligned} \mu_{GaAs_{bulk}} &= \mu_{As} + \mu_{Ga} < \mu_{As_{bulk}} + \mu_{Ga_{bulk}} \\ \mu_{GaAs_{bulk}} - (\mu_{As_{bulk}} + \mu_{Ga_{bulk}}) &= \mu_{As} - \mu_{As_{bulk}} + \mu_{Ga} - \mu_{Ga_{bulk}} < 0 \\ \mu_{GaAs_{bulk}} - (\mu_{As_{bulk}} + \mu_{Ga_{bulk}}) &= \Delta\mu_{As} + \Delta\mu_{Ga} < 0 \end{aligned} \tag{1.2}$$

The term $\mu_{GaAs} - (\mu_{As_{bulk}} + \mu_{Ga_{bulk}})$ is simply the energy of formation of gallium arsenide $-\Delta H$. Calculations and measurements suggest a value of (0.80 ± 0.15) eV for ΔH. Therefore $\Delta\mu_{As}$ and $\Delta\mu_{Ga}$ are restricted to small range:

$$\begin{aligned} -\Delta H_{GaAs} &\leq \Delta\mu_{As} < 0 \qquad \text{or} \\ -\Delta H_{GaAs} &\leq \Delta\mu_{Ga} < 0 \end{aligned} \tag{1.3}$$

Since $\Delta\mu_{Ga} + \Delta\mu_{As} = -\Delta H_{GaAs}$ it is enough to consider either $\Delta\mu_{Ga}$ or $\Delta\mu_{As}$. For example, $\Delta\mu_{Ga} \approx 0$ denotes gallium rich conditions, i.e. the onset of gallium droplet formation. $\Delta\mu_{Ga} \approx -\Delta H$ corresponds to arsenic rich conditions.

How could a reconstruction respond to arsenic rich conditions? Certainly a reconstruction containing excess gallium (a gallium rich reconstruction) is unfavorable, as a reconstruction containing a lot of arsenic atoms seems better suited. Indeed, the free energy of a reconstruction depends on the chemical potential, as it can be seen in figure 1.4.

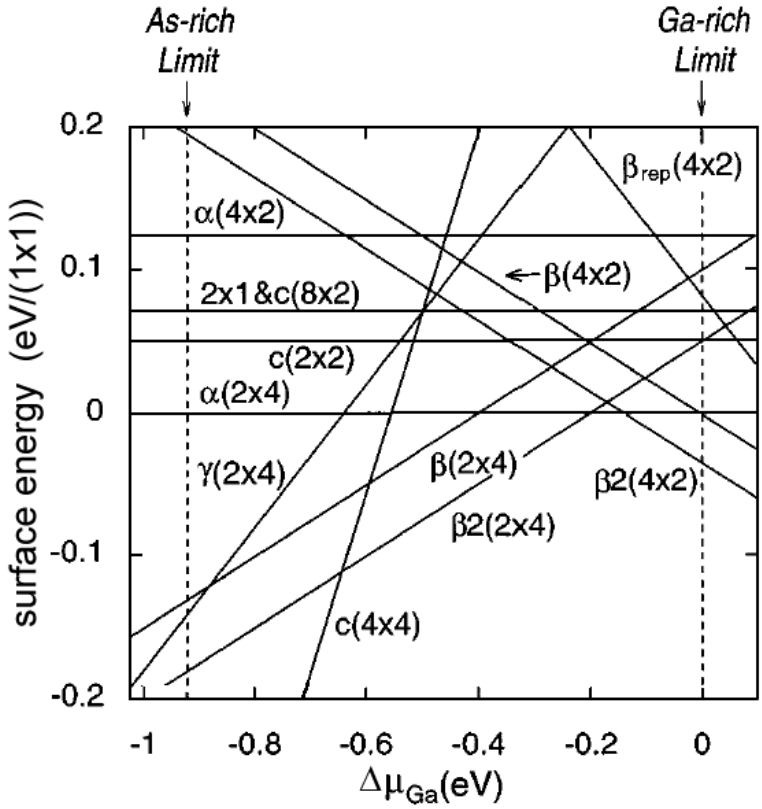

Figure 1.4: *Calculation of total surface energies of several reconstructions on (001) gallium arsenide [2] using DFT-LDA.*

Figure 1.4 shows the calculated total energy of several reconstructions on a gallium arsenide (001) surface as a function of the chemical potential of gallium $\Delta\mu_{Ga}$. Only the reconstruction with the lowest energy at a given chemical potential is stable. For gallium rich conditions the gallium rich $\beta 2$(4x2) reconstruction is the lowest energy structure, with more arsenic rich conditions α(2x4), $\beta 2$(2x4), and finally the very arsenic rich c(4x4) reconstruction are the most stable, lowest energy reconstructions.

1.3 Equilibrium Crystal Shape

The free energy of a reconstruction is important to determine the stability of an actual surface, because under certain conditions some surfaces tend to spontaneously form structures like grooves, pyramids or holes, whose sidewalls are high-index surfaces. These sidewall surfaces are called facets.

The simplest system with facets has three surfaces, the flat surface A and two adjacent facets B and C (fig. 1.5). Facet B (C) is tilted by an angle β (γ) with respect to the flat surface

A. The area coverage of facet B (C) projected on A is called σ_B (σ_C). Since the facets are tilted, their real areas are given by $\frac{\sigma_B}{\cos\beta}$ ($\frac{\sigma_C}{\cos\gamma}$). Thus the total energy of this surface is:

$$E_{tot} = E_A\sigma_A + E_B\frac{\sigma_B}{\cos\beta} + E_C\frac{\sigma_C}{\cos\gamma}. \tag{1.4}$$

If the starting surface is flat ($\sigma_A = 1$) then every step up to a facet B must be followed by a step down with a facet C (as seen in fig. 1.5).

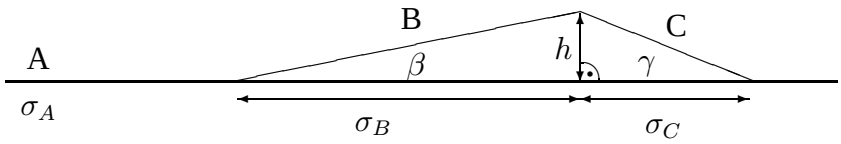

Figure 1.5: *Geometry of the simplest facetted surface.*

Simple trigonometry yields the following equation:

$$\begin{aligned} h = \sigma_B\tan\beta &= \sigma_C\tan\gamma \\ \sigma_B\frac{\tan\beta}{\tan\gamma} &= \sigma\gamma. \end{aligned} \tag{1.5}$$

Putting equation (1.5) in (1.4) one finally ends up with

$$\begin{aligned} E_{tot} &= E_A\sigma_A + E_B\frac{\sigma_B}{\cos\beta} + E_C\frac{\sigma_B\frac{\tan\beta}{\tan\gamma}}{\cos\gamma} \\ E_{tot} &= E_A\sigma_A + E_B\frac{\sigma_B}{\cos\beta} + E_C\frac{\sigma_B\tan\beta}{\tan\gamma\cos\gamma}. \end{aligned} \tag{1.6}$$

The surface wants to minimize its energy E_{tot}. It is obvious that either the completely flat surface ($\sigma_A = 1, \sigma_b = 0$) possesses minimum energy, or the faceted surface which is covered completely by B and C ($\sigma_A = 0, \sigma_b + \sigma_C = 1$). Equation (1.5) can be used directly to calculate σ_B in this case:

$$\begin{aligned} \sigma_B + \sigma_C &= \sigma_B + \sigma_B\frac{\tan\beta}{\tan\gamma} = \sigma_B\left(1 + \frac{\tan\beta}{\tan\gamma}\right) = \sigma_B\left(\frac{\tan\gamma + \tan\beta}{\tan\gamma}\right) = 1 \\ \sigma_B &= \frac{\tan\gamma}{\tan\beta + \tan\gamma}. \end{aligned} \tag{1.7}$$

Finally equation (1.6) yields the following condition for faceting:

$$E_A > \left(\frac{\tan\gamma}{\tan\beta + \tan\gamma}\right)\left(\frac{E_B}{\cos\beta} + \frac{E_C}{\cos\gamma}\frac{\tan\beta}{\tan\gamma}\right). \tag{1.8}$$

If this equation is fulfilled, facets will appear. However, equation (1.8) tells us nothing about the shape of the resulting surface, i.e. if there are only two large areas of facet B and C or many smaller steps up and down. The final shape is determined by the elastic constants and the diffusion length, which will be discussed in section 3.1. Even more, if mass transport is very slow, faceting might not be observed on reasonable time scales, even though the surface is not stable from an equilibrium point of view.

On a more complex system like a sphere the same analysis can be done as for the simplest system. Also, by calculating the surface energies for several surfaces, the equilibrium shape

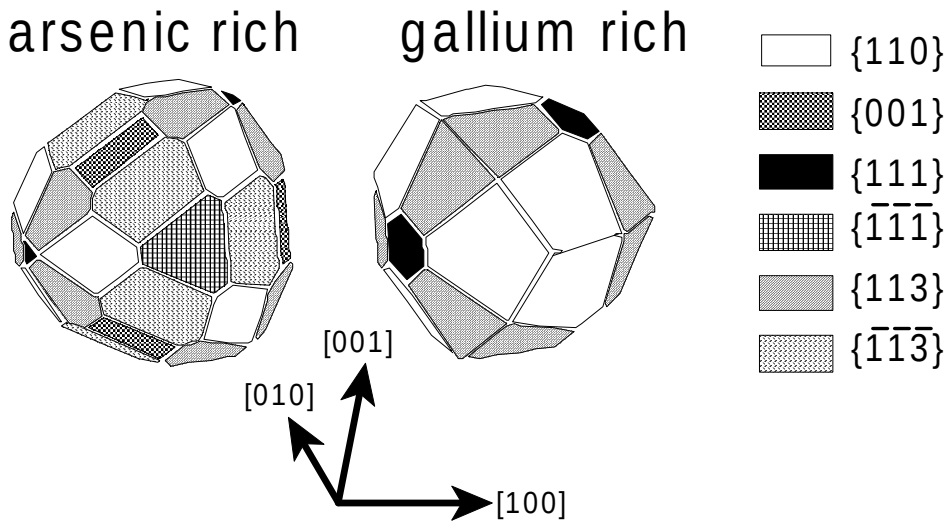

Figure 1.6: *Calculated equilibrium shape (*Wulff *construction) of a gallium arsenide crystal for arsenic rich and gallium rich conditions using DFT-LDA. Considered are* $\{113\}$*,* $\{112\}$*,* $\{111\}$*,* $\{110\}$ *and* $\{001\}$ *surfaces [3].*

of a crystal can be determined by a so-called *Wulff* construction. Figure 1.6 shows a Wulff construction of gallium arsenide for arsenic rich and for gallium rich conditions.

It is interesting to note, that in case of gallium arsenide many flat surfaces do not represent minimum surface energies at gallium rich conditions, i.e. it is energetically more favorable to form facets for these surfaces. The (001) surface is especially not stable at gallium rich conditions, even though reconstructions on gallium rich (001) surfaces like the (4x2) have been observed experimentally. This illustrates the fact that, if material transport is slow, a faceting might not be observed.

2 Growth Dynamics

So far only equilibrium processes were considered. However, the growth itself can lead to the formation of facets, even if the facets are not be stable in equilibrium.

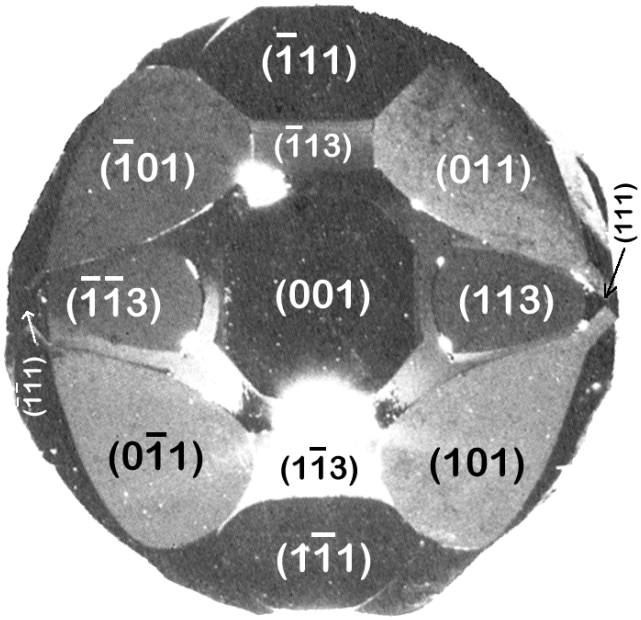

Figure 2.1: *Evolution of facets on a sphere of gallium arsenide after Cl-VPE growth [4]. Note that the* $\{111\}$ *facets have vanished. Their former position is indicated by arrows.*

Figure 2.1 shows facets which evolved during Chloride Vapor Phase Epitaxy (Cl-VPE) growth on a former GaAs hemisphere [4]. It looks very similar to figure 1.6. However, the underlying mechanism of facet formation is completely different. In figure 1.6 the final shape was only determined by the free energy of the different reconstructions, while in the case of growth the different growth rates on the facets themselves determine the shape. For example the (111) and ($\overline{1}\overline{1}\overline{1}$) facets have vanished, although according to figure 1.6 they are stable surfaces under all conditions. This disappearance is caused by the very high growth rate on the $\{111\}$ surfaces (see fig. 2.2). On the other hand, the size of all facets with low growth rates are increased.

Lower growth rates on some facets are possibly due to smaller sticking coefficients or higher activation energy for incorporation (in this case the atoms simply desorb before being incorporated). If a facet is much smaller than the diffusion length, the growth rate becomes additionally smaller, because atoms are lost by diffusion. (The fraction of atoms in relation to the size of the facets can be calculated by the BCF-theory, which will be discussed in section 3.2.2.)

The differences of growth rates can either enhance or diminish facets. An example is given in figure 2.3, a groove with facet sidewalls. When growth is initiated, and facet B is growing much faster than facet A. The groove is vanishing, simply for geometrical reasons.

What is the crucial difference for the growth rates? The simplest system is a large flat surface with a small adjacent facet. Instead of the free energy of the surface (as in the previous section 1.3), the growth rate R is now the crucial factor. The projected growth rate in the direction of the flat surface A of the facet B ($R_B \cos\beta$) has to be larger than the one on the initial surface R_A, otherwise no faceting will occur.

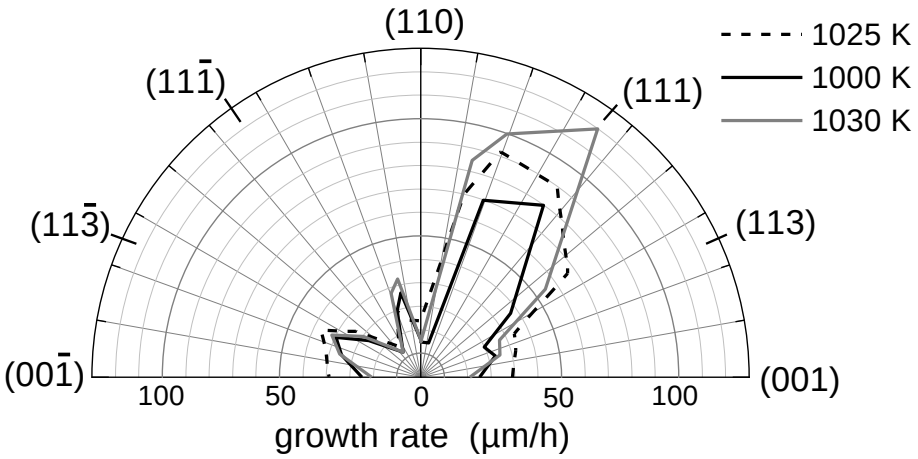

Figure 2.2: *Growth rates of different surfaces of gallium arsenide during Cl-VPE growth at different temperatures (1025 K [5], 1000 K and 1030 K [4]).*

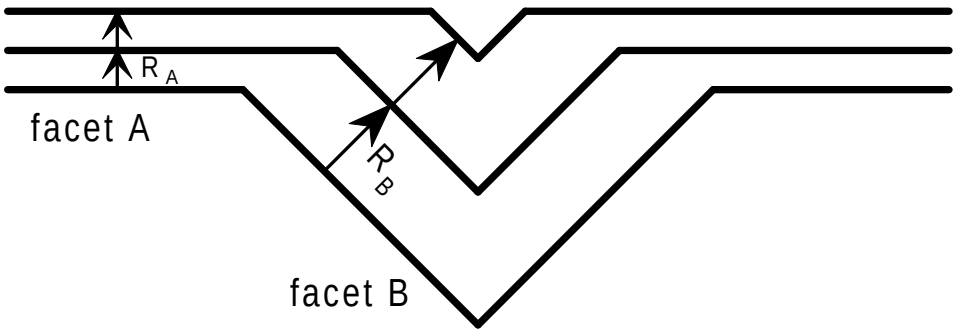

Figure 2.3: *Higher growth rate of the facet B leads to the disappearance of the groove.*

Figure 2.4 shows the geometry of this process. The area increase of facet B ($\Delta\sigma_B$) can be calculated from ΔR and β. ΔR is defined as:

$$\Delta R = R_{B\perp} - R_A = \frac{R_B}{\cos\beta} - R_A. \tag{2.1}$$

Thus the area increase is given by:

$$\Delta\sigma_B = \frac{\Delta R}{\tan\beta} = \frac{R_B - R_A\cos\beta}{\cos\beta\tan\beta} = \frac{R_B - R_A\cos\beta}{\sin\beta}. \tag{2.2}$$

The situation is reversed if $\beta < 0$ i.e. on a sphere. Then the slower growing facet will remain. And indeed in figure 2.1 the fast growing $\{111\}$ facets are not visible any more and the very slow growing $\{110\}$ facets are very large. If the growth had proceeded much longer the result would have been an octahedron of $\{110\}$ facets.

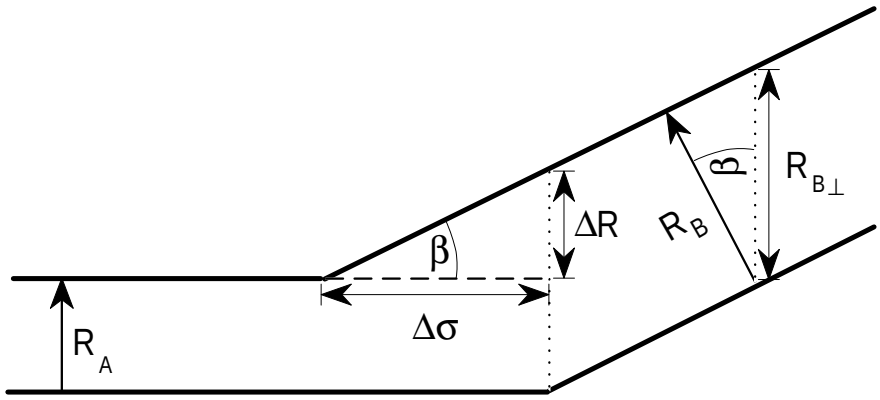

Figure 2.4: *Geometrical construction for the area increase during faceting.*

3 Growth Process on an Atomic Level

The growth process on any single crystal surface includes at least four steps which the monomers (i.e. the later constituents of the crystal) have to go through:

1. Adsorbtion Monomers adsorb at the surface.

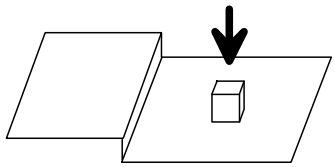

2. Diffusion Monomers move (diffuse) on the surface.

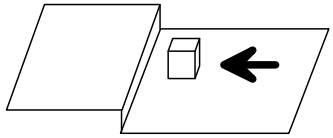

3. Desorption The longer the monomers diffuse on the surface, the higher is the probability for desorption.

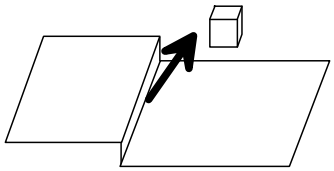

4. Incorporation If a monomer during diffusion reaches a site with a high number of next neighbors, it is incorporated.

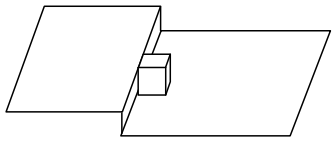

For the growth of GaAs these processes have to be considered for gallium and arsenic. For Metal-Organic Vapor Phase Epitaxy (MOVPE) growth the chemical nature of both the gallium and arsenic precursor have to be taken into account too.

Of the four steps, diffusion is the most important process from the technological point of view, since this process determines the size of structures or facets on the surface. Therefore, in the following sections, diffusion will be discussed in detail.

3.1 Diffusion

Diffusion on a solid surface is defined as the motion of particles on a discrete lattice. In this work diffusion means the motion of monomers on surfaces. A monomer is a constituent of the crystal; this might be atoms, clusters or (as in MOVPE) partly decomposed precursor molecules.

There are two parameters that characterize diffusion: the mean distance on the surface (diffusion length) and the average time needed to travel (velocity). Usually the latter is very short compared to the typical growth rates of a monolayer per second, and thus not of technological importance.

Diffusion length and velocity may differ for different directions, but it is usually assumed that diffusion along the different directions are independent. Consequently the problem can be treated as an one dimensional problem.

The basic assumption is that the monomers do a *random walk*: at every moment a monomer has a probability to move either a step in one direction or the other. Both probabilities are assumed equal. On average the monomer needs t seconds for a single step. Since the probabilities for steps in both directions are equal, the mean position of the monomer after a number of n steps is at the starting position x_0.

Then the probability for a monomer to be at the position x after the time $\tau = n\nu^{-1}$ (i.e. n steps, each taking the time $\frac{\tau}{n} = \nu^{-1}$) can be calculated directly (see e.g. [6] p.75):

$$P(x,\tau) = \frac{1}{\sqrt{2\pi D\tau}} \exp\left(-\frac{(x-x_0)^2}{2D\tau}\right), \tag{3.1}$$

where D denotes the diffusion coefficient $D = a_0^2\nu$ and a_0 the lattice constant.

This is identical to a Gaussian around x_0: $P(x) = \frac{1}{\sqrt{2\pi}\sigma} \exp\left(-\frac{(x-x_0)^2}{2\sigma^2}\right)$ with the standard derivation σ. Thus, the diffusion length is defined as the standard derivation σ of equation (3.1), and one obtains the *Einstein relation*:

$$\begin{aligned} \lambda = \sigma &= \sqrt{D\tau} \\ \lambda^2 &= D\tau. \end{aligned} \tag{3.2}$$

The dependence of the diffusion coefficient D on the temperature is determined by a simple activation energy approach (which is generally discussed in section 4). For each single step the monomer has to overcome the activation barrier of diffusion E_{Diff}:

$$D = D_0 \exp\left(-\frac{E_{Diff}}{k_B T}\right). \tag{3.3}$$

The average time for diffusion τ depends on the event that stops diffusion. If the event is nucleation then τ is equal to time of free diffusion, i.e. τ is proportional to the mean free path on the surface. The other possible event is desorption. In this case τ depends on the rest time on the surface. These two limits represent completely different growth regimes: nucleation limited diffusion and desorption limited diffusion.

A high growth rate (i.e. a high monomer density on the surface) certainly corresponds to nucleation limited diffusion. On the other hand, small growth rates and higher temperatures correspond to desorption limited diffusion. The smaller the incoming flux, and the higher the temperature, the more monomers can desorb before they nucleate. Figure 3.1 shows this schematically.

Note that in figure 3.1 for both extreme cases, when flux $J \to \infty$ and temperature $T \to 0$, or $J \to 0$ and $T \to \infty$, the diffusion length is vanishing, $\lambda \to 0$. However, the growth rate is infinite in the first case and zero in the second.

3.1.1 Nucleation Regime

In this regime the diffusion is limited by a nucleation event. A nucleation event is defined as two monomers meeting each other. The probability of nucleation events is higher with higher density of diffusing monomers, i.e. a higher flux of incoming monomers. A higher probability however, means a shorter time τ for diffusion. Thus, τ is inversely proportional to the monomer density on the surface:

$$\tau = \frac{N_A}{J}, \tag{3.4}$$

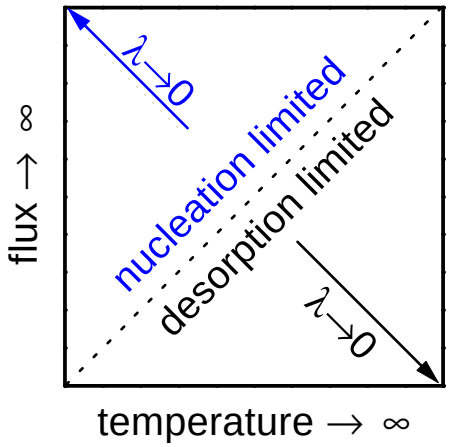

Figure 3.1: *Separation between nucleation limited and desorption limited diffusion.*

where N_A is the number of surface sites, which can also be a function of the temperature.

Putting equation (3.3) and (3.4) into (3.2) one obtains the following equation of the diffusion length λ:

$$\lambda(N_A, J, T) = \sqrt{D_0 \frac{N_A}{J}} \exp\left(-\frac{E_{Diff}}{2k_B T}\right). \tag{3.5}$$

The factor of 2 in the denominator of the exponent originates from the square root in equation (3.2): $\sqrt{D} = \sqrt{\exp(-E/k_B T)} = \exp(-E/2k_B T)$. Since the whole exponent is negative and the temperature is in the denominator, the diffusion length in the nucleation regime is increasing exponentially with temperature.

Extension to MOVPE Growth of GaAs

For binary compounds like GaAs during growth both species, arsenic and gallium, diffuse on the surface. In this case arsenic has a much higher vapor pressure, thus up to a thousand times more arsenic than gallium is offered to the surface. Therefore the effect of the arsenic is usually neglected ("arsenic is everywhere"). However, the effect of arsenic is definitely not negligible: the more arsenic is offered to the surface, the higher is the probability for a diffusing gallium atom to form a bond to an arsenic atom and to be incorporated. On the other hand, if more gallium is incorporated, less diffusing atoms populate the surface and thus the mean free path for diffusion increases.

Hence the free diffusion time τ is affected by the gallium flux J. In equation (3.4) τ is simply proportional to the number of gallium atoms on the surface. To take the arsenic into account the model can be extended by using the ratio between arsenic and gallium (V/III ratio) instead of the gallium flux, because the more arsenic is on a surface the lower is the effective density of unincorporated diffusing gallium atoms.

Obviously the parameter N_A, which gives the number of surface sites, in equation (3.4) must be changed too, since the V/III ratio is dimensionless. It is now called N_r and its dimension is that of a length:

$$\tau = \frac{N_A}{J} = N_r \cdot r_{V/III}. \tag{3.6}$$

τ can be inserted into equation (3.2) and an expression of the diffusion length is obtained:

$$\lambda(r_{V/III}, T) = \sqrt{D_0 N_r} \sqrt{r_{V/III}} \exp\left(-\frac{E_{Diff}}{2k_B T}\right). \tag{3.7}$$

There have been experimental evidence by diffuse X-ray scattering measurements (GIXD), which support the assumption of the above model, i.e. a square-root dependence of the diffusion length from the partial pressure of the gallium precursor on the GaAs (001) surface [7].

In most experiments the diffusion length λ is measured for certain growth parameters. Then the activation energy E_{Diff} can be simply obtained from an Arrhenius plot of λ measurements at different temperatures, but there is no way to directly measure the diffusion coefficient $\sqrt{D_0 N_r}$. The only way to determine the diffusion coefficient $\sqrt{D_0 N_r}$ is to transform equation (3.7) until it yields $\sqrt{D_0 N_r}$:

$$\sqrt{D_0 N_r}(\lambda, r_{V/III}, T) = \frac{\lambda}{\sqrt{r_{V/III}}} \exp\left(\frac{E_{Diff}}{2k_B T}\right). \tag{3.8}$$

Now the different $\sqrt{D_0 N_r}$ can be plotted in a diagram and the average diffusion coefficient $< \sqrt{D_0 N_r} >$ can be calculated.

3.1.2 Desorption Limited Regime

In the desorption limited regime a monomer desorbs if it has enough energy for desorption. Therefore for the residence time τ an activation energy approach is made:

$$\tau = \tau_0 \exp\left(\frac{E_{Des}}{k_b T}\right) \tag{3.9}$$

where E_{Des} is the activation energy for desorption.

At higher temperature the residence time τ decreases. Inserting equation (3.9), (3.3) into (3.2) the following dependence of the diffusion length λ is obtained:

$$\lambda(T) = \sqrt{D_0 \tau_0} \exp\left(\frac{E_{Des} - E_{Diff}}{2k_B T}\right). \tag{3.10}$$

It should be emphasized that E_{Diff} must be smaller than E_{Des}, otherwise monomers would desorb immediately instead of diffusing on the surface. This means $0 < E_{Des} - E_{Diff}$. Thus, the diffusion length λ is decreasing with increasing temperature.

3.2 2D Island Nucleation Growth versus Step-flow Growth

As mentioned earlier real surfaces have steps. Step-edges act as preferred incorporation sites, because at a step-edge a monomer is bound by a higher number of nearest neighbors than on the flat surface. The steps influence the incorporation behavior, as it will be discussed in the next sections.

3.2.1 2D Island Nucleation Growth

On an ideal surface without steps the growth proceeds the following way: first monomers diffuse on the surface, then nucleation starts and islands grow until the islands coalesce, and finally all holes in the new monolayer are filled, and the new monolayer is completed.

Figure 3.2 shows a Monte-Carlo simulation of the development of the monomer density and the island density during the growth of a single monolayer [8]. Four regimes can be easily distinguished on the left side of figure 3.2.

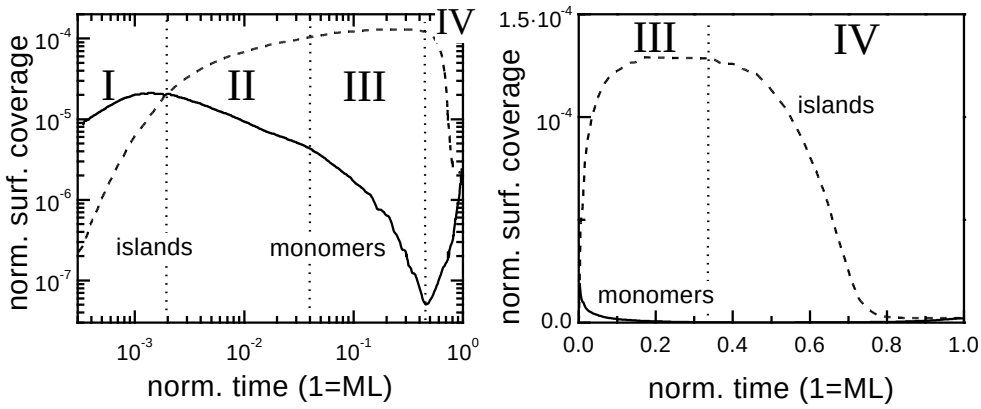

Figure 3.2: *Calculated coverage of monomers (atoms) and islands during the growth of one monolayer plotted on logarithmic (left) and linear scales (right) [8].*

I Island nucleation starts, the islands are small. The density of monomers is much higher than the density of islands.

II After the island and the monomer densities are equal, they become inversely proportional ($\propto t^{\frac{1}{3}}$ or $\propto t^{-\frac{1}{3}}$).

III When the size of the islands becomes comparable to the island spacing nearly all monomers can reach an island within the diffusion length. Thus, the monomer density is dropping rapidly.

IV Finally, the maximum number of islands is reached and the surface roughness is maximal. The density of islands is decreasing, since islands coalesce. On top of the islands nucleation is starting again, as soon as the size of an island becomes larger than the diffusion length. Hence the monomer density is increasing again.

The right hand side of figure 3.2 also shows monomer and island densities but on a linear time and surface coverage scale. Normally, these scales are relevant for comparison to actual growth experiments (like reflectance anisotropy oscillations discussed in section 6.6.1). Two things are remarkable: first the number of monomers at all times is very small, and therefore monomers are hardly observed experimentally. Secondly, only the development of the island size in regime III and IV (where no good analytical theory exists) is important for comparison of experiment and theory.

3.2.2 Step-Flow Growth

Real surfaces have steps at more or less regular distances, due to a slight misorientation. Obviously the effect of preferred incorporation at the step-edges becomes more pronounced if the steps get closer together. At a certain point, when the diffusion length λ becomes longer than the terrace width L, nearly all monomers are incorporated at the step-edges. This growth mode is called *step-flow growth*.

An analytical description for the transition from 2D island nucleation growth to step-flow growth was found in 1949 by *Burton, Cabrera* and *Frank* and is therefore called BCF-theory [9]. They calculated the dependence of α_{BCF} (number of monomers that reach a step) from terrace width L and diffusion length λ:

$$\alpha_{BCF} = \frac{2\lambda}{L} \tanh\left(\frac{L}{2\lambda}\right). \tag{3.11}$$

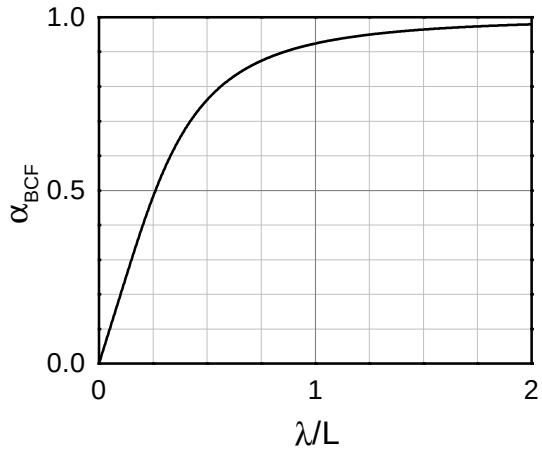

Figure 3.3: *Fraction of monomers that reach the step-edge during diffusion.*

In figure 3.3 α_{BCF} is plotted versus the normalized diffusion length $\frac{\lambda}{L}$. If the diffusion length λ is about the terrace width L, 92 % of the monomers can reach the step. Such a high fraction of monomers very likely corresponds to step-flow growth. If $\lambda = \frac{1}{4}L$ only 48 % of the incoming monomers are incorporated at the step-edges. The remaining monomers can form islands on the terrace and the growth is in the 2D island growth regime as described above.

The question remains at which diffusion length the transition to step-flow growth takes place. From figure 3.3, one can define the value of $\lambda = 0.5L$ with 76 % of monomers as the transition between these two modes.

3.3 Step-Bunching

The BCF-theory does not distinguish between monomers that arrive at the step from the upper or lower terrace. This is not necessarily correct. *Schwoebel* first pointed out that the change of the diffusion potential for a monomer due to a step-edge is important. A barrier might form at the step-edge, hindering either the monomers from the upper terrace to attach at the step and make it more easy for the monomers arriving from the lower terrace (defined as positive energy, as shown fig. 3.4) or vice versa.

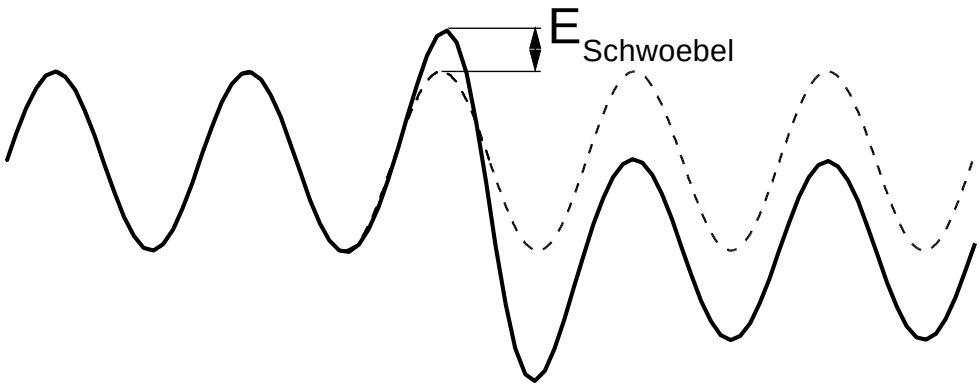

Figure 3.4: *The diffusion potential with a positive* Schwoebel*-barrier, which makes the attachment of monomers from the lower terrace more likely. (Dotted line: diffusion potential without a step.)*

As a result, during growth the steps are moving with different velocities over the surface. If the Schwoebel barrier is positive, steps that belong to a large terrace are moving slower than the ones close to a small terrace. The result is a very flat surface with equally spaced steps. However, the different case is also possible. In this case the steps on large terraces are moving faster "eating" small terraces. The resulting surface consists of areas with many steps and larger terraces. The effect of steps getting closer together and forming supersteps is called *step-bunching*.

To observe step-bunching on a vicinal surface two things are needed. First, the diffusion length has to be much longer than the terrace width; all of the incoming monomers can easily reach a step-edge, thus the growth proceeds in the step-flow regime. Secondly, there must be a negative Schwoebel barrier, i.e. a preferred attachment from the higher terrace.

In figure 3.5 the development of step-bunching is shown schematically.

(a) The initial vicinal surface has equally spaced steps.

(b) When the growth is initiated, small fluctuations of the terrace width appear, due to a random distribution of monomers on the surface. Since the flux of monomers to a terrace depends only on the size of the terraces, larger terraces are catching more monomers. A negative *Schwoebel*-barrier (i.e. a preferred attachment from the upper terrace) results in an faster enlargement of the wide terraces, because the step velocity is proportional to the number of impinging monomers and thus to the terrace width. Hence wide terraces are growing faster than any smaller neighboring terraces.

(c) Finally the terrace width of the largest terraces equals the diffusion length. Nucleation starts in the middle of these terraces. Hence the step propagation speed does not increase any more with increasing size of these terraces, since the number of monomers that reach the step remains constant.

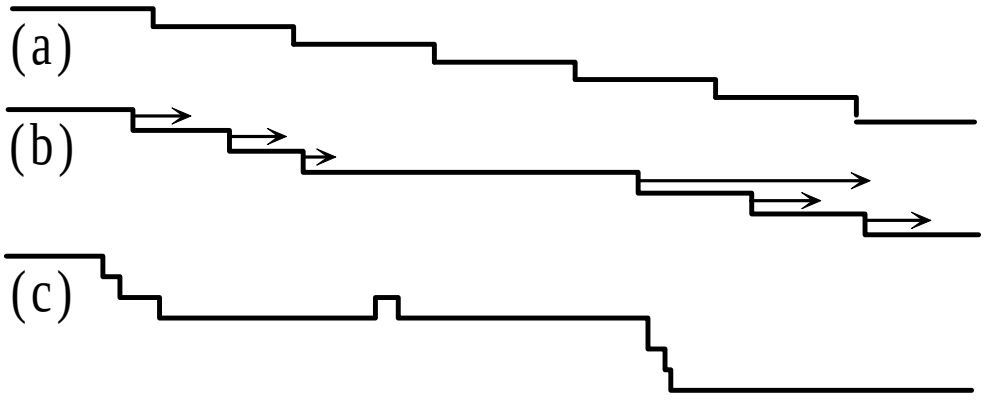

Figure 3.5: *The evolution of step-bunching: (a) initial surface, (b) growth starts (arrows: velocity of steps on the surface), (c) nucleation starts in the middle of the terraces.*

Due to this mechanism, the final terrace width saturates at the diffusion length of the monomers. However, the shape of the bunches is not determined by the Schwoebel barrier. There might be some step-repulsion, or it is more favorable to form a high index facet which would be either limited be the free energy (discussed in sec. 1.3) or different growth rates (see sec. 2). On GaAs (001) the mean distance of steps in the bunch region is between 7 and 18 atoms, probably limited in MOVPE by the presence of complete (nx6) unit meshes at the step-edges.

Even though the topography of the resulting surface is very similar to a surface formed by faceting, the underlying mechanism is completely different. Step-bunching is caused by anisotropic diffusion over the step-edges, while faceting is driven by differences of free energy of the surfaces (sec. 1.3) or by different growth rates on different surfaces (sec. 2).

4 Chemical Kinetics

In this study many processes like arsenic desorption are investigated to obtain activation energies and order of reactions. Therefore, the basic theory of chemical kinetics will be reviewed, using the simple reaction of A and B to the compound AB ($A + B \rightarrow AB$) as an example.

4.1 General Kinetics

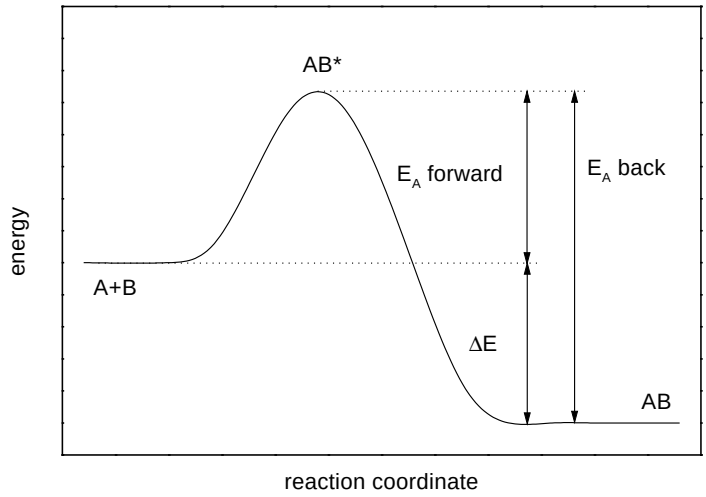

Figure 4.1: *The energy states during the reaction of A and B via AB^* to AB.*

Figure 4.1 shows the three energy states that are passed during the reaction of A and B to the compound AB. First A and B are separated and do not interact. To overcome the repulsive (Coulomb) forces a certain energy is needed: the activation energy E_A(forward). With this energy an "activated complex" AB^* is formed, and the attracting (bonding) forces are balanced by the repulsive (anti-bonding) forces. Now the atoms can either relax to their equilibrium positions in the new compound and release the excess energy of formation ΔE, or they separate again and release E_A(forward).

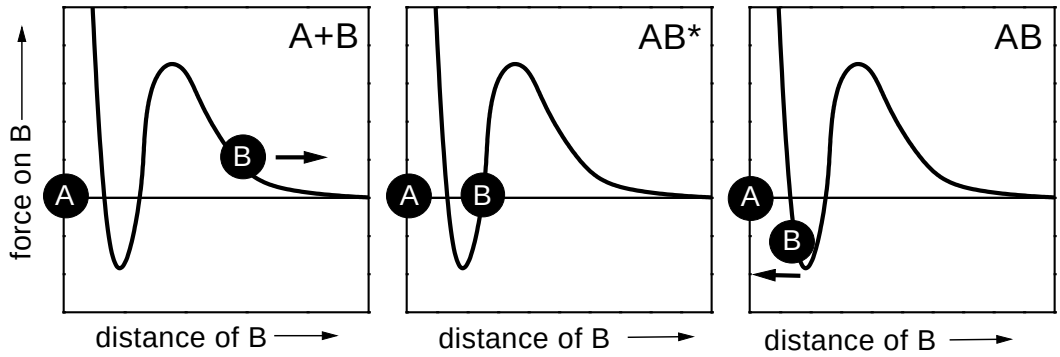

Figure 4.2: *Forces between atom A and B during the three stages of the formation of the compound AB: separate atoms (left) activated complex (middle) molecule (right).*

This three stages can also be seen in in the force on the atoms during formation (fig. 4.2. First the atoms are far apart, their positive charged cores are shielded by the valence elec-

trons. Only the negtive charged valence see each other, the the atoms are repulsing each others. If the atoms have enough kinetical energy, they can come close enough together that also attraction forces began to work. At a certain point a forces compensate: An activated complex is formed. If the atoms come even closer, the binding forces overtake and the molecule AB is formed.

The process shown in figure 4.1 is reversible. If the AB compound gets an energy higher than $E_A(\text{back}) = E_A(\text{forward}) + \Delta E$ it gets into the activated state AB^* and can finally dissociate into A and B. Therefore, an equilibrium of the concentration between the AB molecules and the A and B atoms is reached after some time. The equilibrium concentration depends mostly on the activation energy of the reverse reaction and on the speed of both, the forward and the back reaction. The speed of the reaction determines how fast the equilibrium is reached. It is defined as the first temporal derivative of the concentration. However, the speed of reaction is not necessarily constant and thus not a good measure for a reaction. To overcome this, a simple model for the concentration changes during chemical reactions was made:

$$-\frac{dc(t)}{dt} = kc(t)^n. \tag{4.1}$$

The reaction is now described by only two parameters: the *reaction order* n and the *reaction rate* k. The reaction order is often an integer, it depends on the underlying mechanism: e.g. the dissociation of a simple molecule $AB \rightarrow A + B$ is a first order reaction (the whole molecule must reach the activation energy). Another example is the reverse reaction $A + B \rightarrow AB$, which is of second order, because the activation energy is contributed by two partners. Finally, the reaction rate determines how fast the change towards equilibrium will be and is closely related to the activation energy.

Usually only time-dependent concentration $c(t)$ is measured during a reaction. To determine the reaction rate k and the order n of the reaction, an analytical model of $c(t)$ from the integrated equation (4.1) (see table 4.1) is fitted to the experimental obtained concentration transients $c(t)$. This is done for as many concentration transient measurements as possible. The reaction order n must remain constant for all transients, since it depends only on the mechanism of the reaction.

For the fitting, the reaction order n has to be determined first. (Usually a fitted n has a large error bar. For an analysis n is often rounded to the next integer or to a simple fraction like $\frac{n}{2}$. In this work all reaction orders have been assumed to be integers.)

reaction order	time dependent concentration $c(t)$
$n = 0$	$c(t) = c_0 - kt$
$n = 1$	$c(t) = c_0 \cdot \exp(-kt)$
$n = 2$	$c(t) = \frac{1}{kt - \frac{1}{c_0}}$
	$\vdots$
generally	$c(t) = \sqrt[1-n]{c_0^{1-n} + (n-1)kt} \quad (n \neq 1)$

Table 4.1: *time dependence of the concentration*

Next, we want to determine the activation energy from the obtained reaction rates k. The activation energy is supplied by the kinetic energy of particles, which again depends on the temperature. The number of particles with a certain energy (e.g. for a gas) is given by Maxwell's distribution:

$$F(v) = 4\pi C \exp\left(-\frac{mv^2}{2k_B T}\right) v^2. \tag{4.2}$$

The reaction rate k is assumed proportional to the number of atoms with an energy higher than the activation energy: $k \sim N(E > E_A)$. Thus one has to integrate equation (4.2) from $E_A = \sqrt{\frac{1}{2}mv_a^2}$ to ∞. The result is:

$$k \sim N(E > E_A) = \frac{8\pi C}{m}(E_A - 1)\exp\left(-\frac{E_A}{k_B T}\right) \sim \exp\left(-\frac{E_A}{k_B T}\right). \tag{4.3}$$

The number of particles with $E > E_A$ is proportional to $\exp(-\frac{E_A}{k_B T})$. Therefore, the reaction rate k (and also any other activated process) has the following form:

$$k(T) = k_0 \exp\left(-\frac{E_A}{k_B T}\right). \tag{4.4}$$

This equation gives a way to measure the activation energy. If one plots the reaction rates k, obtained at different temperatures, in an Arrhenius plot, i.e. plot $\log(k)$ versus the reciprocal temperature (in Kelvin), equation (4.4) is now transformed to $\log \frac{k(T)}{k_0} = -\frac{E_A}{k_B} T_{rez}$. The linear slope in the Arrhenius plot is equal to $\frac{E_A}{k_B}$. Thus, from the slope the activation energy can be calculated. Even more, any constant factor (any k_0 of $c_0(T)$ in tab. 4.1) does not influence the determination of the activation energy.

4.2 Measuring Kinetics on Surfaces

To measure the kinetics, a method is needed which can measure the change concentration of species at the surface. In the case of gallium arsenide, the species in questions are usually the content of arsenic and gallium of a certain reconstruction, i.e. the stochiometry of the surface.

4.2.1 Reflectance Anisotropy Spectroscopy

The method used in this work is the Reflectance Anisotropy Spectroscopy (RAS). For RAS linear polarized light is shone on a surface. Due to the reconstruction of the surface the polarisation of the reflected light is changed. This change is measured and normalized to the total intensity. The RAS signal is the normalized change of the polarisation along two prependicular axis, the direction depends on the surface orientation (see glossary on page 110).

An RAS spectrum can be used to identify a surface, by comparing it to spectra measured on well-ordered reference surfaces. Therefore, in the experimental part II reference spectra will be presented. If a well-ordered surface has a certain RAS spectrum, how does the spectrum of a combination looks like?

The answer is quite simple, since the RAS signal is directly proportional to the area of a reconstruction (like every unit mesh is a little dipole), a combination of two reconstructions on a surface is just proportional to a linear combination of these two spectras. This is illustrated in figure 4.3. The spectrum of the surface covered by 33 %$_{c(4x4)}$ and 66 %$_{ß2(2x4)}$ can be calculated by a linear combination of the RAS spectra of the two well-ordered reconstrutions.

Since each reference RAS spectrum corresponds to a well-ordered reconstruction, it corresponds also to a certain arsenic (or gallium) coverage of this reference surface. A change of reconstruction means always a change of the arsenic covereage. If, like in figure 4.3 indicated, the surface's reconstruction changes from arsenic rich c(4x4) to a more stochiometric ß2(2x4), the corresponding RAS spectra would change too. If only the time-dependent RAS signal at a certain energy is recorded (like indacted by the arrow in fig. 4.3 at 2.6 eV), the

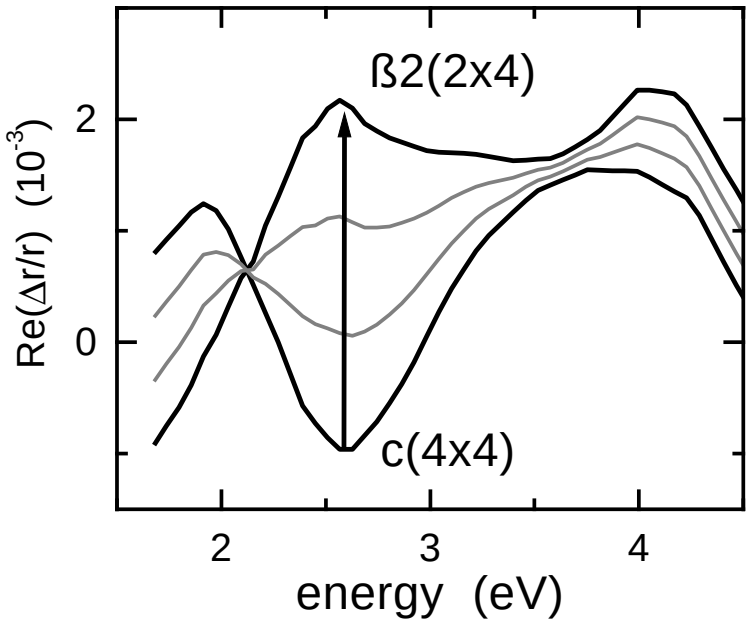

Figure 4.3: *RAS spectrum of a c(4x4) and a ß2(2x4) reconstruction on a GaAs (001) surface. Grey marked are the spectra of a 33 %$_{c(4x4)}$/66 %$_{ß2(2x4)}$ and 66 %$_{c(4x4)}$/33 %$_{ß2(2x4)}$.*

signal would gradually change from the starting to the end level. And since the RAS signal is proportional to the total area of c(4x4) and ß2(2x4) reconstruction, each point of such a linear combination can be assigned a certain coverage too.

4.2.2 RAS Signal and Kinetics

This is not neccessariely limited to gallium and arsenide on gallium arsenide surface. Therefore, in the following section the general connection of RAS to the chemical kinetic will be discussed, and how reaction rates and activation energies can be measured using RAS. The usual surface process analyzed by RAS is a change of reconstruction on the surface by adsorption/desorption experiments. In this case, the part of the concentration $c(t)$ of reactants is replaced by the coverage $\Theta(t)$ of the surface with the respective reactants.

An ideal surface, completely covered by a single well-defined reconstruction, is described by its characteristic adsorbate coverage $\Theta_{reconstruction}$ and its characteristic RAS signal $RAS_{reconstruction}$. If a surface is covered with more than one reconstruction, the fact that RAS is a linear optical method becomes important. All reconstructions contribute linearly to the RAS signal, with respect to their surface area: e.g. two reconstructions which cover 30% and 70% of the surface contribute 30% and 70% to the RAS signal [10]. More generally:

$$\begin{aligned} RAS &= \sum_i \sigma_i \cdot RAS_i \\ \text{with} \quad & \sum_i \sigma_i = 1, \end{aligned} \tag{4.5}$$

with σ_i is the normalized surface area of reconstruction i and RAS_i is the RAS-response of surface covered with reconstruction i by 100 % (i.e. $\sigma_i = 1$). But not only RAS_i the RAS signal is linear, Θ the coverage with a surface spezies (e.g. arsenic) is linear too:

$$\Theta = \sum_i \sigma_i \cdot \Theta_i. \tag{4.6}$$

Equations (4.5) and (4.6) are true for any functions for the surface area σ_i, therefore also for time dependent $\sigma_i(t)$'s. More important, since RAS_i and coverage Θ_i are caracteristic for each reconstruction i, the σ_i in equation (4.5) and (4.6) have to be exactly the same.

Now the general case of a change of the RAS signal due to a change of reconstructions can be analyzed. With the definition $\Delta RAS_i = RAS_i - RAS_1$ and $\Delta\Theta_i = \Theta_i - \Theta_1$ one obtains:

$$\begin{aligned} RAS(t) &= RAS_1 \cdot (1 - \sigma_2(t) - \sigma_3(t) - \ldots) + \sigma_2(t) \cdot RAS_2 + \sigma_3(t) \cdot RAS_3 + \ldots \\ &= RAS_1 - \sigma_2(t) \cdot RAS_1 - \sigma_3(t) \cdot RAS_1 - \ldots - \sigma_n(t) \cdot RAS_1 \\ &\qquad + \sigma_2(t) \cdot RAS_2 + \sigma_3(t) \cdot RAS_3 + \ldots + \sigma_n(t) \cdot RAS_n \\ &= RAS_1 + \sigma_2(t) \cdot \Delta RAS_2 + \sigma_3(t) \cdot \Delta RAS_3 + \ldots + \sigma_n(t) \cdot \Delta RAS_n \quad (4.7) \\ \Theta(t) &= \Theta_1 + \sigma_2(t) \cdot \Delta\Theta_2 + \sigma_3(t) \cdot \Delta\Theta_3 + \ldots + \sigma_n(t) \cdot \Delta\Theta_n. \quad (4.8) \end{aligned}$$

Thus, in principle n different processes can be simultaneously analyzed. However, only the case of one process is of practical importance, because during a desorption/adsorption process a surface usually changes from reconstruction 1 to reconstruction 2:

$$\begin{aligned} RAS(t) &= \sigma_1(t) \cdot RAS_1 + \sigma_2(t) \cdot RAS_2 \\ RAS(t) &= RAS_1 + \sigma_2(t) \cdot \Delta RAS_2 \quad (4.9) \\ \text{and} \quad \Theta(t) &= \Theta_1 + \sigma_2(t) \cdot \Delta\Theta_2 \quad (4.10) \end{aligned}$$

For the analysis of surface reactions the time dependent volume concentration $c(t)$ is replaced by the time dependent surface coverage $\Theta(t)$. Since $c(t)$ fulfills the differential equation (4.1), $\Theta(t)$ fulfills this equation too. Because RAS_i as well as Θ_i are constants, it follows from equation (4.9) and (4.10) that the RAS signal is proportional to the surface coverage with a certain surface species:

$$RAS(t) \propto \Theta(t). \quad (4.11)$$

Therefore, instead of $\Theta(t)$ the time dependent RAS signal $RAS(t)$ can be used as a measure of surface concentration, and can be analyzed according to the differential equation (4.1). Hence, to obtain the reaction rate from the change of a measured RAS, $RAS(t)$ is fitted by one of the functions from table 4.1. The function which fits best gives the reaction order and the reaction rate k. To obtain the activation energy of a process, reaction rates must be obtained at several temperatures. The linear slope of the logarithm of the reaction rates plotted versus the reciprocal temperature $1/T$ (Arrhenius plot) corresponds to the activation energy of that process, as discussed previously.

It has to be noted that only for first order reactions k from the fit to the RAS transients gives a true reaction rate. For any other reaction rate a fit yields $\tilde{k} = k \cdot (\Delta RAS)^{1-n}$. However, this is not a problem for the determination of the activation energy as long as the temperature dependence of $\Delta RAS(T)$ is negligible. (In the Arrhenius plot $\tilde{k}$ has an constant offset to the "true" k of $\log(\Delta RAS)$, thus the slope and therefore the activation energy remains unchanged). For most experiments $\Delta RAS(T) \approx const$ is a good approximation, since over a temperature range of 100 K the reaction rates k are usually changing by about 1.5 to 2 magnitudes, while the change of RAS amplitude is below 10 %.

5 MOVPE Process

This work investigates the growth of gallium arsenide on different GaAs single crystal surfaces. The samples were grown using Metal-Organic Vapor Phase Epitaxy (MOVPE), a process introduced at the end of the sixties by Manasewit [11]. Its predecessor was the Chloride Vapor Phase Epitaxy (Cl-VPE or simply VPE). Several crossover processes existed, to overcome one or another disadvantage. Nowadays MOVPE has finally won the competition to grow large scale homogeneous structures with atomic precision at low costs.

MOVPE of III/V semiconductors often uses hydrides like AsH_3 (the UPAC-name is arsan, but more common is the old name arsine) as a precursor for the group V elements. Nowadays liquid and less toxic, alternative precursors like tertiary Butyl-Dihydrides are used.

As precursor for group III elements liquid metal-organic tri-methyl compounds like TMGa (tri-methyl-gallium), TMIn, and TMAl are standard. The use of TEGa (triethyl-gallium) is less common. Only for some special applications like selective area growth or low temperature growth, other compounds such as TIBGa (tri-isobutyl-gallium), TEIn (tri-ethyl-indium), DMEAAl (di-methyl-ethyl-amin-alane) and others are used.

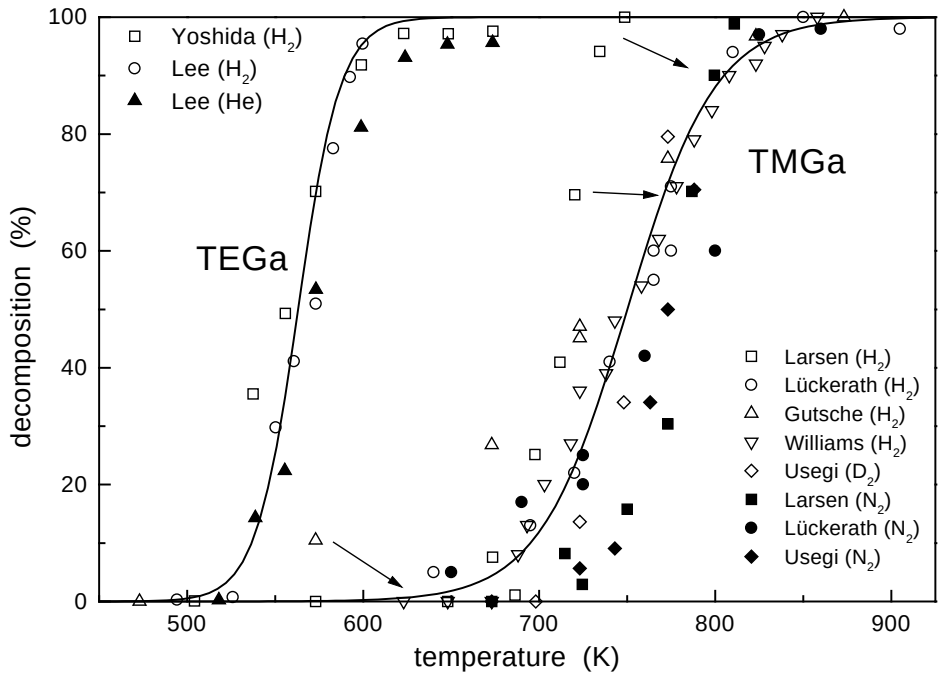

Figure 5.1: *Decomposition of TEGa (Yoshida [12], Lee [13], Williams [14]) and TMGa (Usegi [12], Larsen [15], Williams [14] Lückerath: [16], Gutsche: [17]) in the absence of AsH_3. The values of Lückerath and Gutsche have been shifted by 50 K to lower temperatures (see text).*

The precursors are mixed to a carrier gas, usually hydrogen or nitrogen. It provides a high flux through the reactor and therefore a fast change of the vapor phase gas composition. The total pressure is usually around 2-10 kPa[1]. The precursors are thermally decomposed above a heated susceptor. The susceptor is made of graphite, or seldom, of molybdenum. In the center of the susceptor the substrate (the sample) is located.

[1] 1 kPa=10 mbar

The carrier gas is supposed to be inert (but in sections 6.2 and 6.3.3 evidence for chemical activity of the carrier gas will be discussed in detail). Mass-spectroscopy measurement of the decomposition of TMGa together with AsH_3 in a deuterium carrier gas showed that the hydrogen for the formation of CH_4 indeed comes from the AsH_3 and the carrier gas is inert in this case. Therefore, the sum reactions are the following:

$$\begin{aligned} \text{TMGa:} \quad & AsH_3 + (CH_3)_3Ga \rightarrow GaAs + 3CH_4{}^{\uparrow} \\ \text{TEGa:} \quad & AsH_3 + (C_2H_5)_3Ga \rightarrow GaAs + 3C_2H_4{}^{\uparrow} + 3H_2{}^{\uparrow}. \end{aligned} \tag{5.1}$$

However, the sum reactions do not tell which intermediate products might be of importance for the surfaces. There has been a number of investigations of the decomposition of TMGa [14, 15, 16, 18, 19], TEGa [12, 13, 14, 19], and AsH_3 [14, 15, 16, 17, 20]. Figure 5.1 shows the typical decomposition temperatures for TEGa and TMGa in different atmospheres taken from these studies. Note the big scattering for the TMGa data, which is probably due to the different methods, but also due to some systematical errors (e.g. in [16, 17] the gas was sampled a little bit above the susceptor, thus the "true" gas phase temperatures are probably about 50 K lower).

The general trend in figure 5.1 shows a 200 K lower temperature for 50 % decomposition for TEGa as compared to TMGa, which is due to the different decomposition pathways of the gallium precursors. TMGa decomposes by radical formation in the vapor phase:

$$\begin{aligned} Ga((CH)_3)_3 + R\cdot &\rightarrow \cdot Ga((CH_3)_2 + R\text{-}CH_3 \\ \cdot Ga((CH_3)_2 + R\cdot &\rightarrow :GaCH_3 + R\text{-}CH_3 \end{aligned} \tag{5.2}$$

The loss of the first methyl group needs an activation energy of 4.9 eV, the second 3.1 eV [20, Tab 4.1]. No further decomposition takes place in the vapor phase. Therefore, at least (CH_3)Ga: (mono-methyl-gallium) is present on the surface [16, 7.2]. The 50 % decomposition temperature is about 750 K in a hydrogen atmosphere, and 20-30 K higher with nitrogen carrier gas (fig. 5.1). However, 100 % decomposition is reached for both at about 800 K.

TEGa on the other hand decomposes by $\beta-$elimination:

$$(CH_3 - CH_2) - Ga\text{-}R \rightarrow CH_2 = CH_2 + H\text{-}Ga\text{-}R \tag{5.3}$$

The activation energy for TEGa decomposition is low, 2.1 eV in the gas phase and 0.6 eV on the surface [20, 6.1.1]. Even more, highly reactive GaH_x is delivered to the surface, so growth is possible at temperatures below 750 K. Since no radicals or other external reaction partners are needed, the $\beta-$elimination of TEGa is independent from the carrier gas, as also found by the experiments. 50 % decomposition is at T=(562 ± 12) K.

The decomposition of AsH_3 is again by radical formation, like TMGa: [16, 7.2],[20, 6.1.1 and 4.2.2.2].

$$\begin{aligned} AsH_3 + R\cdot &\rightarrow \cdot AsH_2 + H\text{-}R \\ \cdot AsH_2 + R\cdot &\rightarrow :AsH_1 + H\text{-}R \\ :AsH_1 + R\cdot &\rightarrow :As\cdot + H\text{-}R \end{aligned} \tag{5.4}$$

The activation energy for removing a hydrogen atom is 2.6 eV [20, Tab. 2.2, 6.1.1 and 4.2.2.2]. The decomposition of AsH_3 is enhanced in the presence of GaAs [15, 20]. Therefore, at least some partly decomposed AsH_x reaches the surface and reacts there. Furthermore, growth using solid source evaporation of As_2 or with "hydrogen-free" precursor like tri-methyl-arsine (TMAs) usually results in layers with a poor morphology, thus AsH_x is important for the growth process: The hydrogen of AsH_x is essential to desorb the left-over

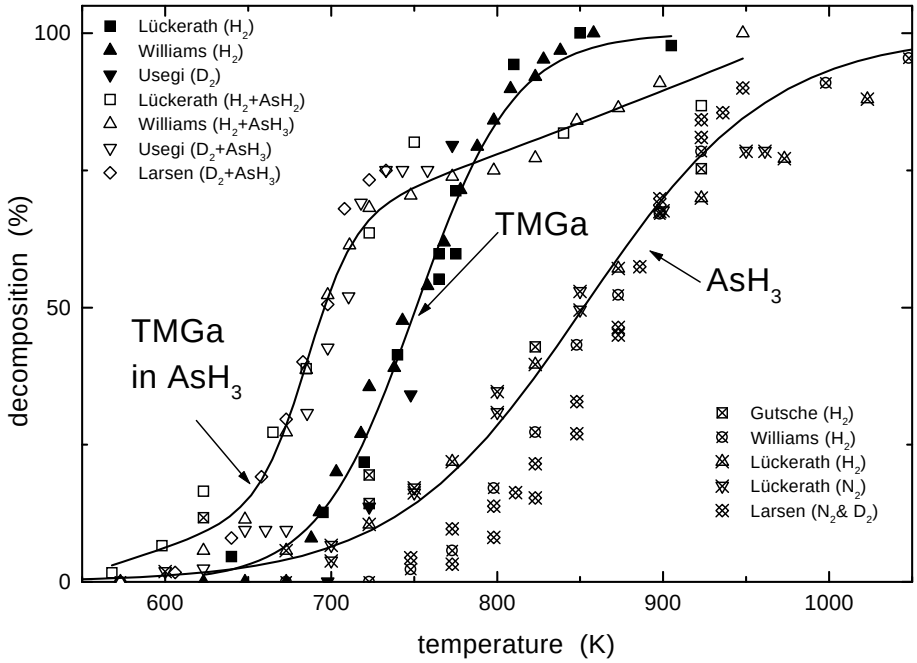

Figure 5.2: *Decomposition of AsH_3 (Williams [14], Lückerath [16], Gutsche [17], Larsen [20, fig. 4.15]) and TMGa (Usegi [12], Larsen [15], Williams [14], Lückerath [16]) in the absence or presence of AsH_3. The values of Lückerath and Gutsche have been shifted by 50 K to lower temperatures.*

methyl groups from the TMGa [19, 15]. However, in section 6.7 the influence of the coverage of the surface with methyl or methylene on carbon incorporation will be thoroughly discussed.

During growth of GaAs both AsH_3 and TMGa are present. In this case, as it can be seen in figure 5.2, the TMGa decomposition is strongly enhanced at the onset of the AsH_3 decomposition. This is most likely due to hydrogen radicals produced by AsH_3 decomposition.

The decomposition behavior as shown in figure 5.2 is what finally limits the growth rate, plotted in figure 5.3. Three different regimes can be observed in figure 5.3:

Desorption limited growth: At very high temperatures (above 1100 K) the growth rate decreases with increasing temperature. The limiting factor is the desorption of gallium species before incorporation.

Transport limited growth: (also called diffusion limited growth) In the mid-temperature range the growth rate is nearly independent of the temperature. The growth rate is only limited by the amount of gallium precursor offered to the surface.

Kinetic limited growth: At lower temperatures (below 750-800 K for TMGa and 700-650 K for TEGa) the growth rate decreases with decreasing temperature.

The change of the growth rates in the three regimes is shown in figure 5.3 (left side). Since the data are from different publications (and thus different MOVPE set-ups) they are normalized.

The drop of the growth rate in the kinetic limited growth regime at lower temperatures using TMGa is due to incomplete decomposition of TMGa (i.e. many methyl groups are reaching the surface). Furthermore, the amount of atomic hydrogen from the decomposition of AsH_3 is very small (fig. 5.2), but the hydrogen is needed to desorb the methyl groups

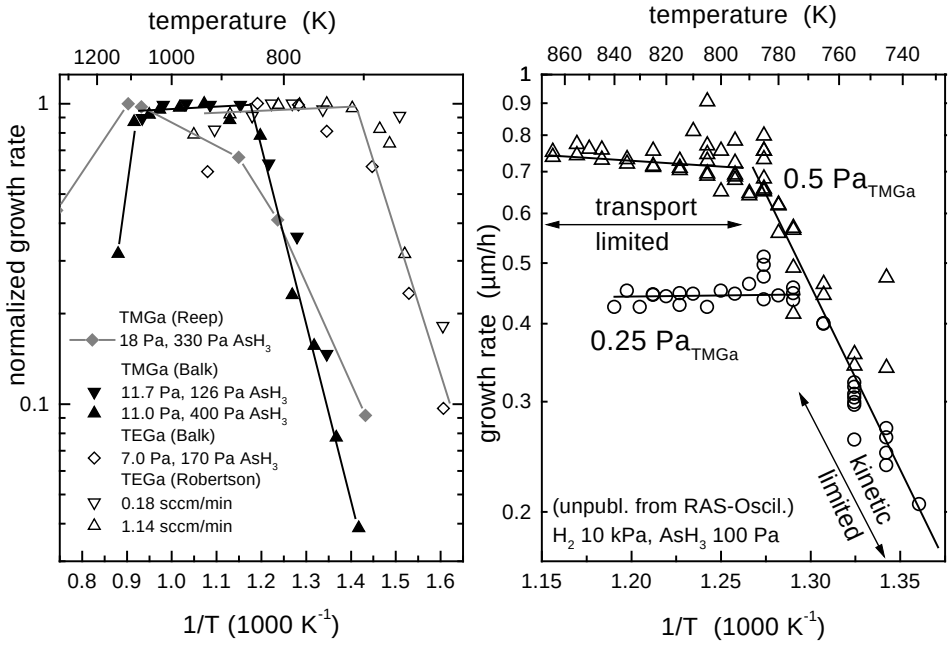

Figure 5.3: *Normalized growth rates on (001) GaAs using AsH_3 and either TMGa (Reep [21] (100 kPa), Balk [22]) or TEGa (Balk [22], Robertson [23]). Our data with much lower TMGa partial pressures are plotted for comparison in the right diagram.*

from the TMGa, which are bound quite strongly. Thus adsorbates cover a good part of the surface and hinder further precursor attachment.

The presence of adsorbates on the surface at low temperatures is known from the self-limiting Atomic Layer Epitaxy (ALE) growth mode using TMGa. ALE is done by alternatively switching between AsH_3 and TMGa. In a wide regime of parameters ALE leads to a growth rate of exactly one monolayer per exposure cycle on the GaAs (001) surface. This is only possible if during the TMGa exposure an adsorbate layer is formed, which prevents further TMGa attachment. A detailed study of the surfaces formed by exposure of a (001) surface to TMGa can be found in section 6.4.2.

Using TEGa, the kinetic limited growth regime might indeed be due to incomplete decomposition of the precursor, since no self limiting ALE growth mode and thus no adsorbate layers, that would hinder precursor adsorption, has been reported.

The transition temperature between transport limited growth (constant growth rate) and kinetic limited growth (decreasing growth rate) depends on the partial pressure, as it can clearly be seen on the right hand side of figure 5.3 for TMGa partial pressures of 0.5 Pa and 0.25 Pa. The TMGa partial pressure dependence of the saturation of the growth rate at constant temperatures is shown in figure 5.4 for atmospheric pressure MOVPE (i.e. p_{total}=100 kPa). The saturation of the growth rate in the kinetic limited regime depends only on the TMGa partial pressure and not on the surface orientation [21].

Using TEGa such a saturation of the growth rate has not been reported. From the growth rate dependence with temperature, a kinetic limited growth regime exists below 650 or 700 K. However, at these low temperatures the AsH_3 decomposition is negligible, and layers grown at these temperatures show many defects.

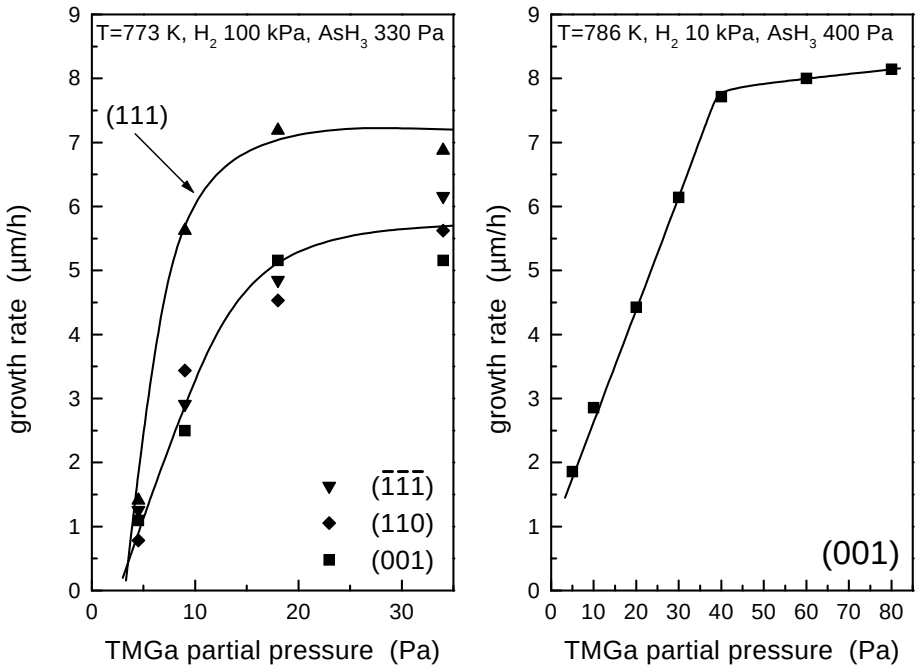

Figure 5.4: *Growth rate dependence on TMGa partial pressure for several GaAs surfaces at 773 K [21] and on the (001) GaAs surface at 786 K [24].*

II

The Gallium Arsenide (hkl) Surfaces

In this part all surfaces will be investigated, starting from the (001) surface. Following the circle of figure 1.3 next will be (115), (113), (110), (1$\bar{1}$3), and finally (1$\bar{1}$5).

First the reconstructions of these surfaces will be introduced. Next the arsenic desorption on these surfaces is discussed and finally the actual growth processes will be reviewed.

6 (001) Surface

A phase diagram for MBE growth (fig. 6.1) shows many different reconstructions on the (001) surface. Some of them are also found in MOVPE. In the following sections I will briefly review them from arsenic rich to gallium rich conditions, i.e. from the right side to the left in the phase diagram in figure 6.1.

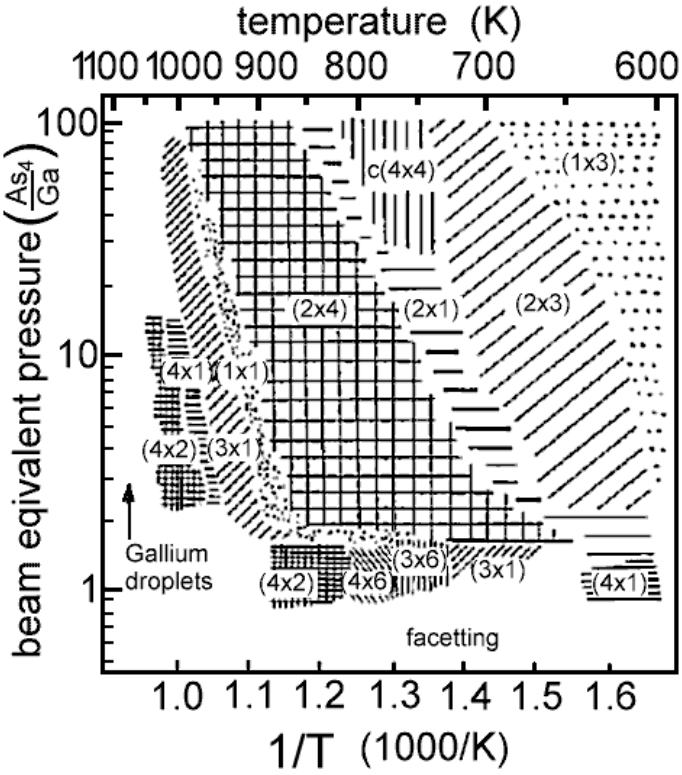

Figure 6.1: *Reconstruction observed during MBE growth on a vicinal GaAs (001) surface, misoriented 2˚ in [110] direction [25].*

6.1 Well-ordered Surfaces

6.1.1 (4x3) Reconstruction

A reconstruction with (4x3) symmetry has not been reported before. Probably the (2x3) reconstruction found at low temperatures in MBE (fig. 6.1) has a similar structure. However, in a MOVPE reactor a (4x3) reconstruction seems to be always present at temperatures below 800 K with AsH_3 flowing. A typical RAS (Reflectance Anisotropy Spectroscopy) spectrum of the (4x3) reconstruction at room temperature is shown in figure 6.2. To further investigate this reconstruction by UHV-based surface science methods, a special MOVPE system attached to an UHV analysis chambers was used (see appendix C).

Figure 6.3 shows a LEED image of a (4x3) reconstruction prepared by MOVPE and then transferred into UHV. The LEED pattern corresponds to a (4x3) symmetry: Along the main axes (2x1) spots are present, and additional streaks appear at $(\frac{1}{4}, \frac{1}{3})$, $(\frac{3}{4}, \frac{1}{3})$, $(\frac{1}{4}, \frac{2}{3})$, and $(\frac{3}{4}, \frac{2}{3})$.

The *in-situ* RAS spectra recorded between 800 K and room temperature show only changes due to the temperature but the shape of the spectra remains essentially the same. Therefore, the reconstructions at 800 K and at room temperature are identical and corre-

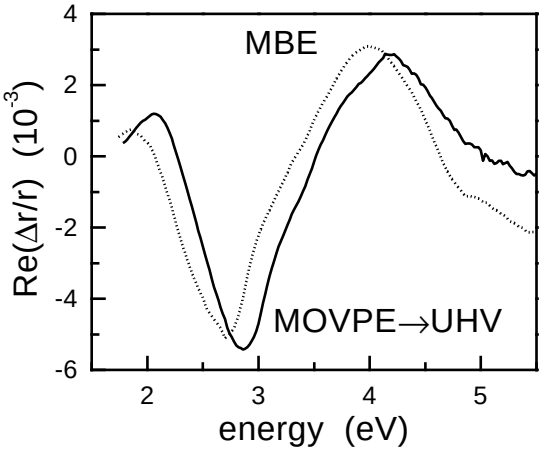

Figure 6.2: *RAS spectra of the (4x3) reconstruction after transfer of a MOVPE sample to an UHV analysis system at room temperature (see fig. 6.3) and the RAS spectrum of an arsenic rich sample in a MBE chamber at ≈600 K (no symmetries were measured).*

sponds to the most arsenic rich reconstruction observed on the (001) surface so far. (The influence of the temperature on the RAS spectra of arsenic rich surfaces will be discussed in more detail in section 6.2.)

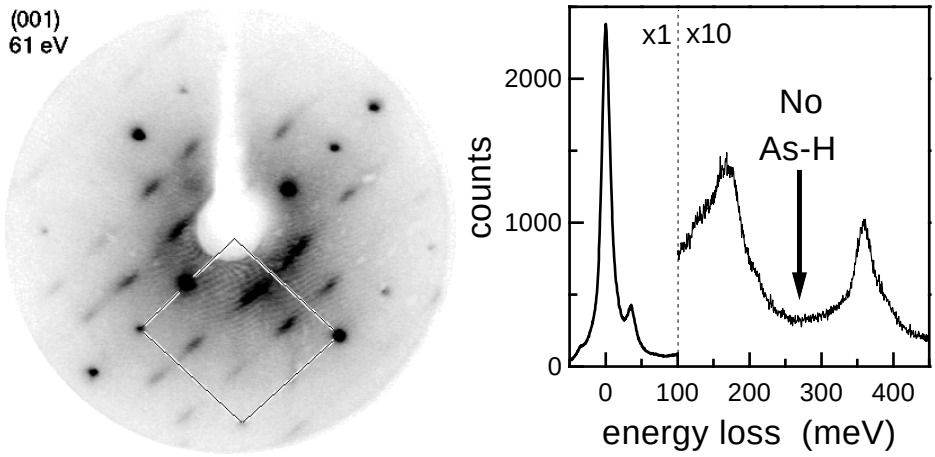

Figure 6.3: *LEED image and HREELS spectrum of the (4x3) reconstruction. (The large peaks are Fuchs-Kliever phonons, bulk related vibration.) Note the absence of As-H vibrations in the HREELS spectrum, which are expected around 262 meV (arrow).*

Also interesting is the absence of As-H vibration in the HREELS spectrum in figure 6.3. At 170 meV there is a small shoulder, related to C-H-vibrations, but all other peaks are bulk induced vibrations. Hence all AsH_3 is completely decomposed and this reconstruction is certainly not hydrogen induced. This was expected since the AsH_3 was switched off at 475 K, 25 K above the observed desorption temperature of 450 K of hydrogen on a GaAs (001) surface in UHV [26, 27].

A threefold symmetry along [110] like (4x3) is not very common. However, reconstructions with threefold symmetry appear during the low temperature growth of GaAs (001) in MBE, as it can clearly be seen in the phase diagram in figure 6.1. At very arsenic rich conditions (e.g. high arsenic fluxes and low gallium fluxes and temperatures) (1x3) and (2x3) symmetries are dominating. Further experimental evidence of a well-ordered very arsenic-

rich reconstruction comes from arsenic desorption experiments, where at very arsenic rich preparation conditions a desorption peak in TDS (Thermal Desorption Spectroscopy) prior to the c(4x4) (the most arsenic rich reconstruction reported so far) appears [28, 29]. However, complete evidence will be presented in section 6.3.1.

Zhang et al. calculated the surface energy for a number of reconstructions on the GaAs (001) surface using either DFT-LDA (Local Density Approximation – Density Functional Theory) (in fig. 1.4) or their own LCSM (Linear Combination of Structural Motive) method [2]. The result of LCSM calculations of arsenic rich structures is shown on the right hand side of figure 6.4. Together with the c(4x4) a c(8x6) reconstruction has the lowest surface energy at arsenic rich conditions (low $\Delta\mu_{Ga}$) (left hand side of the total energy diagram in figure 6.4).

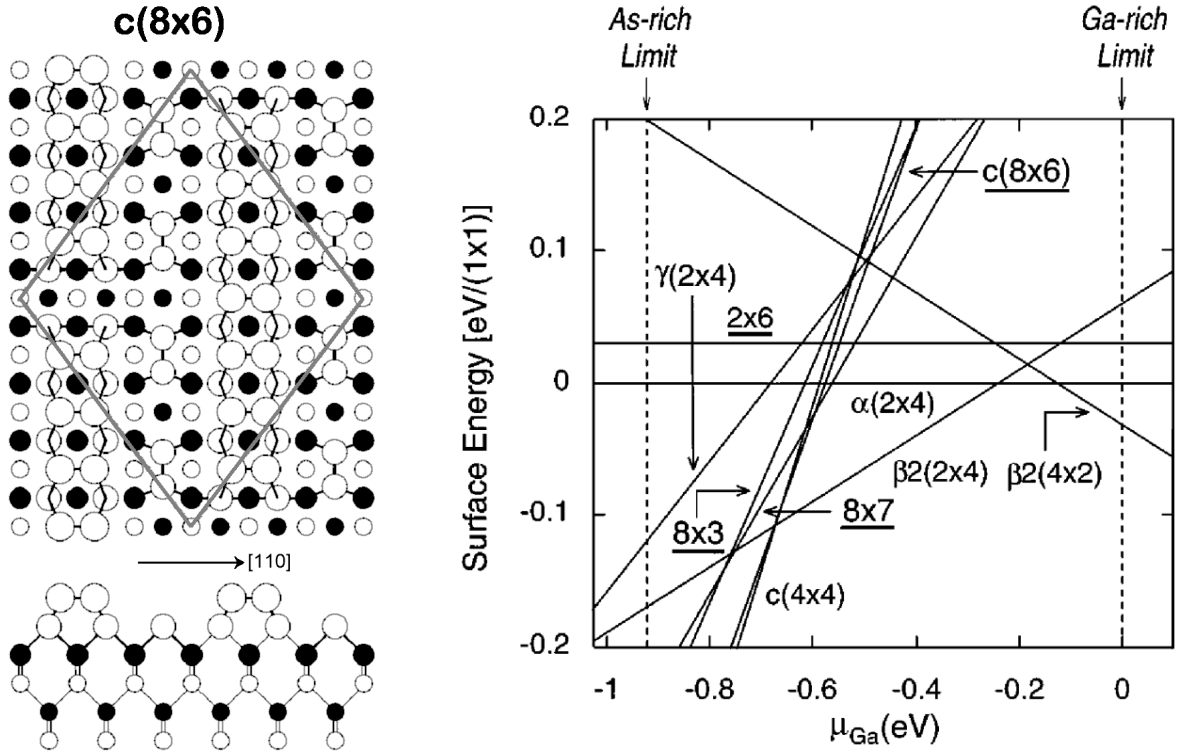

Figure 6.4: *Structure of c(8x6) which is probably related to the (4x3) (left side), and the calculated total energy of several arsenic rich reconstructions (right side) [2]. The c(8x6) has nearly the same surface total energy as the c(4x4) reconstruction.*

The calculated c(8x6) reconstruction has an arsenic coverage of 1.67 ML_{As} (ML=monolayer), less than an ideal c(4x4) with three arsenic dimers (1.75 ML_{As}). However, arsenic desorption experiments, which will be discussed in section 6.3.1, suggest that the (4x3) reconstruction is more arsenic rich than the c(4x4). If an arsenic dimer is added to the c(8x6), the resulting (2x3) structure would also have an arsenic coverage of 1.75 ML. STM measurements of a (2x3) reconstruction suggested, that such a dimer arrangement indeed exists [30].

A more arsenic rich reconstruction than the c(4x4) with trifold symmetry may contain a third top-layer of arsenic. In fact, DFT-LDA calculations of arsenic dimer adsorption showed that the site on top of a c(4x4) arsenic dimer is favorable for the adsorption of another arsenic dimer [31].

To conclude, the structure of the very arsenic rich (4x3) reconstruction is still unknown, but it is not hydrogen induced and it is more arsenic rich than the c(4x4) reconstruction.

6.1.2 c(4x4) Reconstruction

The most investigated arsenic rich structure is the c(4x4) reconstruction. It can be prepared either by annealing a surface in an arsenic rich environment or by desorbing an amorphous arsenic cap layer.

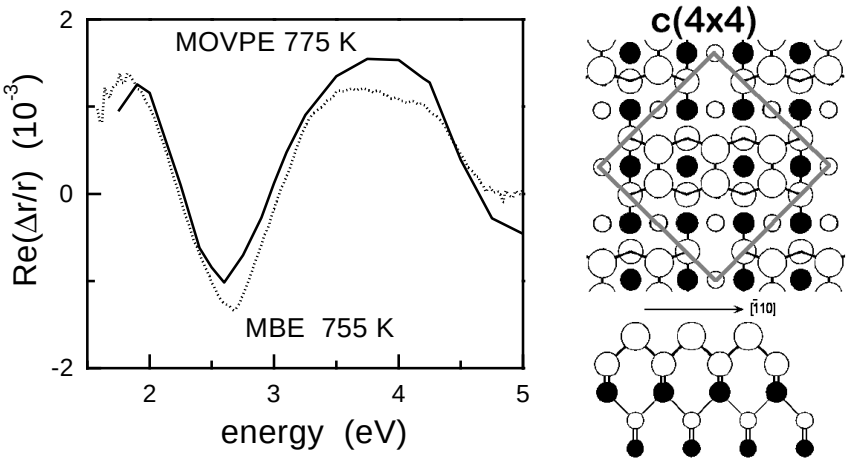

Figure 6.5: *RAS spectra of and structure of the c(4x4) reconstruction.*

The structure of the c(4x4) has been investigated both in MOVPE [32, 33, 34] and MBE [29, 28, 35, 36, 37]. The established model consists of three arsenic dimers on an arsenic monolayer (fig. 6.5); a mixture of two and three arsenic dimers at typical growth temperatures (700-900 K) is also in discussion.

GIXD measurements in an MOVPE reactor at 733 K and 30 Pa $tBAsH_2$ indicate towards the existence of an "arsenic deficient" c(4x4) reconstruction with a mixture of three and two arsenic dimers. The best fit to the recorded GIXD peak intensities was a combination of 30 % two and 70 % three dimer model, although the three dimer model alone showed reasonable agreement too [32]. Another GIXD work also suggested a mixture of two and three dimers on MBE prepared samples, although no percentage was given [36].

The model of the three dimer reconstruction is mainly based on STM-images of quenched MBE-grown layers [35], and also on decapped samples only a few unit meshes with apparently two dimers were found [38]. The STM-images always showed the same very regular, typical brickwork pattern of a three dimer c(4x4) reconstruction.

To sum up, two structures with c(4x4) symmetry exist. One contains two arsenic dimers and the other three, and both fulfill the electron counting rule. However, at room temperature only the three dimer variant has been observed. Therefore, the two dimer variant may only appear for short times during desorption processes or at elevated temperatures.

6.1.3 (2x4) Reconstructions

Reconstructions with (2x4) symmetry are the most investigated reconstructions in the entire GaAs system, because during MBE growth the surfaces shows (2x4) symmetry over a wide range of parameters (see fig. 6.1). Thus the surfaces can be easily prepared and investigated using many surface science techniques. In MBE, RHEED (Reflection High Energy Electron Diffraction) is normally used to determine the symmetry of reconstructions. Therefore three different (2x4) phases (named α, β and γ) were proposed, according to the brightness of the $(\frac{2}{4})$ streak along the fourfold symmetry axes.

However, only two different reconstructions with (2x4) symmetry have been proven stable by DFT-LDA calculations [2, 39, 40] (see fig. 6.4 and 1.4), STM experiments [40, 41],

and some other methods. These two stable reconstructions are named $\beta 2$(2x4) and the α(2x4) (see fig. 6.6 for model). The γ(2x4) was experimentally shown to consist of a mixture of $\beta 2$(2x4) and c(4x4) [41].

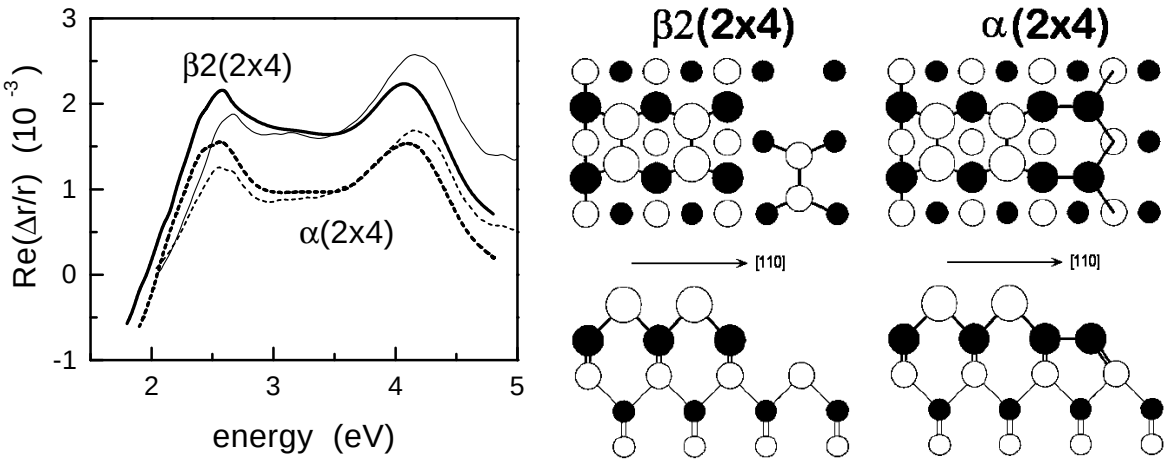

Figure 6.6: *RAS spectrum and atomic structure of α(2x4) (dotted) and $\beta 2$(2x4) (solid lines) reconstruction in MOVPE (thick lines, 925 K) and MBE (thin lines, 845 K and 895 K)*

Both (2x4) reconstructions are quite similar. The only difference between the α and $\beta 2$ structure is the additional arsenic dimer of the $\beta 2$(2x4). No surface intermixing, i.e. an arsenic in the gallium layer or vice versa occurs. Both structures have a trench between the dimer rows, which is very important to gallium diffusion in MBE growth, since it causes anisotropic diffusion lengths in MBE.

As it can be seen in figure 6.6 the RAS spectra of the $\beta 2$(2x4) and the α(2x4) are very similar. The RAS spectrum of the α(2x4) is only shifted about 0.6 to lower values with respect to $\beta 2$(2x4).

6.1.4 (nx6) Reconstructions

The (nx6) family has many members: (1x6) [42], (2x6) [35, 43], (3x6) [25, 44], (4x6) [25, 33, 42, 44], and (6x6) [45] were reported. The structural motif inherent in all these reconstructions is the presence of both gallium and arsenic dimers within a single reconstruction.

These reconstructions are typically observed during growth in MOVPE, or after prolonged annealing in UHV. From the RAS spectrum, the (nx6) reconstruction seems also present during growth. However, surfaces during growth is the topic of section 6.6.1.

6.1.5 (4x2) Reconstruction

The (4x2) represents the most gallium rich reconstruction known. Even though STM measurement have been reported for about ten years [35], the structure of the (4x2) reconstruction is still controversially discussed. UHV investigations are difficult, because it is nearly impossible to prepare a (4x2) reconstruction without traces of a six-fold symmetry. Even the gallium coverage of the (4x2) reconstruction is not fixed: it seems that additional gallium can be adsorbed in gallium clusters on the (4x2) reconstruction between the dimer rows [46].

In-situ, the (4x2) reconstruction can be easily prepared by deposit some gallium on a (2x4) reconstructed surface at temperatures above 875 K, as described in section 6.4.2.

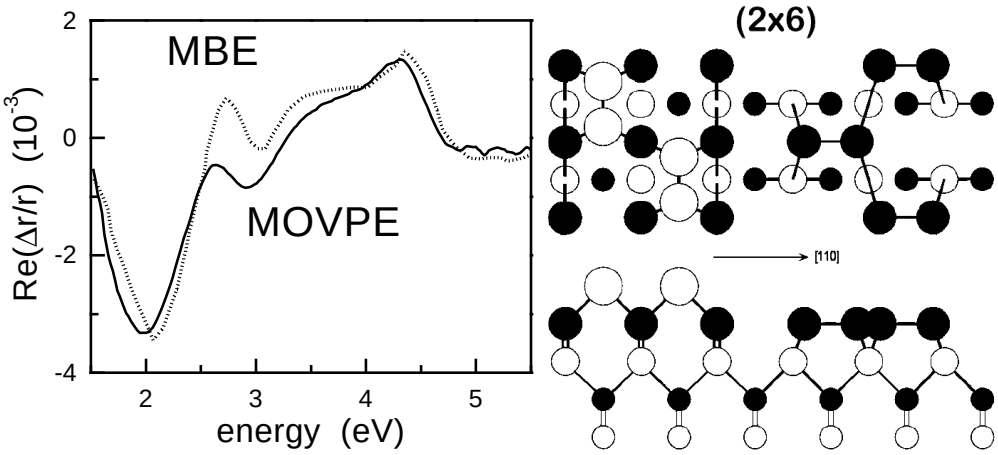

Figure 6.7: *RAS spectra in MOVPE [33] of (4x6) and MBE [42] of (1x6) and structure of the (2x6) reconstruction [35].*

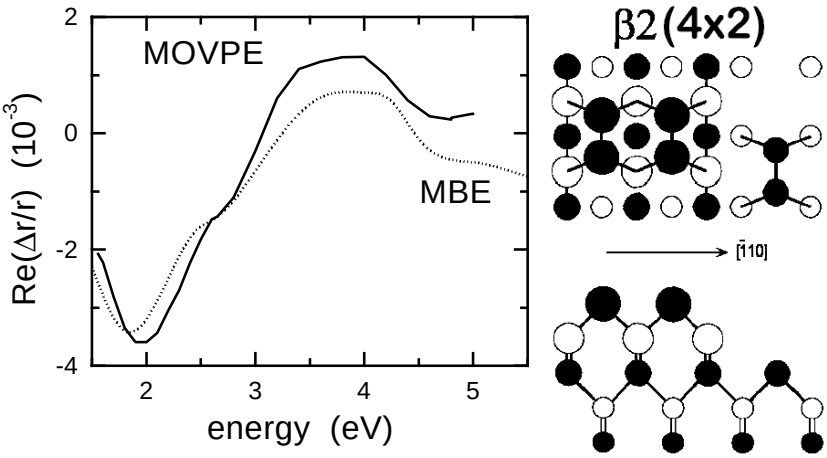

Figure 6.8: *RAS spectra and structure of $\beta 2(4x2)$ in MOVPE (T=923 K) and MBE (T=823 K) [42].*

6.1.6 (1x2)-CH_3 Reconstruction

This is an adsorbate covered surface. There are two models for this surface in literature. A well-ordered (1x2)-CH_3 is obtained by exposing a c(4x4) reconstruction to CH_3 radicals and then annealing the surface. This (1x2)-CH_3 reconstruction is composed of mixed Ga-As-dimers on top of an arsenic layer [47]. Adsorbed to the Ga-atoms of the dimer is a methyl group (fig. 6.9 middle). This (1x2)-CH_3 model is strongly supported by GIXD transient measurements during growth, where a $\times 2$ symmetry remains [48].

There is another model of an adsorbate covered (1x2) reconstruction. This model assumes the (1x2) to be a disordered c(4x4) with CH_3 adsorbed to first layer undimerized arsenic atoms. However, this model can neither explain the sharp (1x2) LEED pattern, nor the slightly lower arsenic coverage compared to a c(4x4) measured by Auger Electron Spectroscopy (AES) [47].

The main difference between the model is the bonding partner of the methyl groups. In on the well-ordered (1x2)-CH_3 it is gallium, while on the disordered surface the methyl groups are bound to the arsenic. Although IR adsorbtion spectroscopy has been done in this surface, the adsorbtion sites of the methyl groups has been not definitively identified [34, 49].

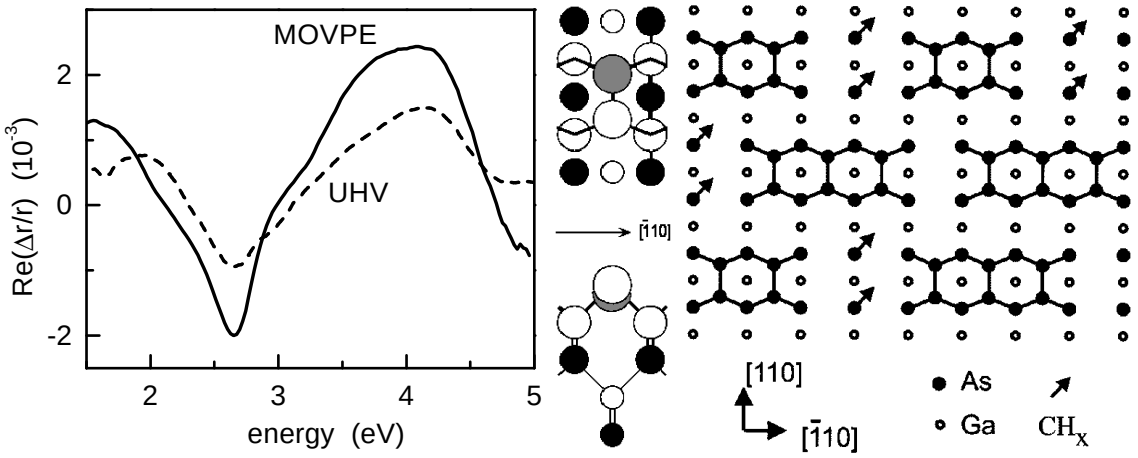

Figure 6.9: *RAS spectra and structure of arsenic rich (1x2)-CH_3 in MOVPE (during growth using TMGa at 700 K, V/III=4) and in UHV [47]. Middle is the model of Creighton et al. (grey atoms:$GaCH_3$) [47], in the right the model of a disordered c(4x4) of Hicks et al. [34]*

6.1.7 (1x4)-CH_2 Reconstruction

Exposing a clean (2x4) reconstructed surface to methyl radicals and anneal it in UHV, one obtains a (1x4)-CH_2 reconstruction [47, 50]. The (1x4) symmetry [47, 50] and also the coverage with methylene groups (CH_2) [49, 50, 51] were measured on such prepared reconstructions in UHV.

During Atomic Layer Epitaxy (ALE), after exposure to TMGa, a similar RAS spectrum was reported by several groups [47, 52, 53] and sec. 6.4.2. In addition, this methylene covered surface was found to be very stable at elevated temperatures, in contrast to the methyl covered (1x2)-CH_3 reconstruction [47].

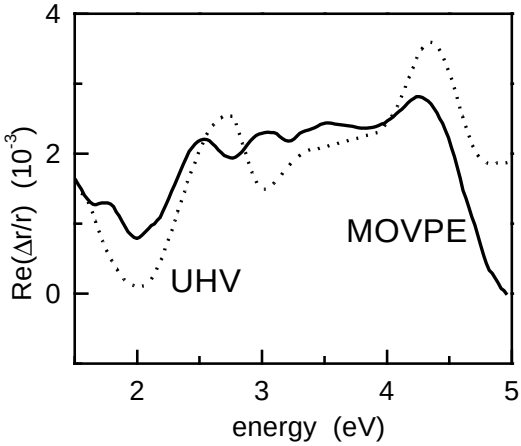

Figure 6.10: *RAS spectra of (1x4)-CH_2 in MOVPE (during growth using TMGa at 700 K, V/III=1) and in UHV [47].*

During ALE growth the surface changes between the arsenic rich (4x3) reconstruction during AsH_3 supply and this (1x4)-CH_2 reconstruction during TMGa supply. Since the resulting growth rate is exactly 1.0 monolayer (ML) per cycle, the difference in arsenic coverage of this reconstruction to a (4x3) is about one. Assuming an arsenic coverage of 1.75 ML for the (4x3) reconstruction, the (1x4)-CH_2 would have an arsenic coverage of about 0.75 ML. However, the structure is still unclear.

6.2 AsH_3 Stabilized Surfaces

The most arsenic rich surface obtained in MOVPE is the (4x3) reconstruction. The RAS spectra at room temperature of the (4x3) has a pronounced minimum at 2.8-2.9 eV (fig. 6.2). As figure 6.11 shows, the minimum of the RAS spectra shifts to lower energies at higher temperatures. Up to 750 K the shift is nearly linear, as the inset shows. This shift is simply caused by the increasing temperature, as the bands are broadening and therefore the gap gets smaller. ALso the amplitude of the RAS spectra gets smaller, due to the sma effect. At temperatures above 750 K the RAS minimum shifts away from the linear region to lower energies. The transition temperature depends on carrier gas (H_2 or N_2) (left hand side of fig. 6.11) and misorientation of the sample (right hand side).

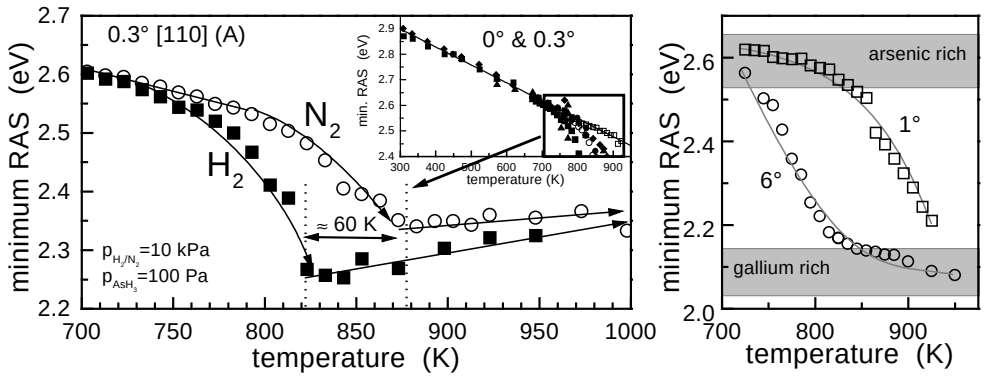

Figure 6.11: *Dependence of the minimum of the RAS spectra with temperature and carrier gas. The right hand side shows the shift of the RAS minimum for two misorientations (Points are average of three runs).*

This shift of the minimum of the RAS signal to lower energies can be explained by a transition form the very arsenic rich c(4x4)/(4x3) reconstructions (which have their minima around 2.6 eV at 700 K) to the less arsenic rich (2x4) reconstructions (a maximum at 2.6 eV), or even to gallium rich reconstructions like (nx6) and (4x2) (deep minima at 1.7 eV - 1.9 eV). However, the RAS spectra measured at 925 K do not resemble any well-ordered reconstruction. Such RAS spectra are best described by a linear combination of c(4x4), (2x4), and a small fraction of (4x2) domains on the surface.

Thus, according to figure 6.11 the surfaces become less arsenic rich at high temperatures, even though AsH_3 is completely decomposed at higher temperatures above 900 K (sec. 5 fig. 5.2). This change towards less arsenic rich surfaces is certainly due to an increased arsenic desorption, because the arsenic desorption increases exponentially with increasing temperature, but the arsenic flux to the surface remains constant as soon as the temperature for complete AsH_3 decomposition has been reached.

Interpreting figure 6.11 now in terms of desorption rate leads to two interesting conclusions:

1. The surfaces become less arsenic rich using hydrogen carrier gas. This effect is likely caused by etching from hydrogen radicals formed from the hydrogen carrier gas at higher temperatures. The same effect was also found during arsenic desorption (sec. 6.3.3) and gallium desorption (sec. 6.4.2)

2. With increasing misorientation and therefore a higher step-density, the surfaces become less arsenic rich. Thus, the steps promote arsenic desorption. An indication for steps as preferred desorption sites is also found during arsenic desorption, as discussed in the next section.

6.3 Arsenic Desorption

With increasing temperature six different desorption processes were encountered. They are named from process I to process VI and will be discussed in that order. A composition of three RAS measurements during arsenic desorption is shown in figure 6.12. More detailed RAS spectra and transients can be found in figures 6.13, 6.14, 6.17 and 6.18, showing typical RAS transients during arsenic desorption at temperatures of 773 K, 843 K and 963 K, and finally with nitrogen as carrier gas at 973 K. These RAS transients were usually measured at 2.65 eV photon energy.

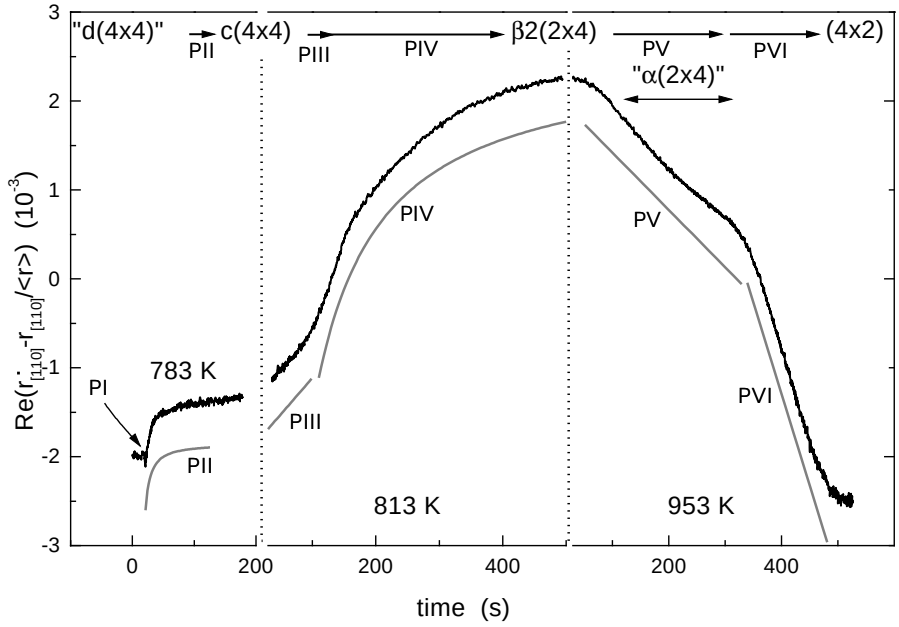

Figure 6.12: *Composition of three RAS transients measured at 2.65 eV during arsenic desorption at different temperatures, which shows all relevant processes under hydrogen carrier gas.*

6.3.1 Transition from (4x3) to c(4x4)

As the surface is essentially (4x3) covered at temperatures below 800 K, this is the starting surface of the arsenic desorption process. After switching off the AsH_3, the arsenic starts to desorb. During arsenic desorption, starting from the (4x3) reconstruction, the RAS signal showed first a small dip (process I) followed by an exponential change of the RAS signal (process II) (fig. 6.13). The RAS spectrum after 30 s desorption (end of process II) in figure 6.13 is very similar to the spectrum of a c(4x4) in MBE (light dots). Hence the (4x3) reconstruction must be more arsenic rich than the c(4x4) structure in this temperature range.

The small RAS signal change of process I is observed only between 700 and 800 K. This process is very fast (see fig. 6.13) and consequently the RAS signal change is influenced by the lock-in amplifier settings, preventing a fitting of the signal. Likely hydrogen adsorbates from the AsH_3 decomposition are responsible for this small dip.

The adsorption and desorption of hydrogen on GaAs (001) is well investigated (see [26] and references therein). On a (2x4) reconstruction hydrogen desorbs at temperatures above 460 K [26]. This agrees well with our finding, that after MOVPE growth and cooling to

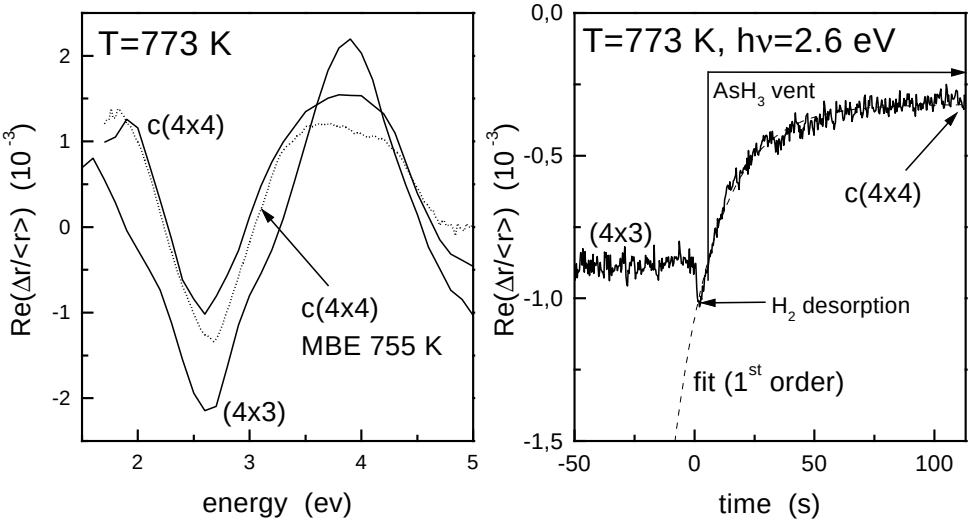

Figure 6.13: *RAS spectra before and during arsenic desorption in MOVPE, starting with arsenic stabilized (4x3).*

475 K with AsH_3 flowing, and after in-situ transfer to an UHV analysis chamber no As-H vibration could be detected by HREELS (sec. 6.1.1 fig. 6.3).

Therefore, any adsorbed hydrogen produced by decomposition of AsH_3 should have a very short life-time on the surface at 700-800 K, because hydrogen desorption is very fast at these temperatures. Below 700 K only very few AsH_3 is decomposed, and therefore no hydrogen reaches the surface. Therefore, the concentration of hydrogen on the surface decreases again. This explains why process I is observed only between 700 and 800 K. To summarize, process I is assigned to the fast desorption of hydrogen produced by the decomposition of AsH_3.

During process II the reconstruction is changing from (4x3) to c(4x4). Single wavelength Surface Photo Adsorption (SPA) measurements at 348 nm during arsenic desorption in MOVPE below 780 K have been explained in terms of a decreasing roughness by the desorption of excess non-dimerized arsenic [54]. The calculated activation energy of 2.57 eV shows reasonable agreement to the value of (2.36 ± 0.07) eV of this work (see fig. 6.19 and table 6.1). However, no traces of a higher roughness were measured on the (4x3) by ex-situ atomic force microscopy (AFM) and also no change of roughness in the in-situ ellipsometric signal during desorption was found. Thus the roughness assumption can be ruled out.

To conclude: after the fast desorption of hydrogen (process I) on a (4x3) reconstruction the surface changes to c(4x4) (process II). The desorbing species is likely As_4 [28]. The reaction order of one of this desorption process is an indication, that somehow the arsenic on the (4x3) reconstruction is organized in a way very similar to an As_4 cluster. The activation energy is (2.36 ± 0.07) eV (see fig. 6.19 and table 6.1).

6.3.2 Transition from c(4x4) to β2(2x4)

At temperatures exceeding 780 K further arsenic desorption from the c(4x4) is observed. First linearly with time (process III) and then exponentially (process IV) (fig. 6.14). The RAS signal changes sign and finally saturates. Figure 6.14 left shows the RAS spectrum at 923 K at that maximum. This spectrum completely resembles that of a β2(2x4) (fig. 6.6) recorded in MBE [55].

The first change (process III) of the RAS signal is attributed to the initial arsenic desorption from the c(4x4). This process is linear with time, as seen in figure 6.14. At a certain

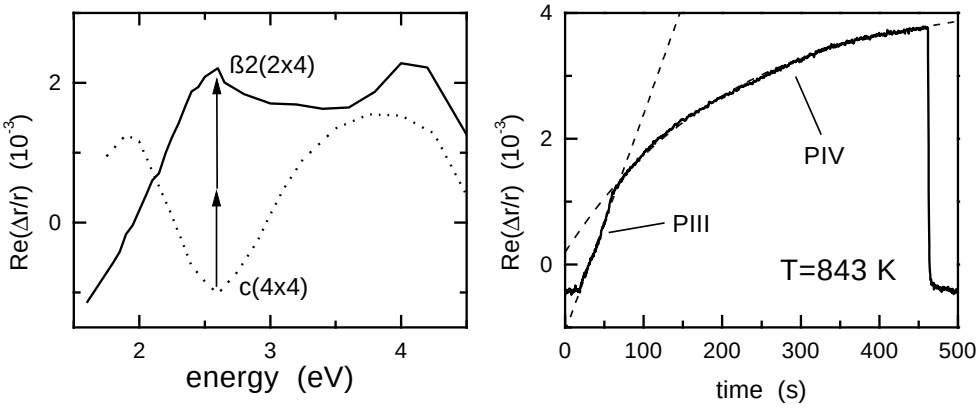

Figure 6.14: *RAS spectra and transients during arsenic desorption in MOVPE, starting from c(4x4).*

point the desorption mechanism is changing, the time dependence of the RAS signal is exponentially (process IV in fig. 6.14).

Two different processes during transition from c(4x4) to β2(2x4) have been reported in UHV experiments too [28, 29, 36]. By annealing the initial c(4x4) reconstruction the coherent c(4x4) domain size was not affected until β2(2x4) domains appeared. For this first desorption step As_4 [28] or As_2 [29] as main desorbing species were reported, dependent on the surface preparation (As_4 only with AsH_3 [28]).

When the arsenic coverage has reached about 1.0 monolayer the surface changes dramatically: c(4x4) domains are practically gone, but very small (2x4) domains appear [36] (see fig. 6.15). However, there is no long range order, and LEED shows only (1x1) symmetry [28]. STM images confirm this: At a certain temperature many very small or even incomplete β2(2x4) unit meshes can be measured [37] (upper fig. 6.15). After the complete transition to β2(2x4) (or c(4x4) respectively) the surface becomes smooth again [36, 37]. The desorbing species for this process is always As_2 [28, 29].

The linear time dependence (reaction order of zero), as observed for the initial desorption from the c(4x4) (process III), is somewhat unexpected, since arsenic desorbs as As_4 or As_2 molecules. If the formation of As_4 is the rate limiting step, a reaction order of one or even two is expected. It is second order, if the rate limiting step is the collision of two arsenic dimers on the surface to form As_4. Or, if the rate limiting step is the detachment of complete dimers from the surface, a reaction order of one (i.e. exponential time dependence) is expected.

A reaction order of zero usually involves an intermediate state. The occupation of this intermediate state is limiting the reaction speed and provides the necessary concentrations for the formation of the products (in this case arsenic clusters). Possible intermediate states/sites during arsenic desorption are steps (or kinks) at the surface. If arsenic mainly desorbs from step-edges, and diffusion of arsenic towards the steps is fast compared to the time the arsenic stays there until desorption, then the occupation of step-edges by the arsenic would limit the desorption rate. A higher step density would enhance arsenic desorption.

Actually this effect was observed on vicinal (001) surfaces in section 6.2: At higher misorientation angles (i.e. a higher density of step-edges) the surfaces became less arsenic rich. Furthermore, STM images measured during Migration Enhanced Epitaxy (MEE) growth of GaAs in MBE suggest a fast diffusion of complete As_2 dimers [56], which supports the above model of the step-edges as rate limiting steps during arsenic desorption and a fast diffusion of arsenic to the step-edges.

To conclude, the desorption of arsenic from the second layer on the c(4x4) reconstruction is limited by steps, kinks, or other active surface sites. The high concentration of arsenic

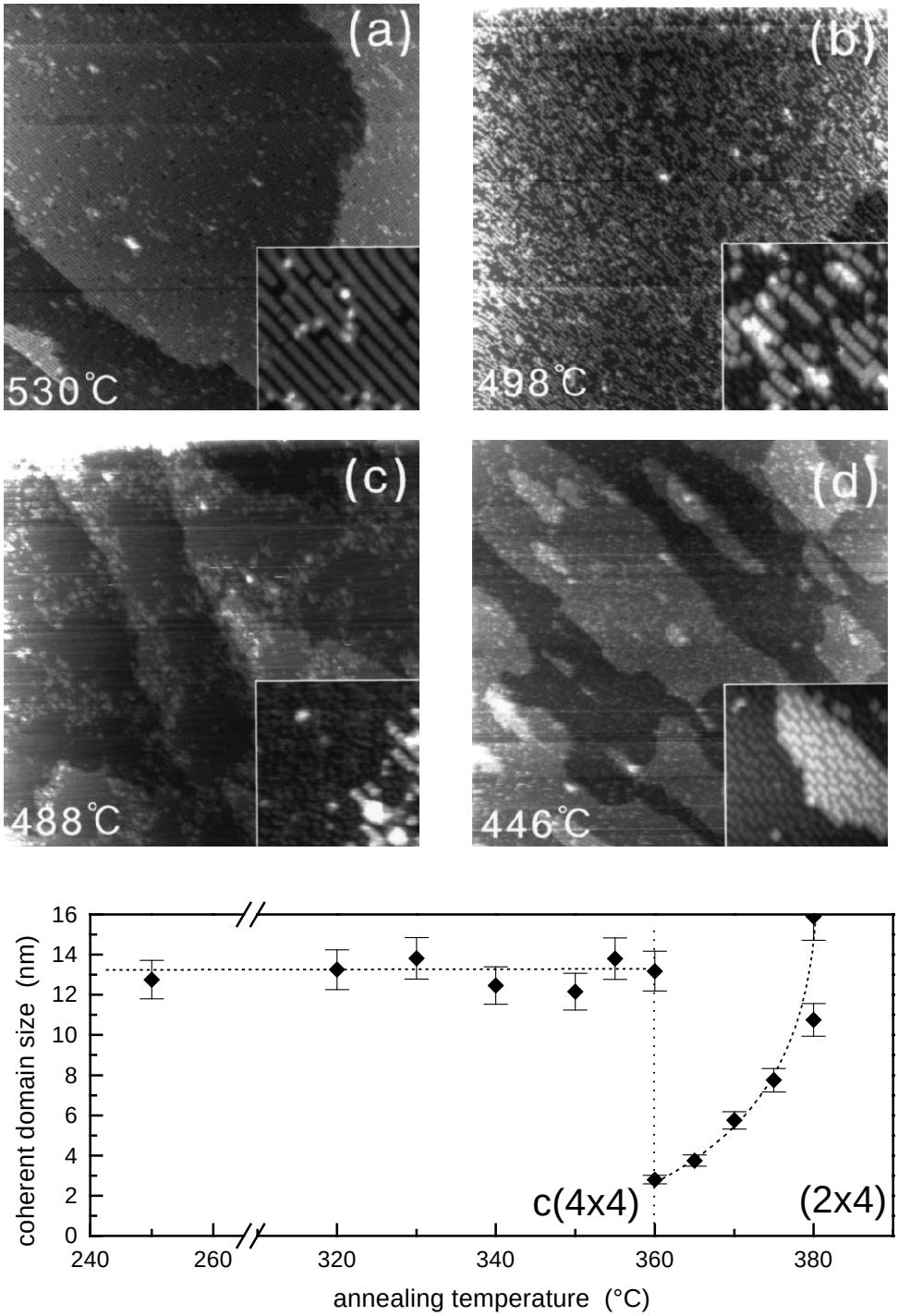

Figure 6.15: *Topography development during change from c(4x4) to β2(2x4) in MBE using STM (upper part [37]) and on decapped samples, measured by GIXD (lower part [36]). The temperature difference between both works is about 150°C.*

species at these sites can also explain the formerly observed desorption of As_4 [28]. At an arsenic surface coverage of about one monolayer the arsenic is bound more tightly, thus the diffusion of arsenic is hindered. Now the arsenic dimers desorb directly from the surface. Support for the above mechanism is the observed change of the desorbing species from As_4 to As_2 during desorption from c(4x4) to (2x4) [28]. From the RAS transients an arsenic coverage for this transition of about one monolayer is estimated, which agrees to TDS

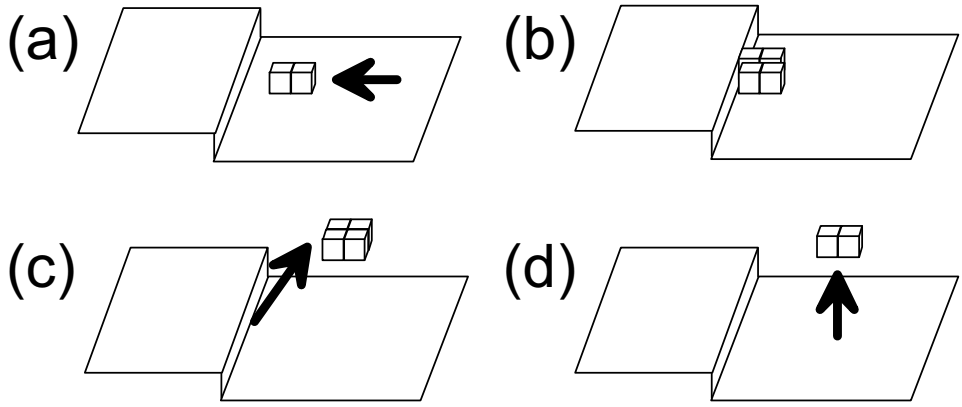

Figure 6.16: *The four different processes during arsenic desorption from c(4x4): (a) fast diffusion of dimers to the steps, (b) due to high concentration of As_2 at the steps formation of As_4, (c) As_4 desorbs (rate limiting step), (d) if the arsenic coverage is below one monolayer, arsenic dimers desorb directly.*

(Thermal Desorption Spectroscopy) measurements [28]. Figure 6.16 shows the desorption process systematically.

Fitting RAS transients for process III, the As_4 desorption from steps, an activation energy of (2.8 ± 0.3) eV was found (fig. 6.19 and table 6.1). For the desorption of deuterated arsine (AsD_3) from a c(4x4) under UHV conditions a smaller activation energy of 1.9 eV was measured by TDS [28]. However, there is an uncertainty due to TDS: both, the reaction order and a pre-exponential factor have to been known independently for doing the Redhead analysis in order to calculate an activation energy.

For process IV, where As_2 is assumed to desorb from the terraces and the reconstruction is changing towards β2(2x4) an activation energy of (2.79 ± 0.17) eV was found. Again TDS experiments reports the much smaller value of 2.0 eV [28].

SPA transient experiments of arsenic desorption in MOVPE at temperatures above 800 K were interpreted as two zero order desorption processes, first arsenic desorption from the c(4x4) and then a change towards a (2x4) reconstruction, with activation energies of 2.75 eV and 1.67 eV [54]. The first value is close to the value for process III of (2.8 ± 0.3) eV, while the value for process IV is much too small. However, if the same reaction orders as in the experiments in this work are assumed (i.e. a zero order reaction for process III and then a first order reaction), and after fitting the SPA transients given in reference [54] with exponential functions, an activation energy of (2.4 ± 0.2) eV is obtained, closer to the value for process IV of (2.79 ± 0.17) eV in table 6.1.

6.3.3 Desorption from β2(2x4)

The desorption from the β2(2x4) depends on the carrier gas. Using hydrogen as carrier gas and temperatures above 920 K causes the RAS signal to decrease linearly during desorption from the β2(2x4) reconstruction (process V) (fig. 6.17). At an anisotropy of about $0.4 \cdot 10^{-3}$ at 2.65 eV the slope changes (process VI) and finally the RAS signal saturates and does not change even after some minutes. Using nitrogen carrier gas only an exponential RAS signal change is observed (fig. 6.18). Even at very high temperatures exceeding 980 K no additional arsenic desorption process is found using nitrogen carrier gas.

The dotted RAS spectrum in figure 6.17 corresponds to a surface under hydrogen carrier gas 30 s after the RAS signal at 2.6 eV started to decrease again. The same RAS spectrum

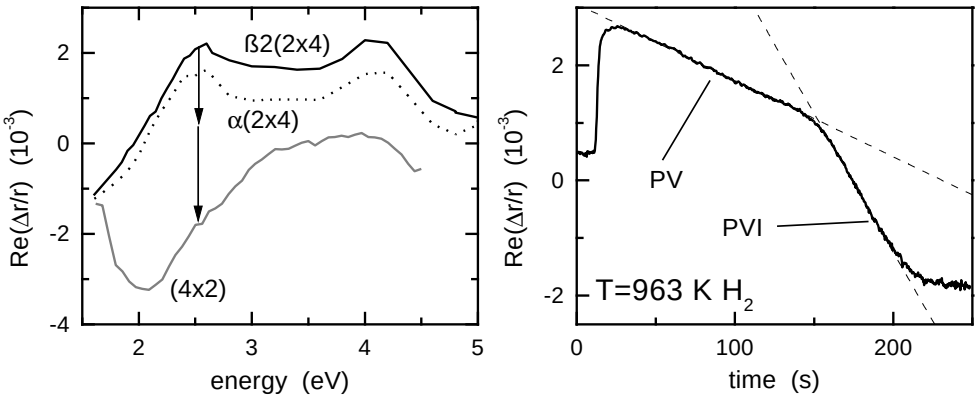

Figure 6.17: *RAS spectra and transient during arsenic desorption in MOVPE using hydrogen carrier gas, starting from β2(2x4).*

was the final spectrum during desorption with nitrogen (fig. 6.18). This spectrum is very similar to an RAS spectrum of an α(2x4) during MBE (fig. 6.6). However, with hydrogen carrier gas there is further arsenic desorption until the process changes. The final RAS spectrum obtained under hydrogen carrier gas is shown in figure 6.17 (T=968 K, dashed line). It clearly resembles the RAS spectrum of a (4x2) reconstruction in MBE (fig. 6.8) [42].

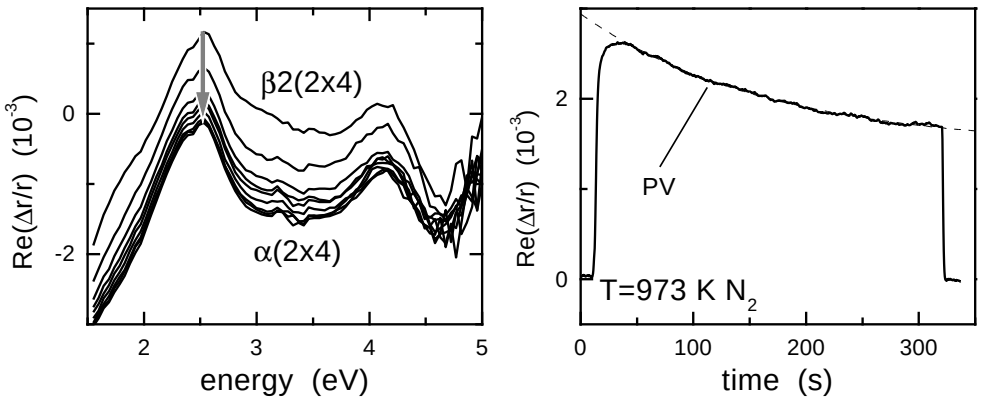

Figure 6.18: *Development of RAS spectra (every 90 s) during arsenic desorption in MOVPE using nitrogen carrier gas, starting from β2(2x4).*

The different processes and reaction orders of arsenic desorption under hydrogen carrier gas compared to nitrogen carrier gas are related to the hydrogen, most likely due to the onset of formation of hydrogen radicals from the hydrogen carrier gas itself above ≈900 K. These hydrogen radicals induce arsenic desorption by the formation of AsH_x molecules; the hydrogen radicals from the carrier gas are etching the arsenic. This assumption could also explain why the surfaces are less arsenic rich with hydrogen carrier gas at higher temperatures compared to nitrogen as carrier gas, as observed in section 6.2.

Therefore, the change of reconstruction during arsenic desorption is simply caused by an etching of the arsenic by the hydrogen radicals. The arsenic coverage (and thus the RAS signal) is changing linearly with time because the rate of hydrogen radical formation and thus the etching rate is constant at a constant temperature.

Using hydrogen as carrier gas the desorption process V from β2(2x4) has an activation energy of (2.4 ± 0.3) eV and is linear with time (zero order). However, as discussed above, this might not be due to desorption from active surface sites, but due to hydrogen radical induced etching. Thus the activation energy is probably related to the formation of AsH_x.

At an RAS signal close to zero (at 2.65 eV) the surface is entirely covered by α(2x4), and the transition to the next more gallium rich surface starts. The further change in the RAS signal (process VI) therefore reflects the etching of the last surface layer of arsenic and the formation of gallium dimers. This final change towards the (4x2) is again linear with time. Just shortly before the signal saturates there is a small curvature. Since the exact nature of the surface at this time is unknown, the possibility of another process shortly before saturation cannot be excluded. Furthermore, the structure of the surface when the desorption behavior changes is not known; it might be a (nx6)-like reconstruction, as claimed in [44].

Fitting this second linear part for the change towards (4x2) yields an activation energy of (2.8 ± 0.2) eV (fig. 6.19). This energy is slightly higher than the activation energies for the previous processes, reflecting the stronger binding of these final arsenic atoms.

However, the "true" process V with exponential As_2 desorption is only observed with nitrogen carrier gas. The very small unavoidable arsenic background pressure of the MOVPE reaction seems to be enough to stabilize the final α(2x4) up to at least 1000 K. The activation energy of (2.7 ± 0.2) eV is close to the values of the other processes.

6.3.4 Summary of Arsenic Desorption

The obtained reaction rates for all desorption processes are shown in figure 6.19. The calculated activation energies from these data are compared to values in literature measured with SPA and TDS in table 6.1.

The reaction rates under hydrogen and nitrogen carrier in figure 6.19 are essentially the same. However, in general the activation energies using nitrogen carrier gas are smaller. But the nitrogen data were measured mostly in a single run, while the data using hydrogen carrier gas are from about 10 runs between 1995 and 1999. Therefore, the error bars for the nitrogen data are probably too small, and any deviations in the activation energies between nitrogen carrier and hydrogen carrier gas are probably due to lack of measurements using nitrogen carrier gas.

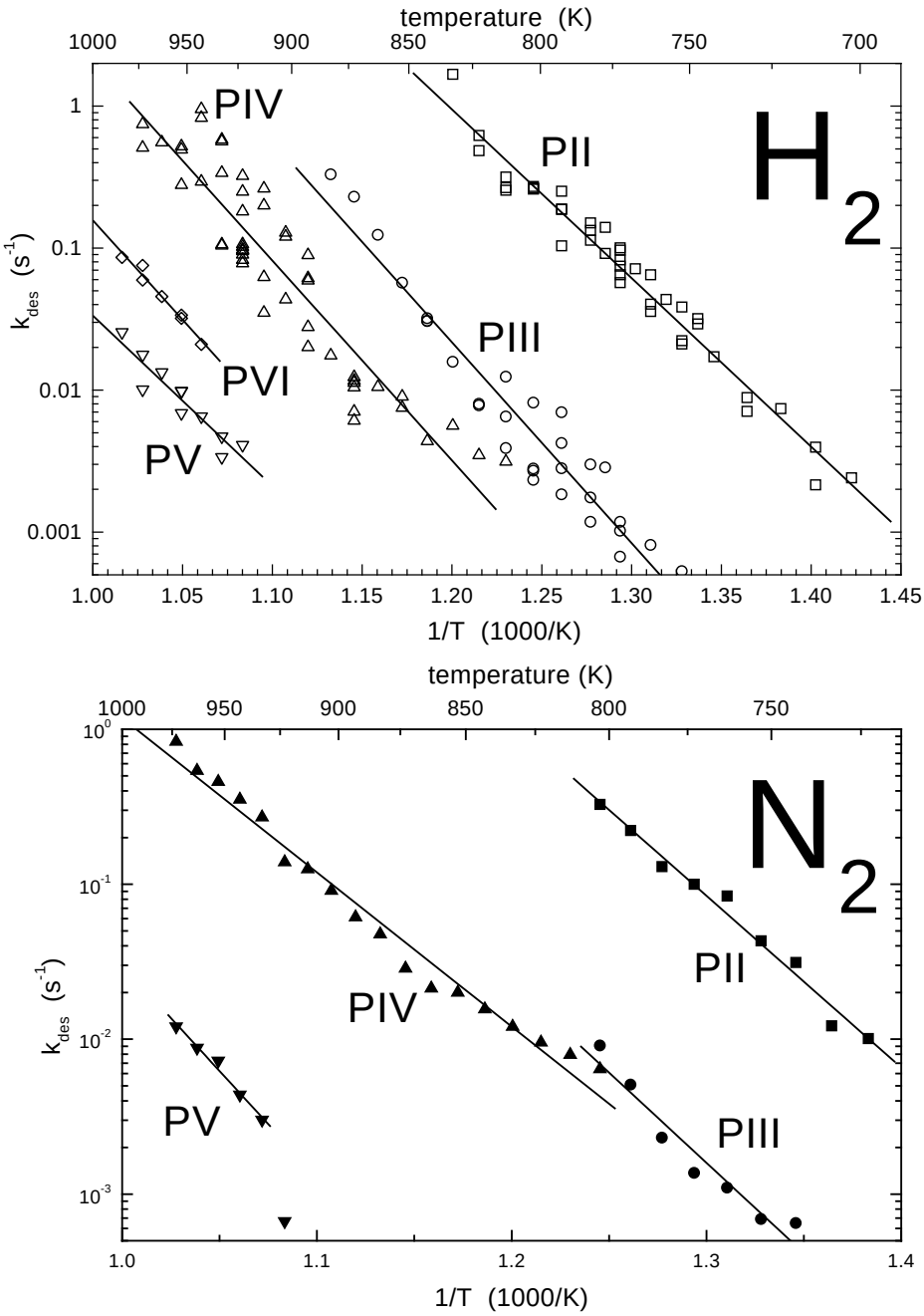

Figure 6.19: *The rate constants of the different processes with hydrogen carrier gas (upper) and nitrogen carrier gas (lower) are plotted on a logarithmic scale above the reciprocal temperatures (Arrhenius plot). The ascent of the obtained lines are the activation energies for these processes.*

process		activation energy (eV)			reaction	desorbing
		by RAS	by TDS[1]	by SPA	order	species
no.	name	(MOVPE)	(UHV)[28]	(MOVPE)[54]		[28]
		with hydrogen carrier gas				
I.	H-desorption	too fast			?	H_2?
II.	to c(4x4)	(2.36 ± 0.07)		2.57	1.	As_4
III.	from c(4x4)	(2.8 ± 0.3)	1.9	2.75	0.	As_4
IV.	to β2(2x4)	(2.79 ± 0.17)	2.0	1.67 (2.4 ± 0.2)[2]	1.	As_2
V.	from β2(2x4)	(2.79 ± 0.17)	2.3		0.	AsH_x?
VI.	to (4x2)	(2.8 ± 0.2)			0.	unknown
		with nitrogen carrier gas				
I.	H-desorption	too fast			?	H_2?
II.	to c(4x4)	(2.20 ± 0.11)			1.	As_4
III.	from c(4x4)	(2.3 ± 0.3)	1.9		0.	As_4
IV.	to β2(2x4)	(1.98 ± 0.07)	2.0		1.	As_2
V.	from β2(2x4)	(2.7 ± 0.2)	2.3		1.	As_2
VI.	to (4x2)	not observed				

[1] Thermal Desorption Spectroscopy (TDS) of AsD_3 under UHV-conditions [28] with a ν_1 assumed to be $10^{13}\,s^{-1}$ and reaction order to be always one. Therefore, all the values may be off by some factor. The desorbing species are also taken from this reference with regard to temperature and reconstruction.

[2] The value of 2.4 eV was obtained by fitting Surface Photo Adsorption (SPA) transients given in [54] with exponentials.

Table 6.1: *Activation energies and reaction orders of the different arsenic desorption processes on the (001) surface.*

6.4 TEGa/TMGA Adsorption/Desorption

Pulsed supply of TMGa (or TEGa) is used for two purposes. The first one is growth in the self-limiting Atomic Layer Epitaxy (ALE) growth mode, i.e. growth using alternating supply of TMGa and AsH_3. In this mode the growth rate is limited to one monolayer per cycle, due to adsorbates from the decomposition of the TMGa still sticking to the surface. This limitation will be discussed in detail in this section. The second usage of pulsed supplies is for delta doping (i.e. creating a thin layer with a high carrier concentration), when a short pulse is offered to the surface at about 900 K. However, doping will be discussed later on in section 6.7.

6.4.1 TEGa Adsorption

Using TEGa it is impossible to achieve self-limiting ALE growth (see e.g. [53]). Figure 6.20 shows the development of the surface during a short ALE sequence at 775 K. At this temperature TEGa is completely decomposed, and thus pure gallium or gallium-hydrides are supplied to the surface.

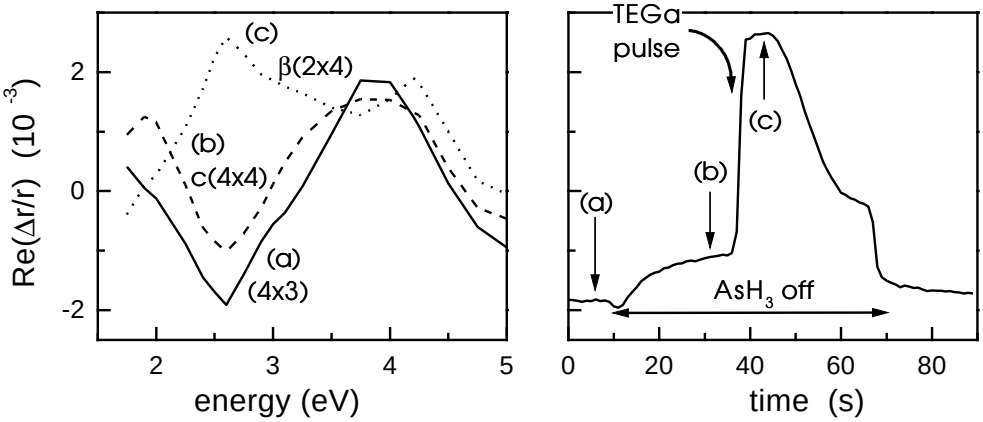

Figure 6.20: *Development of RAS spectra before and after a short TEGa pulse at 775 K (RAS transient at 2.6 eV).*

During the first 30 s purging with hydrogen the reconstruction changes from (4x3) to c(4x4) (already discussed in section 6.3.1). Then after the short TEGa pulse the reconstruction changes to β2(2x4). After some time the residual arsenic evaporates from the walls and the susceptor and the surface changes gradually back towards c(4x4). Finally the AsH_3 is switched on again and the reconstruction transforms into (4x3).

If the amount of TEGa is not too high (i.e. the pulse is short enough) the surface changes from c(4x4) (arsenic coverage 1.75 ML) to β2(2x4) (0.75 ML), resulting in a growth rate of about one monolayer per cycle. However, this mechanism is not self-limiting (e.g. see [53]) and relies on well-chosen switching times.

6.4.2 TMGa Adsorption

Atomic Layer Epitaxy Regime (T$<$750 K)

ALE growth is done by alternately supply TMGa or AsH_3 to the MOVPE reactor at temperatures below 750 K. By doing ALE using TMGa on a (001) surface a self-limiting growth rate of one monolayer per cycle is achieved [57].

ALE growth has been studied thoroughly using RAS [47, 52, 53]. In the first step, after AsH_3 is switched to the vent, TMGa is offered to the surface. At the low temperatures during ALE the decomposition of TMGa is incomplete, and mono-methyl-gallium (MMGa, $GaCH_3$) and even TMGa reaches the surface.

The methyl groups of the adsorbed and partly decomposed TMGa and MMGa do not go off spontaneously. Instead they need atomic hydrogen to desorb, usually delivered by the AsH_3. Without AsH_3, the methyl groups stick much longer to the surface. Some of them can form methane and subsequently evaporate by stealing from other methyl groups, which were reduced to methylene (CH_2).

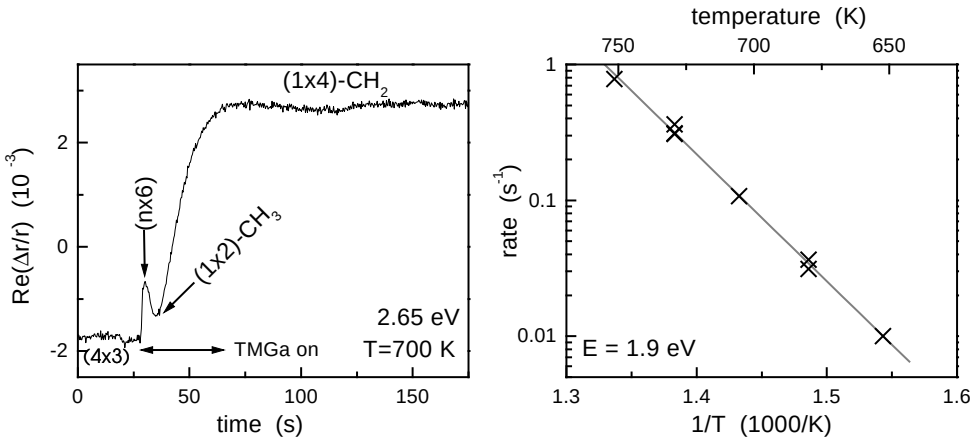

Figure 6.21: *RAS transient at 2.65 eV during TMGa adsorption at 700 K and Arrhenius plot.*

Using UHV techniques [47, 50, 51] and also in-situ RAS [47, 52, 53] the reconstruction prepared by exposing a (001) surface at low temperatures to TMGa was identified as (1x4)-CH_2 reconstruction, which was discussed in section 6.1.7. This reconstruction, probably due to its methylene bonds, is very stable [47] as it can be also seen in figure 6.21: the RAS signal did not change, even when the TMGa was switched off.

The RAS transient in figure 6.21 shows some rise and falls, which can be correlated to several different reconstructions. After switching off the AsH_3 and then switching on the TMGa the surface first changes to (nx6) (small maximum), then to (1x2)-CH_3 (minimum) and finally exponentially to a (1x4)-CH_2 reconstruction (final maximum). This is very similar to the the reconstructions found during growth. (This will be discussed in the following section 6.5.)

This final RAS signal change from (1x2)-CH_3 to (1x4)-CH_2 is slow enough to be fitted. It shows an exponential time dependence (first order reaction) and an activation energy around 1.9 eV. The change is likely limited by the break down of the methyl groups (from CH_3 to CH_2) and the bond rearrangement on the surface.

As mentioned before, the (1x4)-CH_2 is inert against further TMGa adsorption. It is even possible to cool a sample down from 750 K to room temperature with TMGa flowing without getting gallium droplets, as it was done in figure 6.22. The resulting RAS spectrum is somewhat similar to a (2x4) spectrum (see fig. 6.6). However, there are important differences: β2(2x4) has no RAS signal below zero, the RAS spectrum has three more or less distinct structures between 2.5 eV and 4.3 eV. Finally, the β2(2x4) RAS spectrum at the E_1 transition (2.96 eV) is more anisotropic than the structure at E_0'(4.44 eV) in contrast to the (1x4)-CH_2 spectrum in figure 6.22.

A mentioned earlier, the structure of this surface is still unknown. Clearly the presence of methylene groups suggests methylene bridging bonds between different atoms on the surface. Secondly the arsenic net coverage must be around 0.5-0.75 ML, since ALE growth

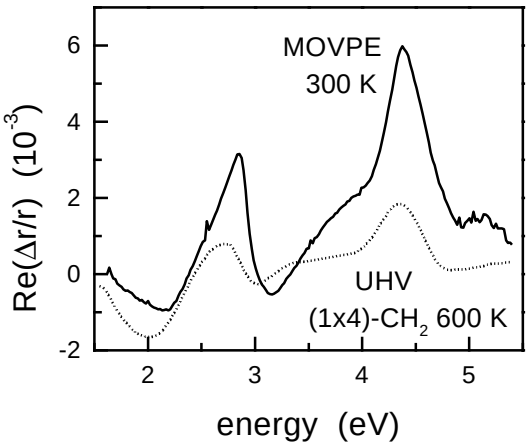

Figure 6.22: *RAS spectrum after cooling from 875 K to room temperature without AsH_3 but TMGa flowing until 575 K (UHV [47]).*

(i.e. changing between (4x3)/c(4x4) and (1x4)-CH_2) results in a growth rate of exactly one monolayer GaAs per cycle.

At high temperatures (T>900 K)

At high temperatures above 900 K the surface transforms rapidly into β2(2x4) without AsH_3 stabilization. Thus, it is expected that an additional supply of TMGa yields an even more gallium rich reconstruction. Figure 6.23 shows the RAS spectra and transients of such an experiment. When a short pulse of TMGa is fed into the reactor the β2(2x4) (created by arsenic desorption) changes to a (4x2) reconstruction. The right hand side of figure 6.23 shows RAS transients for runs with different lengths of the TMGa pulse.

The growth rate measured by RAS signal oscillations at 773 K was 0.547 ML/s. At least this amount of gallium was delivered to the surface at higher temperatures. From figure 6.24 the mean pulse duration for a complete change to (4x2) was found to be (1.59±0.07) s. Thus, the amount of gallium needed to change the β2(2x4) into (4x2) was about $0.547\,\frac{ML}{s} \cdot 1.59\,s = 0.85$ ML.

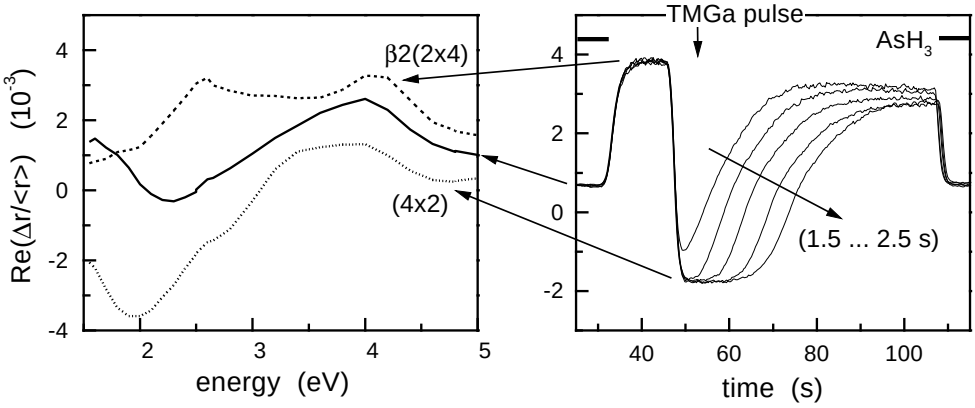

Figure 6.23: *RAS spectra measured before, during and after a TMGa pulse (left) and RAS transients at 2.65 eV of TMGa pulses of different durations (right) at 923 K.*

As it can be seen in figure 6.23 the (4x2) reconstruction vanishes after some time. This recovery time depends linearly on the length of the TMGa pulse (fig. 6.24). If the amount of TMGa exceeded more than 2.5 s (i.e. more than a monolayer), the recovery times did

not increase any further but the surface became rough. This behavior is an indication of the existence of a more gallium rich reconstruction, possibly consisting of gallium droplets between a proper (4x2) reconstruction, as proposed in [46].

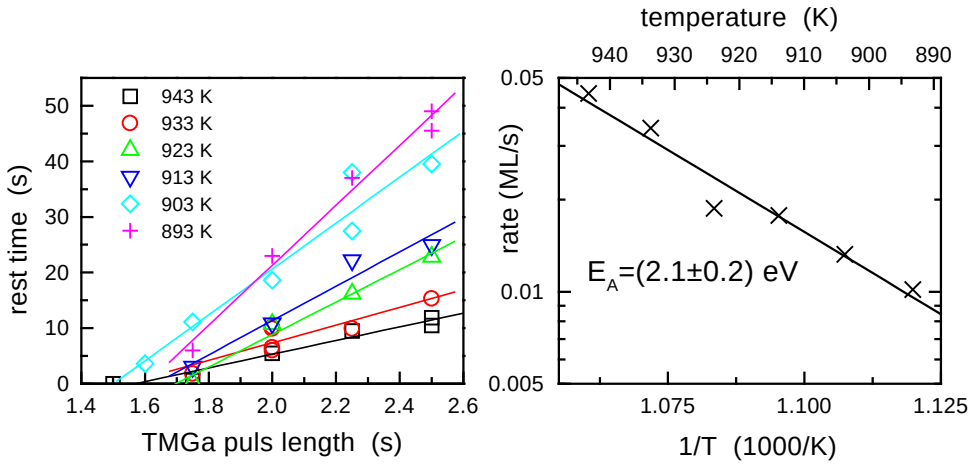

Figure 6.24: *Time of existence of the (4x2) (left) and calculated desorption rates from the data (right).*

From the time the gallium rich reconstruction remains stabilized by the excess gallium on the surface, the gallium desorption rates can be calculated, because the amount of excess gallium offered to the surface and the time it takes to desorb the gallium are known. The right hand side of figure 6.24 shows an Arrhenius plot of the desorption rates of gallium calculated from the lines in the left hand diagram. The activation energy for gallium desorption of 2.1 eV is surprisingly low, compared to the activation energy of 2.5 eV for arsenic desorption (measured in the previous section 6.3). This may be due to the desorbing TMGa being only weakly bound into clusters on the gallium rich (4x2) surface. However, there is also a second explanation. As stated earlier in sections 6.2 and 6.3.3, the hydrogen carrier gas seems to etch the surface at these high temperatures. Thus the desorption rate might be an etching rate instead.

However, the rate is very slow, whether gallium is desorbing or etched by hydrogen, below 0.05 monolayer per second, even at 950 K. Actual rates on less gallium rich reconstructions are most likely even smaller, because on these reconstructions the gallium is bound more tightly. Therefore, gallium desorption is not an important issue for MOVPE growth at temperatures below 975 K.

6.4.3 Summary of TEGa/TMGa Adsorption

The different decomposition pathway of the gallium precursor is reflected by their adsorption behavior. TEGa is decomposed at about 600 K mostly into GaH_x. Thus TEGa adsorption leads to the formation of a (2x4) reconstruction, even at low temperatures. On the other hand TMGa adsorption at low temperatures results in a methylene covered inert surface. Only at very high temperatures when TMGa is completely decomposed, a clean (4x2) reconstruction can be prepared by TMGa adsorption on β2(2x4).

6.5 Surfaces During Growth

Contrary to the results in MBE (i.e. fig. 6.1 from [25]) no long range symmetry exists during growth in an MOVPE reactor, apart from a very disordered (1x2) symmetry [48]. However, the RAS spectra give strong indications to the presence of small reconstruction "sub-units", which on the whole yield RAS spectra close to those of well-ordered surfaces.

Growing with TEGa three characteristic RAS spectra (fig. 6.25) were found, which correspond well to those found during growth using TMGa. Using TMGa at lower temperatures and very low V/III ratios[1] another fourth phase was found. Its spectrum is plotted in fig 6.10.

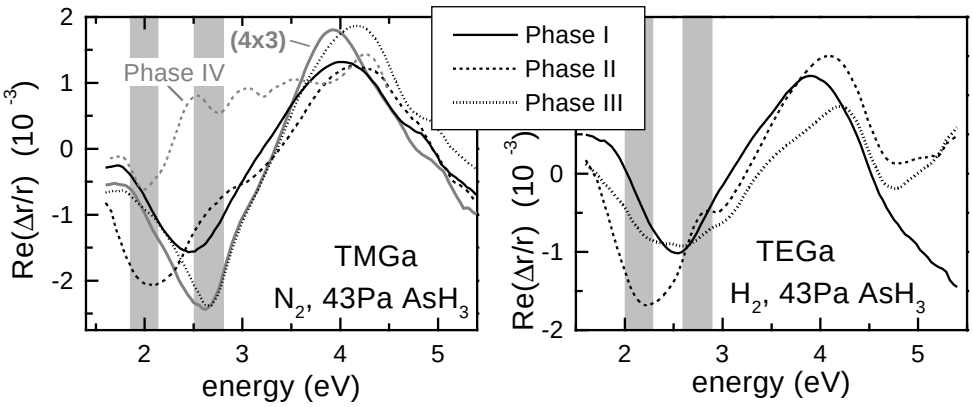

Figure 6.25: *typical RAS spectra during growth using TMGa and TEGa (right). The bars mark the typical regions of the RAS minimum for gallium rich (≈2 eV) and arsenic rich (≈2.6 eV) reconstructions.*

To obtain the phase diagrams shown in figures 6.26 and 6.27, RAS spectra at a large variety of growth conditions have been measured. However, it was not possible to measure at TMGa fluxes of more than 13 Pa due to technical limitations. To obtain spectra at lower V/III ratios, the TMGa partial pressure was fixed at 5 Pa and then the AsH_3 partial pressure was changed (solid symbols in fig. 6.26). Each measured RAS spectrum was assigned to a phase using the following criteria:

Phase I Pre-growth and during growth surfaces are identical; the during growth spectrum might be slightly damped.

Phase II The RAS minimum is shifted to lower photon energies (more (nx6)-like spectra).

Phase III The RAS minimum is shifted back to the value of the starting surface, but now the RAS minimum is narrower, and the maximum is shifted more into the UV range.

Phase IV At very low V/III ratios there is no proper RAS signal minimum at all, and the RAS spectra resemble that of a (1x4)-CH_2 (fig. 6.10).

Figure 6.26 shows the phase diagram for the growth of GaAs (001) using either TMGa or TEGa. Although TEGa features three phases with similar RAS spectra as TMGa (see fig. 6.25), the phase boundaries are shifted by 100-150 K to lower temperatures. On the other hand, using nitrogen carrier gas (see also [58]) or growing on a vicinal substrate (for

[1] Growth using TEGa was not investigated at V/III ratios below 10, therefore the existence of a fourth phase using TEGa cannot be ruled out. However, TEGa decomposes via $\beta-$Elimination forming GaH_x (discussed in sec. 5) thus the existence of an completely adsorbate limited phase is very unlikely.

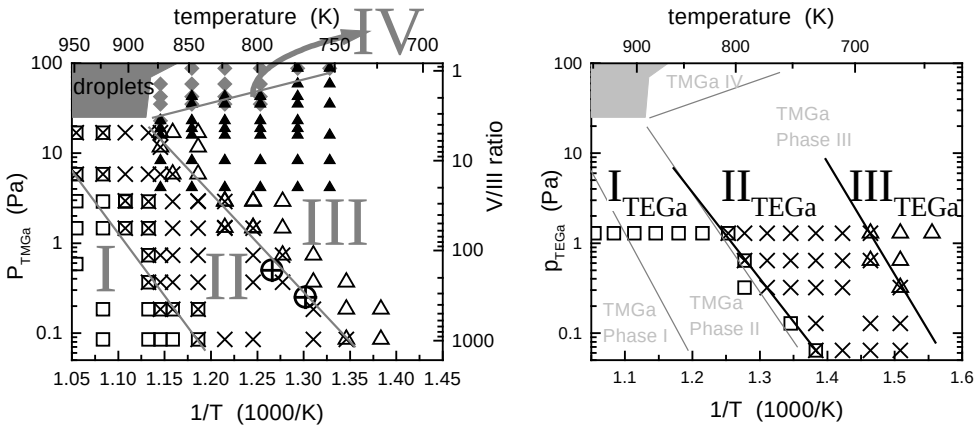

Figure 6.26: *Phase diagram during growth using TMGa (left, H_2 10 kPa & AsH_3 83 Pa) or TEGa (right, N_2 10 kPa & AsH_3 43 Pa). At the crossed circles the growth rate starts to decrease (from data in fig. 5.3 right side).*

additional phase diagrams see [59]) does not change the phase boundaries within an uncertainty of 20 K. Even on the (113) surface and using TMGa the phase boundaries are comparable (sec. 8.3 fig. 8.5). Thus the phase boundaries are strongly related only to the gallium precursor.

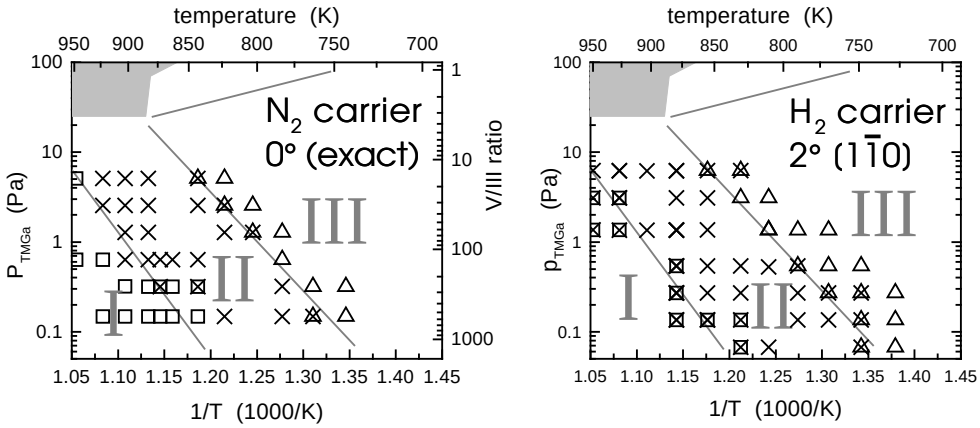

Figure 6.27: *Phase diagram during growth using TMGa and nitrogen carrier gas on an exact oriented substrate (left), and using hydrogen carrier gas and a 2°[1$\bar{1}$0] vicinal substrate (right). The other parameters are 10 kPa carrier gas and 83 Pa AsH_3. The phase boundaries in gray are for GaAs (001) exactly oriented H_2 carrier gas, as shown in figure 6.26*

At higher temperatures and low gallium partial pressures (high V/III ratios) the RAS spectrum does not change upon initiating growth. The arsenic stabilized surface and the surface during growth are in quasi equilibrium and the growth rate is small compared to the decomposition and adsorption rates. All arriving TMGa is instantaneously decomposed, incorporated and covered again by arsenic. Thus, pre-growth and during growth surface are identical.

During growth in phase II the RAS spectra show more contributions of gallium rich reconstructions, i.e. more contributions of (nx6) domains. This can be clearly seen in figure 6.34, where dark areas indicate a strong difference of (nx6) area coverage between pre-growth and during growth surfaces. The gallium dimers typical for the (nx6) reconstruction are likely located at the step-edges, because step-edges are preferred sites for gallium in-

corporation, simply because here atoms have a higher number of nearest neighbors. The previous sections 6.2 and 6.3.2 showed that step-edges are also sites of enhanced arsenic desorption which makes them additionally gallium rich.

For the origin of phases II there is a very simple explanation: in the intermediate temperature range the decomposition of the TMGa/TEGa precursor is 100 % (sec. 5 fig. 5.1). However, only a small part of the AsH_3 is decomposed (sec. 5 fig. 5.2), thus the incorporated gallium is not immediately covered by arsenic. Consequently the during growth surfaces are more gallium rich than the pre-growth surfaces.

This mechanism is certainly true for growth using TEGa, since TEGa is essentially decomposed above 600 K while AsH_3 is not. However, using TMGa phase II extends about 120 K higher in temperature than by using TEGa, even though the AsH_3 decomposition is not influenced that much by the different gallium precursors.

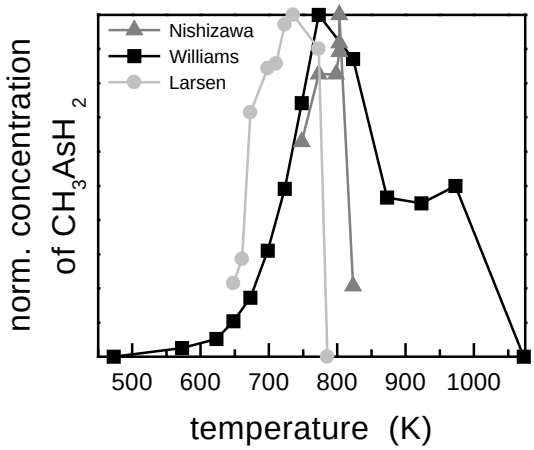

Figure 6.28: *Production of mono- or di-methl arsine ($(CH_3)_xAsH_{3-x}$) during MOVPE growth measured by IR-adsorption and mass spectroscopy (Nishizawa (IR) [60], Armstrong (IR+MS) [61], Larsen (MS) [15]).*

The main difference between TMGa and TEGa is their decomposition mechanism. While TEGa decomposes via $\beta-$elimination and therefore GaH_x is delivered to the surface, TMGa decomposes in the vapor phase only up to $GaCH_3$ (mono-methyl-gallium). Therefore many methyl groups are supplied to the surface during growth using TMGa. Somehow the methyl groups from the TMGa must induce less arsenic rich surfaces. A possible mechanism is the formation of methyl arsines on the surface, which desorbs. The following mechanism is proposed in detail:

1. Partly decomposed TMGa (mostly (CH_3)Ga: and $(CH_3)_2$Ga·) reaches the surface and diffuses to the step-edges.

2. AsH_3 is adsorbed, only partly decomposed, as AsH_x (x=0..3).

3. At the step-edges, the $(CH_3)_x$Ga is incorporated, and the leftover methyl groups still stick to the surface, close to a step-edge.

4. Partly decomposed AsH_x meets the methyl groups at the step-edges. Adsorbed AsH_2 and AsH has two possibilities: either it transfers an hydrogen atom to a methyl group, forming methane (CH_4) which then desorbs, or it forms mono- and di-methyl arsines ($(CH_3)_xAsH_{3-x}$) which also desorbs.

Thus, the methyl groups of the TMGa would induce the formation of methyl arsines. As a result less arsenic is incorporated, because of increased arsenic desorption. This mechanism is only possible at temperatures below the decomposition temperature of tri-methyl arsine (TMAs), i.e. below 850-900 K.

There is experimental evidence of the formation of methyl arsines. In TMGa decomposition studies also the formation of mono-methyl-arsenic (CH_3AsH_2) was observed [61, 15, 60]. Figure 6.28 shows the measured production of methyl arsines as a function of temperature. The temperature range is limited to lower temperature by the onset of TMGa decomposition and to higher temperatures by the onset of TMAs decomposition at about 850-900 K.

However, the partial pressure of the methyl arsines were low, less than 10 % and the partial pressure decreases strongly at total reactor pressures higher than 100 Pa [19], which would make this process less favorable at the typical 2-10 kPa reactor pressures used during MOVPE growth. Thus, this process was neglected for the analysis, since it was certainly not a major pathway of decomposition. On the other hand the formation of methyl arsines as described would be expected to be only a minor process, if it solely happens on the surface, and concentrations of less than a percent are expected then.

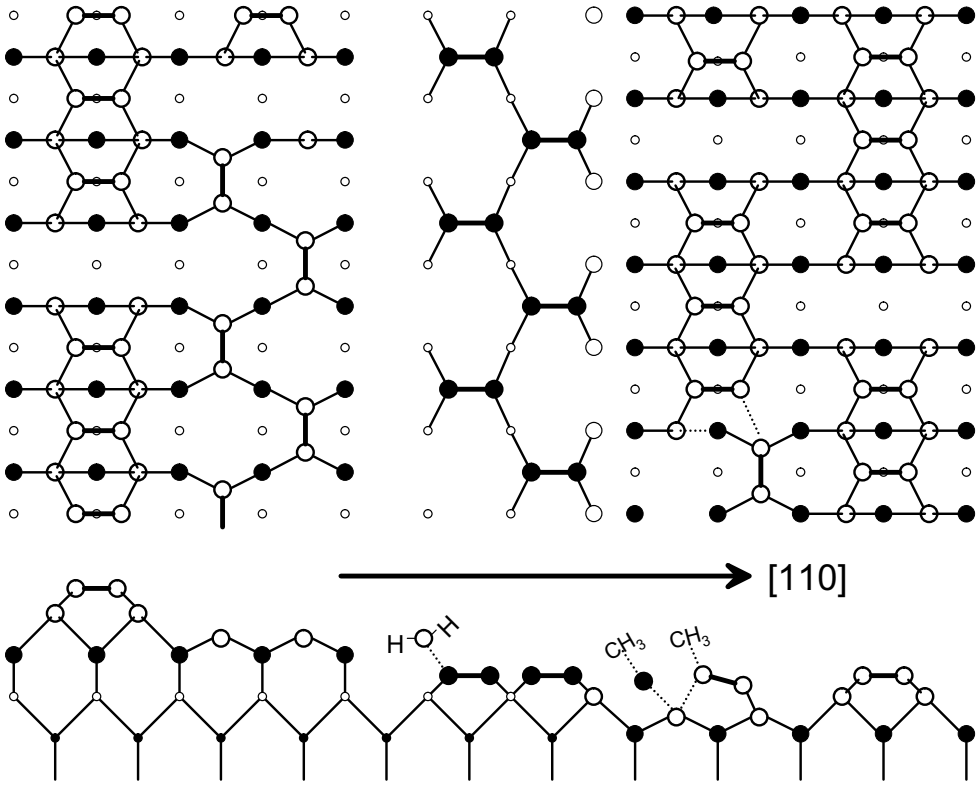

Figure 6.29: *Model of the atomic configuration of a step-edge in [110] direction during MOVPE growth using AsH_3 and TMGa.*

Another important conclusion can be drawn from this model: Close to step-edges the surface is gallium rich, because on the one hand the step edges are the place the gallium is incorporated. On the other hand the arsenic desorption is increased by the left-over methyl goups.

Putting all this together, the model of a step shown in figure 6.29 can be deduced. First, directly at the step, there is a region of gallium dimers, arranged like in (nx6) or (4x2). Next

comes a region, where the surface is only covered by a single arsenic dimer layer, like a (2x4). Then finally comes the terrace region, which is c(4x4) or (4x3) covered.

The origin of phase III is much better understood. In this regime the growth rate decreases with decreasing temperature, as can be seen from figure 5.3. Therefore, phase III belongs to the kinetic limited growth regime. The decreasing growth rate is due to the incomplete decomposition of the precursors, and subsequently the surface is covered with adsorbates. Using TMGa a (1x2)-CH_3 reconstruction appears (see sec. 6.1.6), and the desorption rate of the methyl groups is limiting the growth rate.

The desorption rate of the adsorbates is an activated process (i.e. have an activation energy barrier). Therefore, the partial pressure dependence of the transition between phase II and III shows an exponential temperature dependency: A higher partial pressure means a higher supply rate of adsorbates and thus a higher desorption rate of the adsorbates (i.e. higher temperature) is needed to maintain the same coverage.

Finally, using TMGa and very low III/V ratios (< 1), another characteristic RAS spectrum appears. The RAS spectrum of this phase IV is similar to that of the (1x4)-CH_2 reconstruction, also found during ALE growth which was discussed in the previous section 6.4.2. During growth in phase IV at low V/III ratios there seems to be not enough hydrogen from the AsH_3 to desorb the methyl groups before their are reduced to methylene, which is very stable. Growth at such low V/III ratios is used for intrinsic carbon doping which will be discussed in section 6.7.

To summarize, during growth at normal V/III rates (i.e. larger than 5) three different typical surfaces appear. At high temperatures in phase I the kinetics are much faster than the growth rates and the surfaces during growth is identical to the pre-growth surfaces. At intermediate temperatures in phase II more gallium rich surfaces appear, the gallium is located at the step-edges. This surface is either due to incomplete AsH_3 decomposition (when growing with TEGa) or due to forced arsenic desorption by the formation of methyl arsines (when growing with TMGa). Finally, at low temperatures in phase III the precursor are not decomposed, and the surface is covered by adsorbates.

6.6 Gallium Species Surface Diffusion

The next two sections will deal with diffusion of gallium species during growth with TMGa and AsH_3. The first section uses the "classical" approach of MBE, the transition between 2D island nucleation growth mode and step-flow growth mode. The second section determines diffusion lengths by step-bunching.

6.6.1 2D Island Nucleation Growth ↔ Step-flow Growth

At lower temperatures (725-850 K) RAS signal oscillations can be observed during growth (fig. 6.30) [62]. These oscillations have a period of exactly one monolayer. They can be found for a wide range of parameters; in fact it was used regularly in this work to check the growth rate of the MOVPE system.

The RAS signal oscillations seem to be correlated to 2D island nucleation growth mode, which is discussed in detail in section 3.2.1 and figure 3.2. In 2D island nucleation growth mode the surface alternates between a rougher state with many small islands (after 0.1 to 0.6 monolayer growth) and a smooth state (after 0.7 to 1.0 monolayer growth) with only a few very large islands.

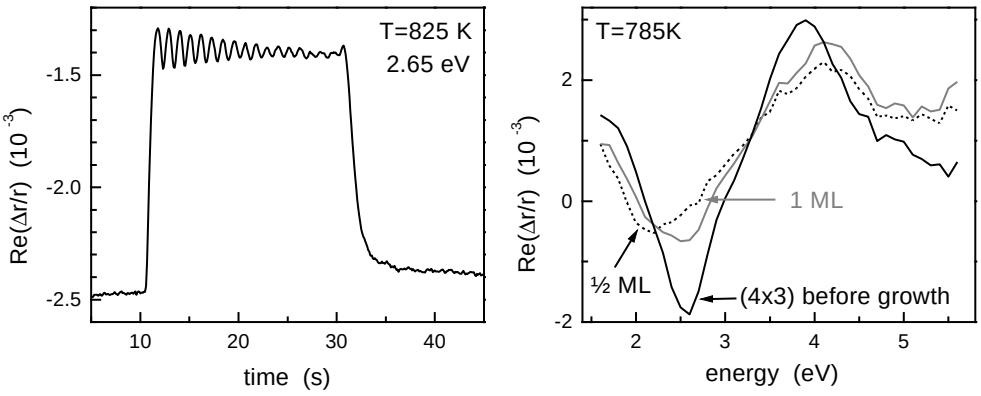

Figure 6.30: *RAS signal oscillations measured at 2.65 eV photon energy during growth using TMGa (left side) and spectral resolved (right side).*

RAS signal oscillations with monolayer periodicity during growth were first measured in MOVPE using TMGa [62], then with TEGa [33], but also in MBE [55]. In MBE RHEED intensity oscillations caused by the roughening and smoothing of the surface during 2D island nucleation growth mode has been a well known fact for many years [63, 64]. Additionally in MOVPE, GIXD intensity oscillations of the crystal truncation rod were found. Thus a similar 2D island nucleation growth with characteristic roughness oscillations [7, 33] is present in MOVPE too.

The observation of the RAS signal oscillations in MBE as well clearly proved two things. Firstly, adsorbates are not important with respect to their origin. Secondly, RAS signal oscillations are indeed related to 2D island nucleation growth. But the presence of 2D island nucleation growth mode was not sufficient, because at certain temperatures RHEED intensity oscillations (and therefore 2D island nucleation growth), but no RAS signal oscillations were observed [55]. Detailed investigations revealed that the RAS signal change during growth and hence the RAS signal oscillations strongly depend upon the reconstruction of the surface [55].

The straight forward interpretation of RAS signal oscillations as a result of an anisotropic changing roughness was finally proven wrong by calculations [10]. The calculated RAS

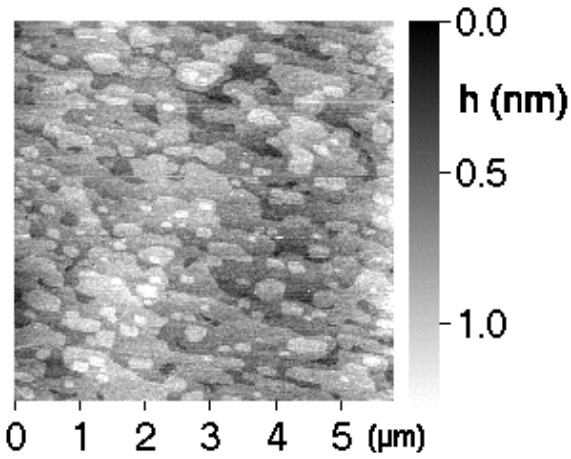

Figure 6.31: *AFM image of a surface after growth in 2D island nucleation growth mode.*

oscillation amplitude for one monolayer high anisotropic islands was too small for the observed RAS signal amplitudes. Finally in MOVPE the RAS spectra at the maximum and minimum of the RAS signal oscillation were measured during growth using TMGa (fig. 6.30) [65] and TEGa [33]. The resulting spectra were incompatible with spectra calculated assuming an anisotropic roughness [10]. Instead the measured spectra showed a dependence on the gallium precursor. Using TEGa the RAS spectra oscillate between phase I and phase II. Using TMGa however, the RAS spectra oscillate between phase II and phase III (see fig. 6.30; phases are described in the previous section 6.5).

In both cases after half a monolayer growth (i.e. many small islands) the RAS spectrum resembles more a phase II RAS spectrum, i.e. a gallium rich surface. GIXD measurements showed the surface to be covered with many small islands [33, 48]. Apparently the higher island density and subsequently the higher surface roughness causes a more gallium rich surface. Two things contribute to this mechanism. Firstly, there is enhanced arsenic desorption at the step-edges (discussed in sec. 6.2 and 6.3.2). Secondly, due to the tighter bonding at step-edges, gallium atoms are preferably incorporated there. Therefore close to the steps the surface has a more gallium rich reconstruction, like discussed in the previous section 6.5.

However after the completion of a monolayer only a few large islands remain, resulting in a small area of gallium rich reconstruction close to the step-edges and thus a large area of arsenic rich reconstruction. Hence the RAS signal oscillates between the RAS spectra of more gallium rich and more arsenic rich surfaces.

Obviously the change between more gallium rich areas and more arsenic rich areas depends on the growth regime. No oscillations are expected during step-flow growth, since the step density does not change. Furthermore, if there is no difference of the reconstruction at the step-edges and on the islands, no RAS signal oscillation are expected, even if the growth mode is 2D island nucleation. Therefore, at higher temperatures in phase I, when the pre-growth and during growth surfaces are nearly identical, no change of reconstruction at the step-edges and thus, no oscillations are expected. The temperature of the transition to phase I depends mostly on temperature and to a smaller degree also on precursor and carrier gas (see figs. 6.26 and 6.27). Hence, only during growth in the phase II regime the vanishing of the RAS signal oscillations indicates a “true” transition from 2D island nucleation growth mode to step-flow growth mode.

From measurements of the transition temperature to step-flow growth at several temperatures and fluxes on vicinal substrates (to have well-defined distances between steps) the constants of the diffusion equation (3.8) can be obtained, as discussed in section 3.1.1.

Transition temperatures on vicinal surfaces were first measured in MBE ([66, 67, 68, 69]) but also in MOVPE [7, 58, 59]. However, it is not clear at which proportion of diffusion length to terrace width the transition to step-flow mode takes place. The ratio depends on the value for the number of atoms that can reach a step during diffusion, which itself can be calculated using the BCF theory, explained in section 3.2.2. For the further analysis in this work the value of 2:1 for the ratio of diffusion length versus terrace width was assumed, i.e. 76 % of the diffusion atoms are incorporated at the step-edges.

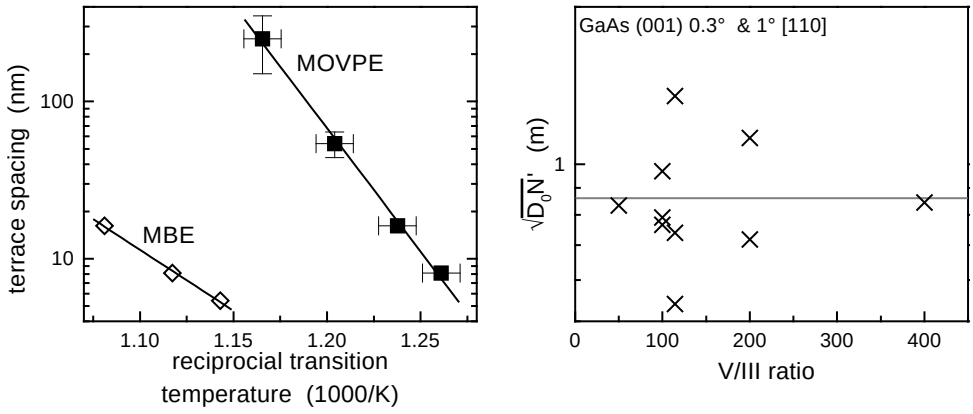

Figure 6.32: *Transition temperatures in MOVPE for TMGa=0.7 Pa for different sample misorientations (left side) (MBE data [67]) and calculated diffusion coefficients* $\sqrt{D_0 N_r}$ *using an activation energy of 2.8 eV (right side).*

As shown in figure 6.32, the transition temperatures are very different in MBE and MOVPE. This is probably due to the different reconstructions. In MOVPE the terraces are mostly covered with an arsenic double layer and therefore gallium incorporation is hindered. In MBE however, the whole surface is usually covered by (2x4) reconstructions, thus gallium is easily incorporated. But also the slope of the lines and therefore the activation energies are very different. Typical values for MBE growth are 1.3 eV to 1.8 eV ([66, 67, 70]. The only measurement in MOVPE so far reported a value of 2.7 eV [7], which agrees well with the value of about 2.8 eV found in this work.

Although the transition temperatures in MOVPE depend strongly on misorientation, temperature and partial pressures, the data for the diffusion coefficient in the right side of figure 6.32 do not show an increase to higher or lower values. Hence the activation energy for diffusion was correctly estimated.

6.6.2 Step-Bunching on Vicinal Surfaces

In section 3.3 the principal mechanism of step-bunching was described. Apart from a diffusion length longer than the terrace width, an anisotropic diffusion energy barrier at the step-edges (negative Schwoebel barrier) was needed. These conditions are both fulfilled on the (001) surface of GaAs. Figure 6.33 shows the step-bunch width (i.e. the separation of the bunches) for different temperatures and partial pressures after growth on 2° [1$\bar{1}$0] vicinal (001) GaAs substrates. The step-bunch width was obtained from several AFM images and the error bars mark the standard deviation.

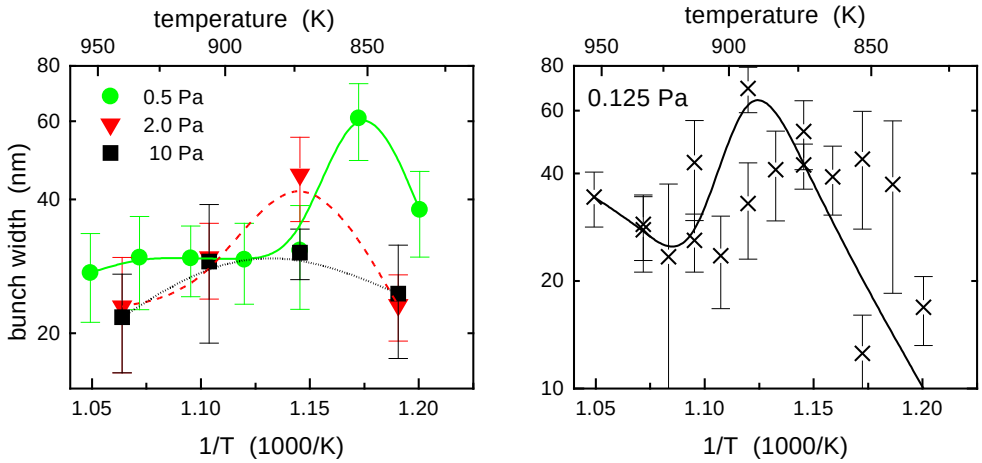

Figure 6.33: *Development of step-bunch width as a function of temperature and using different partial pressures (0.125 Pa measured with new gas inlet).*

For all TMGa partial pressures the step-bunch width first increases with temperature. This is simply due to an exponential increase of the diffusion length of gallium species on the surface in the nucleation limited diffusion regime (sec. 3.1.1). However, at higher temperatures the step-bunch width decreases again. This might be due to either a shorter diffusion length or a change of the Schwoebel barrier. Both values depend strongly on the surface reconstruction. Thus a quantitative analysis of the phase diagram presented in section 6.5 was tried. It was assumed the surface was either covered by (4x3) or (nx6). As pointed out in section 4 the RAS signal amplitudes can be directly correlated to the fraction of surface covered by each reconstruction, the RAS spectra measured during growth on 2°[1$\bar{1}$0] vicinal (001) GaAs surface were fitted by a linear combination of (4x3) and (nx6) RAS spectra.[2] To enhance contrast only the increase in (nx6) area compared to the area covered on the pre-growth surface is shown in figure 6.34.

The dark region (high increase of (nx6)) in figure 6.34 agrees very well with the phase boundary of the phase II measured on exactly oriented substrates (fig. 6.26). At higher temperatures the surface becomes more gallium rich (see fig. 6.11) and simultaneously the differences between pre-growth and during growth surfaces becomes small. Thus no increase in (nx6) area is seen any more.

The right hand side of figure 6.34 shows the development of (nx6) area increase for three selected TMGa partial pressures. The arrows mark the temperature of the widest step-bunch width from figure 6.33. Hence strong step-bunching seems to require two things: a high temperature and a high increase in (nx6) area during growth. Most likely, the termination of step-edges with gallium dimers causes an anisotropic diffusion rate across the step-edges

[2] Since it was not possible to prepare a (4x3) reconstruction at 900 K, a (4x3) RAS spectrum measured at 825 K was shifted to 0.2 eV lower energies, to simulate the energy shift for higher temperatures.

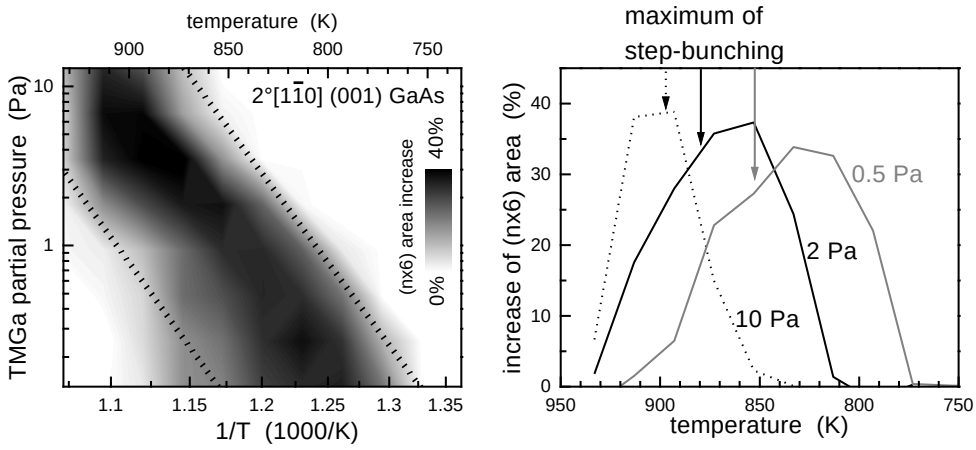

Figure 6.34: *Increase of (nx6) area during growth using H_2 10 kPa, AsH_3 100 Pa and TMGa on a vicinal 2°[1$\bar{1}$0] (001) GaAs surface as gray scale map (left side, dotted lines are phase boundaries from fig. 6.26) and for three selected partial pressure as lines (right side).*

(i.e. negative Schwoebel barrier). Without this, even if the diffusion length is long enough, no step-bunching would appear.

Therefore, the increase of the step-bunch width at increasing temperatures up to the maximum step-bunch width are certainly limited by the gallium diffusion length on the surface. For the analysis it was assumed that the diffusion length equals the step-bunch width. Using equation (3.8) the diffusion coefficients $\sqrt{D_0 N_r}$ were calculated and plotted in figure 6.35. For comparison the values obtained from measurements of the transition temperatures to step-flow growth from the previous section 6.6.1 have been included.

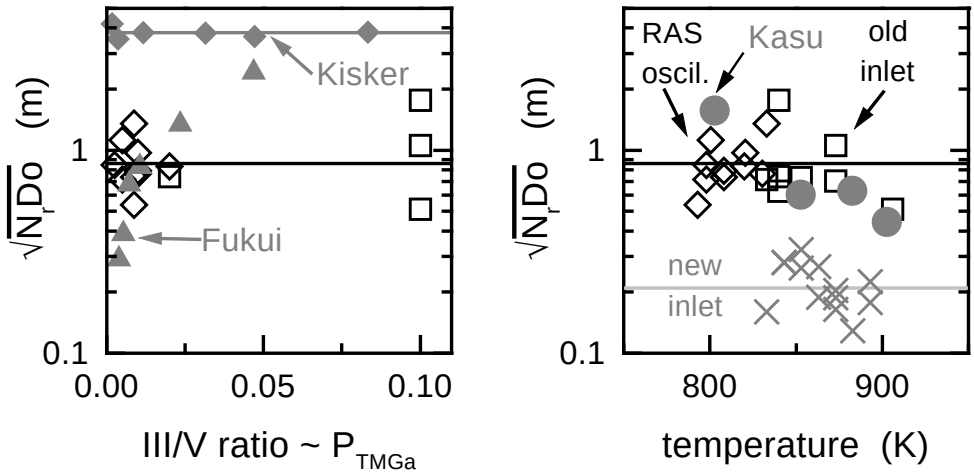

Figure 6.35: *Diffusion coefficients $\sqrt{D_0 N_r}$ calculated from several measurement using an activation energy of 2.8 eV (Kisker [7] varied TMGa+tBAs, Fukui [71] varied AsH_3+TEGa, Kasu [72] STM nucleus densities with STM after growth)*

The absolute values of the diffusion coefficient in figure 6.35 differ strongly between different references. Even in our system the alteration of the gas-inlet changed it by a factor of six. The scattering of data simply reflects the difference of the amount AsH_3 (or TMGa) going into the reactor versus the amount of arsenic (or gallium) which finally reaches the surface. The alteration of our “shower head” to provide a more homogeneous mixing of

AsH_3 and TMGa resulted in more arsenic rich surfaces, and thus a higher effective V/III ratio at the surface.

surface	$\sqrt{D_0 N_r}$ in m	E_{Diff} in eV	precursor	remarks
(113)	$(60 \pm 40)\,10^{-9}$	(0.38 ± 0.06)	TMGa+AsH_3	old inlet [73]
(001)	$\approx 10^{-5}$	1.3 ± 0.1	Ga+As_4	(2x4) in MBE [66]
(001)	$\approx 1 \cdot 10^{-4}$	1.58 ± 0.15	Ga+As_4	(2x4) in MBE [67]
(001)	$\approx 8 \cdot 10^{-7}$	1.74	Ga+As_4	(2x4) in MBE [69]
(001)	0.9 ± 0.3	≈ 2.8	TMGa+AsH_3	RAS oscil. & step-bunching
(001)	0.21 ± 0.07	≈ 2.8	TMGa+AsH_3	altered inlet, step-bunching
(001)	0.8 ± 0.5[1]	≈ 1.4	TEGa+AsH_3	nuclei densities by STM (calc. from fig. 3 in [72])
(001)	1.0 ± 0.8	—	TEGa+AsH_3	only AsH_3 varied, step-bunching [71]
(001)	3.8 ± 0.2[2]	≈ 2.7	TEGa+tBAs	GIXD oscil. [7]
(001)	—	≈ 2.5	TMGa+tBAs	diffuse GIXD [7]
(001)	—	1.35 ± 0.1	TIBGa+tBAs	roughness correlation [74]

[1] : calculated from the data using an activation energy of 2.8 eV.

[2] : calculated using an tBAs flux of 171.6 μmol/min.

Table 6.2: *Diffusion constants $\sqrt{D_0 N_r}$ and activation energies for diffusion E_{Diff}. If not marked otherwise these are MOVPE data.*

Nevertheless, all values obtained with the "old" reactor setup agree very well. Table 6.2 shows all available data on diffusion coefficient and activation energy of diffusion. All the MBE data have much smaller diffusion coefficients and activation energies. This is due to the more arsenic rich reconstruction in MOVPE, on which gallium is bound more tightly to the surface (higher activation energy), but offer many possible pathways for diffusion (higher diffusion coefficient $\sqrt{D_0 N_r}$).

A recent theoretical work concerning diffusion on c(4x4) reconstructed (001) surfaces calculated an activation energy of about 0.4 eV for diffusion [75], which is far less than the experimental value of 2.8 eV. Further studies are needed to check, if this is caused by neglecting the methyl groups or the hydrogen.

6.6.3 Other Diffusion Measurements

The density of islands, formed during 2D island nucleation growth, should be inversly proportional to the square of the diffusion length. By measuring the density of small islands the diffusion length can be calculated. The difficult part of such measurements is the transfer of the sample from the MOVPE reactor to the STM without changing the island density.

Measurements of the spacing of islands on quenched, capped and decapped MOVPE samples have been done using an Scanning Tunneling Microscopy (STM) [72]. The diffusion length calculated from the nucleus density after growth at various temperatures was proportional to $\propto \exp\left(\frac{1.36\,\mathrm{eV}}{2k_B T}\right)$, i.e. exaktly half of the value in this work.

However, the samples had to pass the many steps before an STM measurement was performed. First, the sample was first cooled with about 2 K/s to room temperature, then capped by an amorphous arsenic layer, and finally the cap was thermally desorbed in an ultrahigh vaccum chamber [72]. Therefore, small island may not be observed, because they were able to coalescence during the process (e.g. the cooling or the annealing step). Thus the measured island densities may be too low, depending on cooling and annealing times. However, using the diffusion length from the paper, and an activation energy of 2.7 eV, a diffusion constant of (0.8 ± 0.5) m is obtained, very close to our values.

Finally, a diffusion length can be also obtained from the correlation of roughness on randomly rough surfaces [74]. A activation energy of 1.35 eV was obtained. However, the morphology of the surfaces were much rougher than surfaces grown in our system at comparable conditions (see next section). This may be due to the use of the unusual gallium precursor triisobutylgallium (TIBGa). Furthermore, the question arises, if the so obtained diffusion lengths on rough surfaces are similar to the one on flat surfaces.

6.6.4 Summary of Gallium Species Diffusion

Diffusion lengths have been determined either by measuring transition temperatures from 2D island nucleation to step-flow growth mode on vicinal substrates, or by measuring the separation of step-bunches. The values of the activation energy of diffusion (2.8 eV) and the diffusion constant ($\approx$0.8 m) calculated from both measurements showed very good agreement with many measurement found in literature (see table 6.2). However, the diffusion constant was found to be very sensitive to the actual reactor set-up.

6.7 Carbon Incorporation

Carbon is widely used for GaAs p-type doping for several reasons. Firstly the carbon atoms in the GaAs bulk have a very low diffusion coefficient [76] due to the very tight gallium-carbon bond. Also the generated holes have a relatively high mobility [77]. Then, in contrast to zinc or beryllium (in MOVPE seldomly used) there is no carry over of dopants ("memory effect"), since the carbon either leaves the reactor as methane or solid immobile carbon is deposited. Finally carbon is non-toxic in contrast to beryllium, and carbon precursors are very cheap. And although carbon is a group IV element and can in principle do p- or n-type doping, during growth on the GaAs (001) surface carbon always ends up on an arsenic site, i.e. the layers are always p-type [78].

Using TEGa carbon incorporation during growth is not an issue, because of its low decomposition temperature and due to the decomposition mechanism via $\beta-$elimination (see sec. 5 for details) practically no carbon reaches the surface at growth temperatures above 600 K.

During growth using TMGa background carbon incorporation is always present, since TMGa decomposes only to mono-methyl-gallium in the vapor phase. Thus many methyl groups reach the surface. These methyl groups react with the hydrogen from AsH_3 [15] to form methane, which is very stable and simply desorbs. Therefore, the carbon incorporation can be very high, if there is not enough atomic hydrogen to desorb the methyl groups. This is either done intentionally by the use of low V/III ratios or unintentionally during growth at low temperatures, when only a small fraction of AsH_3 is decomposed. Therefore, using TMGa as gallium precursor, hole concentrations from below $10^{14}\,\mathrm{cm}^{-1}$ up to above $5 \cdot 10^{19}\,\mathrm{cm}^{-1}$ can be obtained just by changing temperature and V/III ratio.

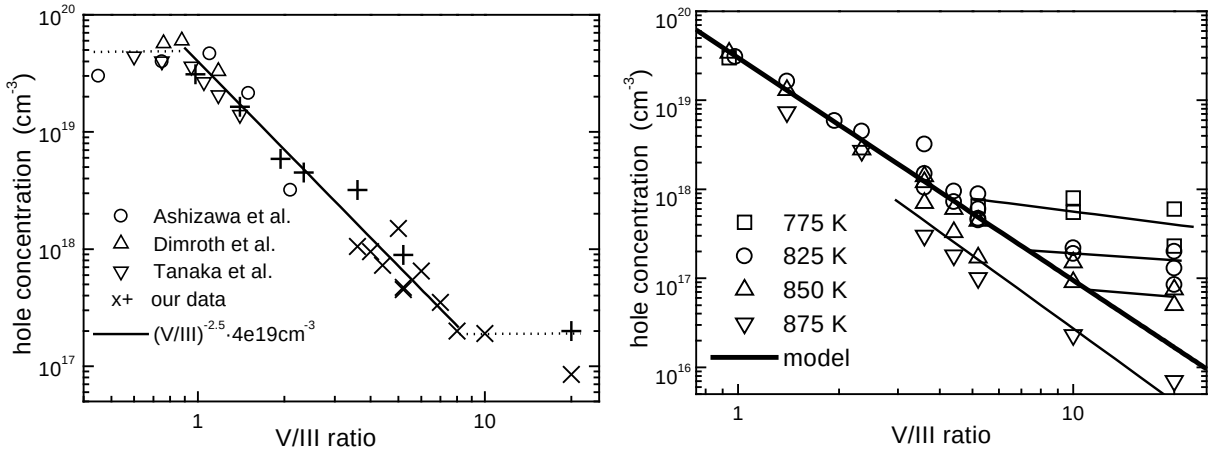

Figure 6.36: *Hole concentration versus V/III ratio for growth at 823 K compared to results in literature (Ashizawa [79] 823 K, Tanaka [80] 765 K, Dimroth [81] 803 K) (left) and our data for different temperatures (right).*

Figure 6.36 shows the measured hole concentration as a function of the V/III ratio. Despite the different MOVPE reactors and different growth temperatures all the data agree very well. The hole concentrations depends mainly on the V/III ratio during growth. Three different regimes can be distinguished:

1. At V/III ratios below one the hole concentration saturates close to $5 \cdot 10^{19} cm^{-1}$.

2. In the intermediate range the hole concentration shows a power law dependence on the V/III ratio:

$$p(r) = \frac{p(1)}{r^k}, \tag{6.1}$$

T	$p(1)$ in cm^{-3}	k	V/III ratios
893 K	$1.5 \cdot 10^{19}$	2.1	2.4 ... 130 [82]
873 K	$1.4 \cdot 10^{19}$	2.7	1.5 ... 20
850 K	$2.5 \cdot 10^{19}$	2.5	1 ... 10
823 K	$2.8 \cdot 10^{19}$	2.3	1 ... 10
773 K	$1.4 \cdot 10^{18}$	2.2	1 & 5

Table 6.3: *Parameters for calculation of hole concentration dependence from V/III ratio, determined by fits to the experimental data. The error of k is about ± 0.3.*

where r is the V/III ratio, $p(r)$ the hole concentration and k an empirically determined exponent. Table 6.3 gives the parameters for equation (6.1) derived from data in figure 6.36.

Both parameters, $p(1)$ and the exponent k, seem to be constant. p(V/III=1) is always close to $3 \ldots 5 \cdot 10^{19}$ cm^{-3} and the exponent k is always near 2.5, although there is no obvious explanation for this behavior.

3. At high V/III ratios the hole concentration saturates, and the saturation level is temperature dependent.

It is remarkable that the change in the carbon incorporation behavior is also reflected by the topography of the layers. Figure 6.37 shows AFM and optical microscope images of layers grown at different V/III ratios. At low V/III ratios of about one some holes can be observed on the surfaces, but overall the surfaces are relatively smooth (fig. 6.39). At V/III ratios above 1.5, small hillocks appear and the surfaces become rougher (clearly visible for V/III=1.94 and 3.6 in fig. 6.39). Finally, at high V/III ratios the surfaces are smooth again, apart from some quite large hillocks.

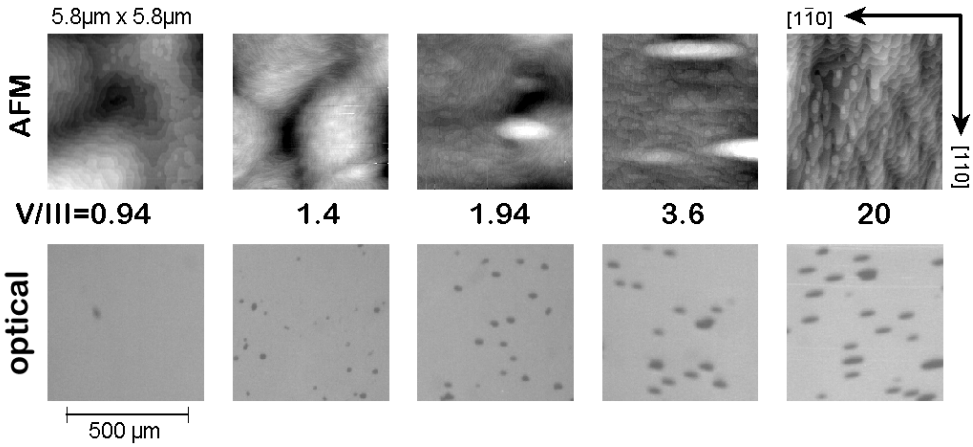

Figure 6.37: *AFM and optical microscope images of 5 μm thick layers after growth at 823 K and a TMGa partial pressure of 5 Pa.*

The size of hillocks increases with increasing V/III ratio (fig. 6.39). These hillocks might be due to the relatively high TMGa partial pressure (5 Pa) and thus the large growth rate (about 4.8 μm/h) used to obtain low V/III ratios.

All these processes can be related to the change of the reconstruction on the surface. Figure 6.38 shows the evolution of the RAS spectra during growth with decreasing V/III ratio. Using high V/III ratios the RAS spectrum is similar to that of a (1x2)-CH_3 reconstruction: the growth is in the phase III regime (phases are discussed in sec. 6.5), typical for

kinetic limited growth. Indeed, the growth rate in figure 6.38 (upper right) depends only on temperature for V/III ratio$\geq$2, as expected for kinetic limited growth.

The methyl groups are only weakly bond to the phase III surface: when the growth is stopped, the surface returns to its initial state within seconds. Therefore, the doping level depends on how fast the carbon is incorporated, i.e. hole concentration should depend strongly on the growth rate.

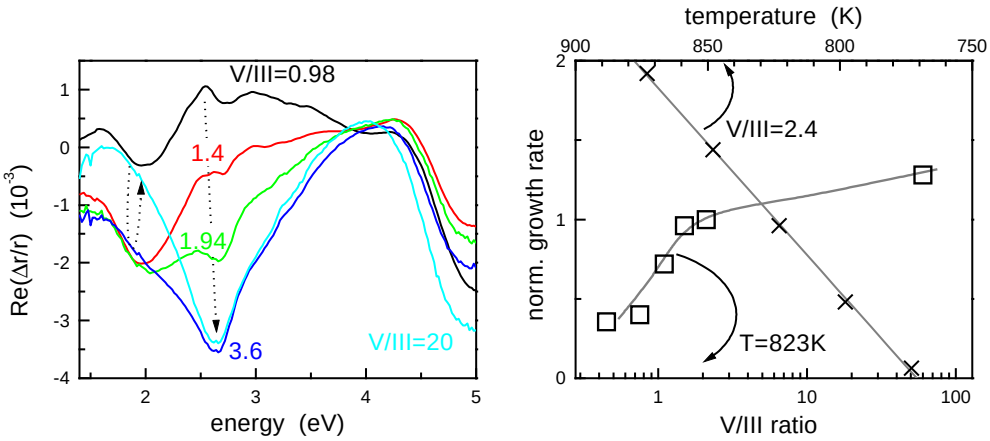

Figure 6.38: *RAS spectra measured during growth at different V/III ratios at 823 K (left) and growth rate as a function of the V/III ratio at 823 K [79] and as a function of temperature at a V/III ratio=2.4 (right side).*

The saturation of the carbon incorporation at low V/III ratios is correlated with a drop of the growth rate at V/III ratios below 1.5 (fig. 6.38), i.e. the growth becomes AsH_3 limited in contrast to the usual case of TMGa limited growth. The RAS spectra measured during growth at low V/III ratios corresponds to that of a (1x4)-CH_2 reconstruction. This reconstruction is characteristic for growth in phase IV in the phase diagram in figure 6.26.

As stated in [47] and section 6.4.2 the (1x4)-CH_2 reconstruction is very stable and inert against further TMGa adsorption. Therefore, the growth rate depends no longer on the TMGa partial pressure but on the CH_2 desorption rate. The methylene desorption rate itself is influenced by temperature and by the amount of hydrogen or AsH_x that reaches the surface.

In this growth regime, the carbon incorporation becomes independent from the V/III ratio, because the entire surface is (1x4)-CH_2 reconstructed and thus the carbon coverage is fixed at a certain value. A further decrease of the V/III ratio decreases only the growth rate, as less hydrogen is delivered to the surface because less AsH_3 reaches the surface. Less hydrogen means that less CH_2 reacts to CH_3 and finally to methane and desorbs. Thus less surface sites are available where AsH_3 (and TMGa) can attach.

As mentioned earlier, the surfaces after growth at very low V/III ratios are surprisingly smooth (see fig. 6.37 and 6.39). This is probably due to a reversed step-flow growth mode. Now the desorption of the methylene is the limiting factor, because the attachment of AsH_3 is also sterically hindered by the methylene layer as it is for the TMGa. Because desorption of methylene is likely higher at the step-edges due to a less tight bonding (as observed for arsenic in sections 6.2 and 6.3.2). Thus, AsH_3 can only attach at the step-edges, resulting in AsH_3 limited step-flow growth.

In the intermediate range at V/III ratios of 2 to 4 the surface becomes quite rough. A lot of 2D islands are present on these surfaces (like in fig. 6.31), but also larger 3D islands and some holes (fig. 6.37). This is probably connected to a transition of the reconstruction of the

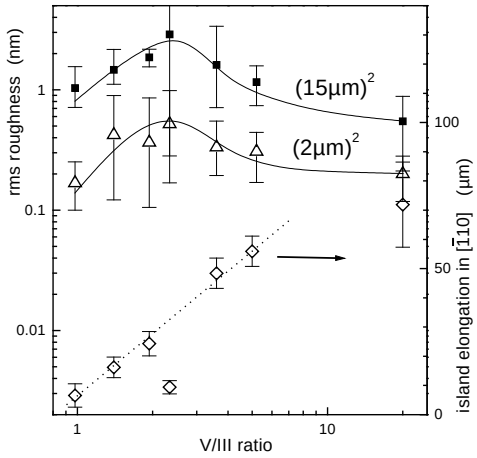

Figure 6.39: *RMS roughness and hillock size of the V/III ratio for 5 μm thick layers grown at 823 K.*

growing surface. While at low V/III ratios the entire surface is (1x4)-CH_2 covered, at inermediate ratios domains of (1x4)-CH_2 and (1x2)-CH_3 coexist. The (1x2)-CH_3 domains act as nucleation sites, since precursor adsorption is suppressed on the (1x4)-CH_2 domains. If a small area of (1x2)-CH_3 is formed, the TMGa and AsH_3 will attach there. Thus the (1x2)-CH_3 domains are growing faster than the (1x4)-CH_2 covered domains. Since the growth is 2D island nucleation mode, the layers are growing out of sync, i.e. at some places the growth on top of a layer is beginning, while at many other places the previous layer is not even finished.

At V/III ratios above 5 there is enough hydrogen present to change the whole surface into (1x2)-CH_3. All methyl groups of the TMGa can react with hydrogen and desorb. Since the whole surface is covered by a single reconstruction, the surface is smooth again.

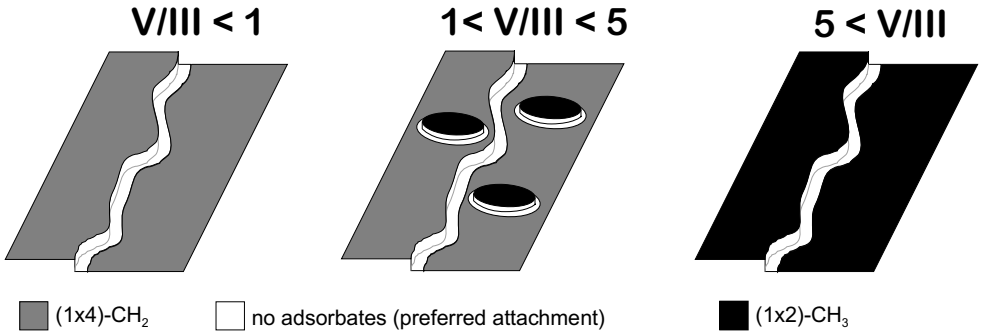

Figure 6.40: *The surfaces during growth with the three different V/III ratios. At low V/III ratios only the step-edges are not covered by adsorbates, while at intermediate V/III ratios many additional sites for attachment are formed.*

Summarizing, three different regimes of carbon incorporation can be observed: a saturation at $p = 3 \cdot 10^{19}$ cm^{-3} at low V/III ratios, a decrease following a power law at intermediate V/III ratios and finally, at V/III ratio above 10, again a constant carbon incorporation. This can be explained by the presence of different reconstructions during growth, as shown systematically in figure 6.40. At low V/III ratios the entire surface is (1x4)-CH_2 covered, and carbon incorporation as well as growth rate is methylene desorption limited. At high V/III ratios the whole surface is covered by (1x2)-CH_3. Since the methyl groups are more weakly bound than the methylene groups the carbon incorporation on the (1x2)-CH_3 covered surface

is lower. In the intemiate range both reconstructions are present, the carbon incorporation changes with the different sizes of the domains.

7 (115) Surface

The (115) surface shows no tendency towards faceting, neither during MBE nor MOVPE growth. No facets were found by AFM or LEED. The AFM image of this surface in figure 7.1 shows many small islands with monoatomic steps. Hence this surface grows in 2D island nucleation growth mode at the buffer temperature of 925 K. The spacing of the structures and thus the diffusion length indicated by the AFM image is in the range of 20 nm, much shorter than on other GaAs surfaces. Investigations by Scanning Electron Microscopy (SEM) micrographs of 180 nm thick MBE grown buffer layers showed some roughness and no RHEED intensity oscillations were reported [83].

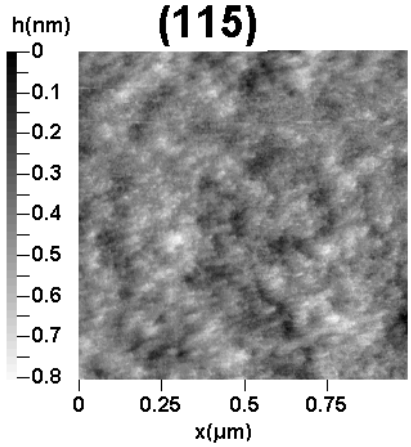

Figure 7.1: *Typical AFM image after 500 nm buffer growth in MOVPE at 925 K.*

In literature only a few studies have been done concerning the (115) surface. The growth rate on the (115) surface in atmospheric pressure MOVPE at 993 K was a little higher than that of the (001) surface, resulting in an expansion of the (001) surface during growth on patterned substrates [84]. The surface symmetry measured by LEED during and after MBE growth was a primitive (1x1) symmetry [83].

7.1 Well-ordered Surfaces

7.1.1 p(1x1) Reconstruction

The RAS spectra measured at arsenic rich conditions are shown in figure 7.2 together with a LEED image.

The amplitude of the RAS spectrum measured in MBE in fig. 7.2 is smaller, probably due to an insufficient supply of arsenic to prepare this surface. The LEED image corresponds to a primitive p(1x1) symmetry, the rhomboedric primitive unit mesh can be clearly seen.

A p(1x1) reconstruction cannot contain arsenic dimers simply for geometrical reasons. Therefore, a termination of the surface by arsenic ad-atoms is proposed for this surface. A similar structure is discussed in section 8.1.2 for the arsenic rich (113) surface.

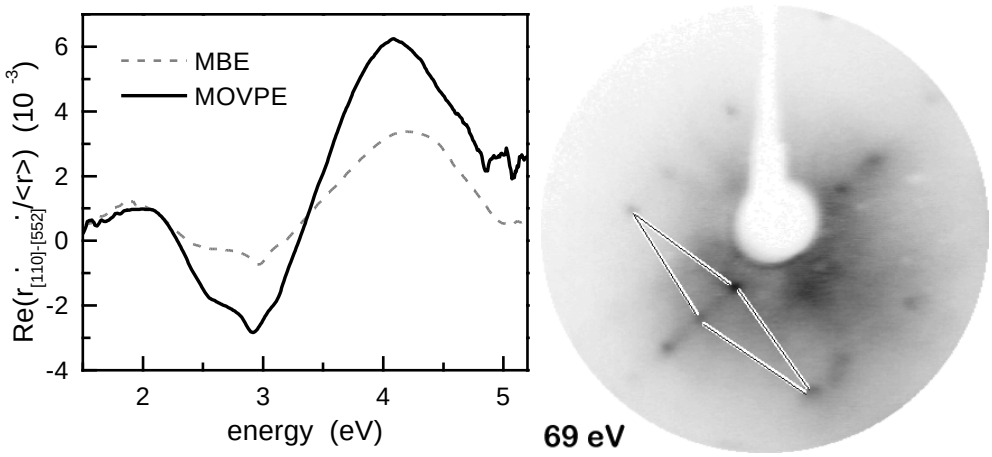

Figure 7.2: *RAS spectrum in MOVPE and MBE and LEED image after MOVPE growth and transfer of the arsenic rich p(1x1) reconstruction.*

7.1.2 p(2x2) Reconstruction

Under less arsenic rich conditions and temperatures above 800 K a primitive p(2x2) reconstruction was found to be the typical reconstruction in MOVPE and MBE. A LEED image of this reconstruction was published in [85].

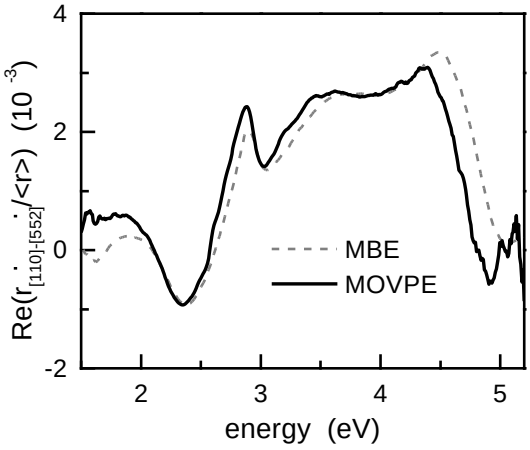

Figure 7.3: *RAS spectrum of the p(2x2) reconstruction.*

The RAS spectrum in figure 7.3 is quite similar to that of $\beta 2$(2x4) reconstruction on a (001) surface. Therefore the p(2x2) is probably also made of arsenic dimers on top of a bulk layer. The p(2x2) symmetry would allow for such a model of this reconstruction, consisting of rows of arsenic dimers.

7.2 Arsenic Desorption

The arsenic desorption behavior is a second order process, since the RAS signal during desorption is inversely proportional to the time: $RAS \propto t^{-1}$ (fig. 7.4). The activation energy for arsenic desorption was found to be (2.09±0.07) eV.

Since no studies of arsenic desorption from high-index surface have been made in UHV using a mass-spectrometer no information about the desorbing species is available.

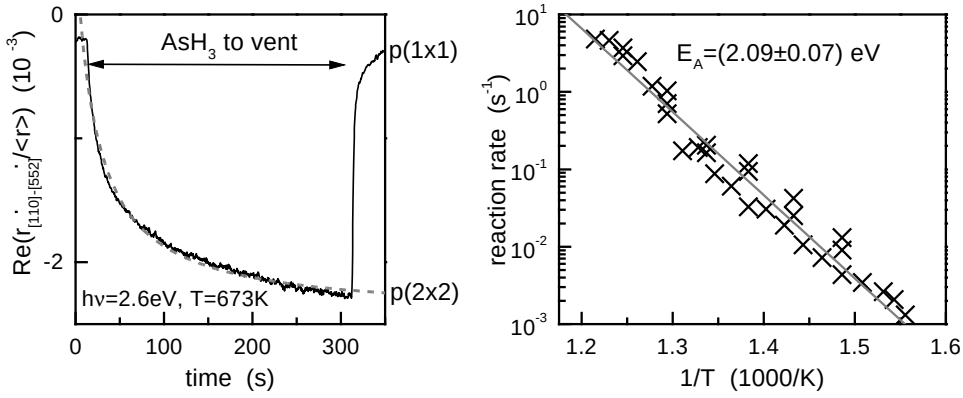

Figure 7.4: *RAS transient during arsenic desorption (left) and Arrhenius plot of the desorption rates (right).*

8 (113) Surface

After a report of Nötzel et al. in 1991 on the self-organized formation of AlAs quantum wires during MBE growth [86] on the (113) surface, this surface has been the target of several investigations [87, 88, 89, 90, 91]. At the beginning the RHEED patterns of the GaAs (113) surface during MBE growth were interpreted as a 3.2 nm wide corrugation [86]. However, STM studies showed that instead of a corrugation, a reconstruction with an (8x1) symmetry was formed [87]. The proposed structural model [87] was confirmed by further studies with photoemission spectroscopy (PES) [89]. This (8x1) reconstruction was found to be stable over a wide range of growth conditions in MBE, and total energy DFT-LDA showed that the (8x1) reconstruction of the GaAs (113) surface is an energetically very favorable structure (fig. 8.1 [91]).

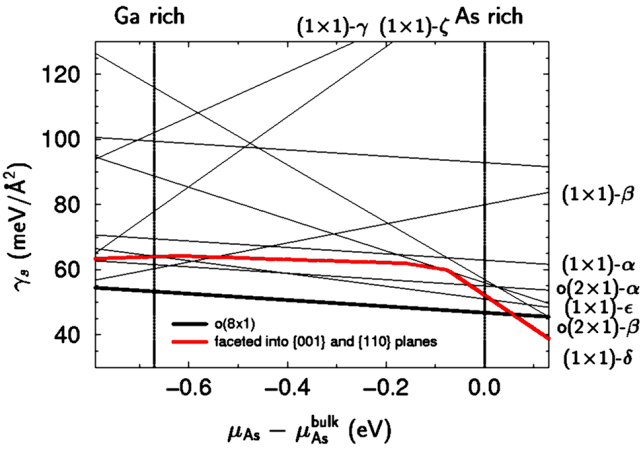

Figure 8.1: *Calculated total energy of several reconstructions of the GaAs (113) surface [91].*

The existence of another reconstruction, and therefore the possibility of reliably changing the amount of arsenic and gallium on the surface, is required for the observation of ALE growth as in [57]. Also STM images of decapped MBE grown surfaces [88] showed twofold, threefold, and fivefold symmetries in the [110] direction, which cannot be explained by an (8x1) reconstruction.

An MOVPE study of the homo-epitaxial growth of GaAs (113) reported a periodic corrugation, depending on temperature and layer thickness [92]. A similar roughness was also observed in the STM images of MBE grown samples [87, 88], although the small sizes of the scan areas did not allow for a quantitative comparison. The corrugation always consists of 1.5 to 2 nm high valleys, which run very straight in the [33$\bar{2}$] direction.

8.1 Well-ordered Surfaces

8.1.1 (8x1) Reconstruction

Figure 8.2 shows the RAS spectrum and the ball and stick model of the (8x1) reconstruction. The structure of this reconstruction has been confirmed by many different measurements, like STM [87], LEED and PES [89], and also by DFT-LDA calculation [91]. This amazingly complex structure fulfills the electron counting rule, and is the most complex reconstruction in the entire GaAs system.

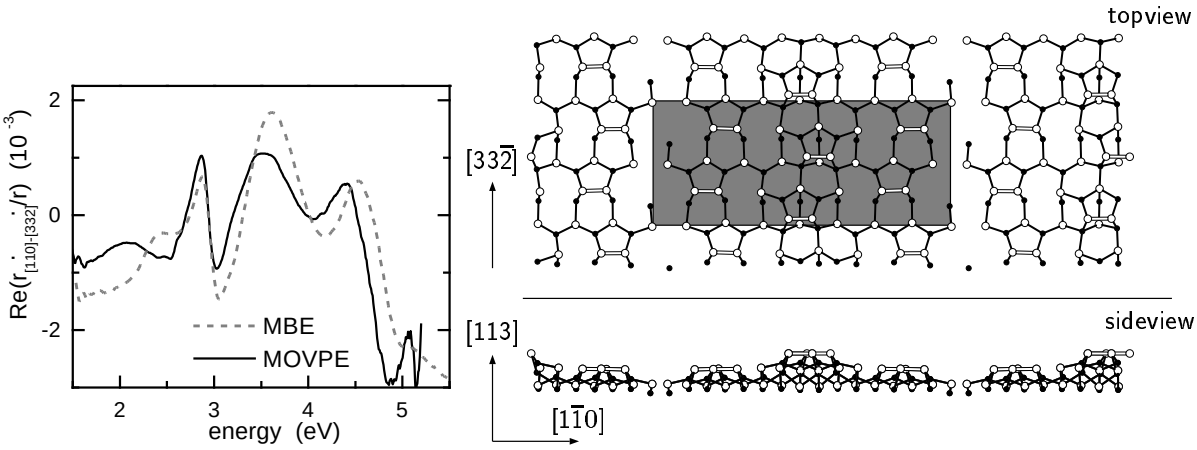

Figure 8.2: *RAS spectra of the (8x1) reconstruction measured in MBE and MOVPE at room temperature and structural model from DFT-LDA calculations [3].*

The (8x1) reconstruction consists of arsenic dimers on top of gallium atoms, threefold coordinated arsenic atoms with filled dangling bonds and threefold coordinated gallium atoms with empty dangling bonds. The atoms themselves are arranged in three different monolayers, thus there is a slight corrugation of two monolayers along [1$\bar{1}$0]. The atoms within one unit mesh can be rearranged in such an order that the reconstruction contains only two steps up or down and still fulfills the electron counting rule. As a result the surface is somewhat instable and spontaneously forms a corrugation along [1$\bar{1}$0], which will be discussed further in section 8.4.

8.1.2 p(1x1) Reconstruction

According to DFT-LDA calculations the (8x1) reconstruction is the only stable surface on the (113) surface [91] (see fig. 8.1). However, it is possible to perform ALE growth (i.e. growth by alternating switching between TMGa and AsH_3) [57]. Hence there have to be at least one less arsenic rich and one arsenic rich reconstructions. The growth rate per cycle saturated at about 0.4 ML. Thus this is the difference in arsenic coverage of the two reconstructions.

Indeed, at temperatures below 770 K in MOVPE another typical RAS spectra was measured, like the one shown in figure 8.3. Clearly, this RAS spectrum is very different compared to the one of the (8x1) reconstruction (fig. 8.2). This new reconstruction corresponds to arsenic rich conditions, because after heating in UHV or MOVPE without arsenic stabilization the surface reconstruction transforms into (8x1).

A similar RAS spectrum was found after MBE buffer growth and cooling down to room temperature with the As_4 shutter open (dotted lines in fig. 8.3). However the transition was not complete, as the total RAS amplitudes were smaller and the LEED image showed some traces of (8x1) symmetry. Probably the flux of the As_4 cell was too low to achieve a full surface transition.

The LEED image of a surface prepared by MOVPE growth at 925 K and subsequent cooling down with AsH_3 flowing till about 550 K is shown in figure 8.3 middle: Only reflection spots corresponding to p(1x1) bulk symmetry are visible, i.e. the most primitive unit mesh.

STM images measured on surfaces prepared by decapping (which might yield more arsenic rich surfaces) showed a twofold, threefold, and fivefold symmetry in the $[1\bar{1}0]$ direction [88].

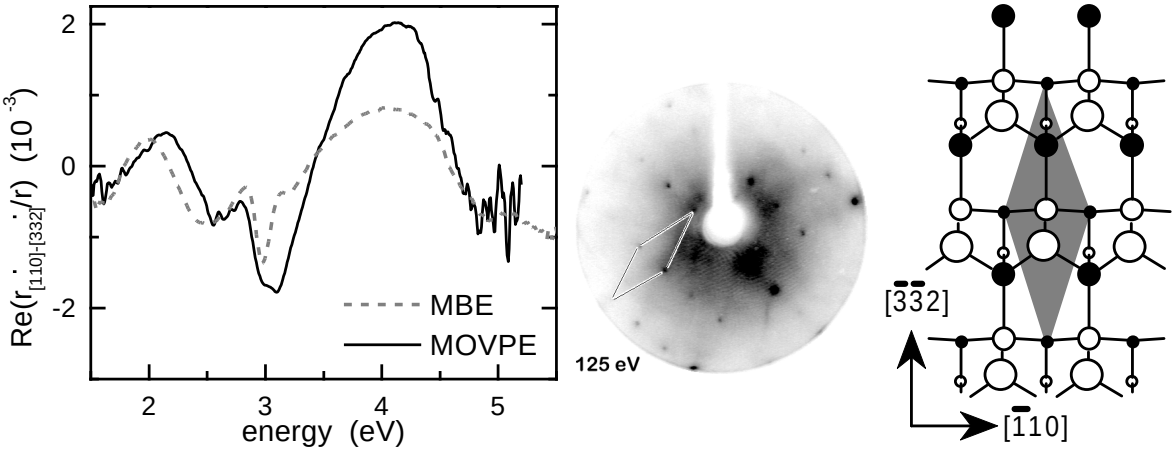

Figure 8.3: *RAS spectra of the arsenic rich p(1x1) reconstruction measured in MBE and MOVPE at room temperature (left), LEED image at 125 V after MOVPE to UHV transfer (middle) and proposed structure for this reconstruction (right).*

Since nobody has succeeded in the preparation of a well-ordered arsenic rich surface other than the (8x1) reconstruction in UHV, one can only speculate about the structure of the p(1x1) arsenic rich reconstruction. Even more, there is no way in which a reconstruction with p(1x1) symmetry could fulfill the electron counting rule. Thus, a well-ordered arsenic rich reconstruction is energetically very unfavorable.

The structure proposed in figure 8.3 also does not fulfill this rule, but it minimizes the number of dangling bonds. It consists of arsenic ad-atoms on top of a bulk layer. It features a difference of arsenic coverage of about 0.4 ML to the (8x1) reconstruction as suggested by ALE [57]. This structure was included into the DFT-LDA calculations as $\alpha-$(1x1) in figure 8.2, but it was not a lowest energy structure and therefore unstable. Slightly more stable was the $\delta-$(1x1) structure, with the gallium atoms in the first layer substituted by arsenic ad-atoms. However, such structure would be too arsenic rich for the ALE result.

8.2 Arsenic Desorption

Below 775 K the (113) surface in MOVPE is mainly p(1x1) reconstructed. If the AsH_3 is switched off below this temperature, arsenic desorbs and the surface changes into an (8x1) reconstruction. Figure 8.4 shows a typical RAS transient during a desorption experiment. The development of the RAS signal is clearly inversely proportional to time, i.e. the desorption process is of second order. A second order arsenic desorption process was also found on the (115) surface (sec. 7.2). Possibly the second order time dependence is caused by a transition between the same kind of reconstructions from an ad-atom structure to arsenic dimer terminated surface.

The temperature dependence of the effective reaction rates $\tilde{k}$ in figure 8.4 corresponds to an activation energy for arsenic desorption of (1.50 ± 0.02) eV. This energy is much lower than the 2.09 eV on the (115) and the 2.5 eV on the (001) surface. Hence the arsenic is less tightly bound, possible due to some internal stress because the dimers are tilted 25° with respect to the surface.

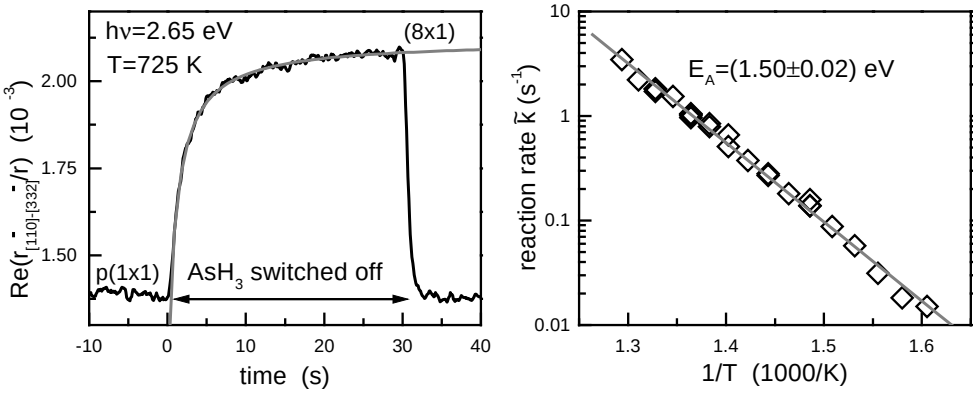

Figure 8.4: *RAS Transient at 2.4 eV photon energy and 725 K together with fit (dotted line) during arsenic desorption and Arrhenius plot for arsenic desorption from the p(1x1) GaAs (113) surface.*

8.3 Surfaces During Growth

During growth three different typical RAS spectra have been found (fig. 8.5). As described in section 6.5 they were compared to each other and then assigned to a certain phase.

The spectra characteristic for phase I and II are very similar to the ones of the static (8x1) reconstruction at the respective temperatures. The main difference is a lower general level in the UV range of the phase I RAS spectra, probably due to a roughness or a larger corrugation (see next section).

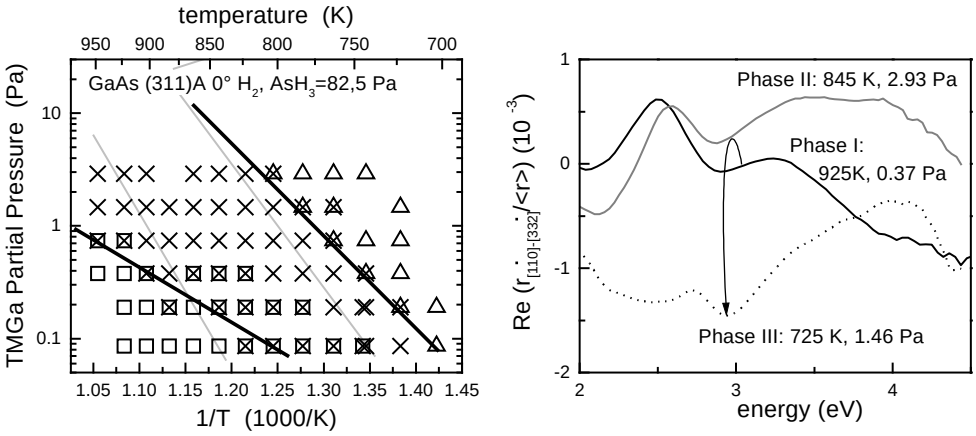

Figure 8.5: *Phase diagram for the growth on (113) GaAs surfaces using TMGa and hydrogen carrier gas. Gray lines indicate the phase boundaries on (001) surfaces taken from figure 6.26. Right hand side shows the three characteristic RAS spectra observed during growth.*

The RAS spectra typical for phase III resemble the one of the arsenic rich reconstruction, which is comparable to the behavior of the (001) surface: On the (001) surface the adsorbate covered phase III RAS spectra were similar to the ones of the static arsenic rich reconstruction (sec. 6.5). Therefore, phase III on the (113) surface is likely an adsorbate covered reconstruction, possibly consisting of gallium ad-atoms with attached methyl groups on top of a bulk-like layer, like the arsenic rich p(1x1) reconstruction.

The phase boundary between phase I and phase II has a different slope on the (113) compared to the (001) surface. However, this boundary is not abrupt and not only depends on

the precursor but also on the surface gallium and arsenic diffusion and sticking coefficients, which may vary between (001) and (113) surfaces.

The phase boundary between phase II and phase III is shifted slightly to lower temperature compared to the respective phase boundary on the (001) surface. This might be due to a higher sticking coefficient of TMGa or AsH_3, or the methyl groups are bound less tightly.

Summarizing, the phase boundaries which separate the different growth regimes show only a small variation between (001) and (113), emphasizing the fact that they depend strongly on the chemical kinetics of the precursors. Therefore, phase III on (113) as on (001) surface corresponds likely to an adsorbate covered surface.

8.4 Surface Diffusion

A valley structure develops on the (113) surface during annealing and increases further during buffer growth [92, 93]. Figure 8.6 shows a typical AFM image and the size increase during buffer growth. The valleys run along [33$\bar{2}$] direction for some 100 nm until a step. Such valleys appear spontaneously during growth only if the surface is (8x1) reconstructed. On the p(1x1) reconstruction only an increasing large-scale roughness develops during growth.

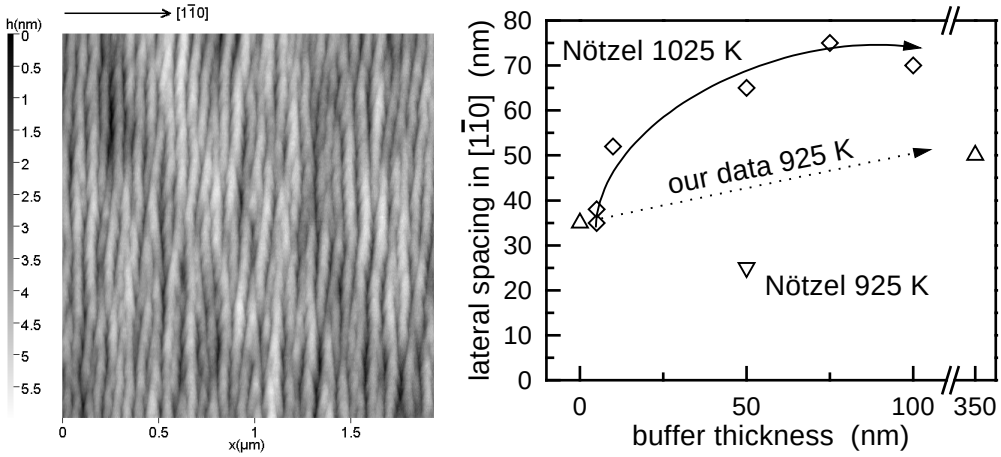

Figure 8.6: *Typical valley structure of the GaAs (113) surface after buffer growth at 925 K (left) and the development of the valley spacing during buffer growth (Nötzel [92]) (right).*

The origin of this structure is not yet clear. Fact is that steps along [1$\bar{1}$0] on an (8x1) reconstructed (113) surface have a very low energy, since these steps can be incorporated into the reconstruction without violating the electron counting rule. However, a somewhat similar structure was observed on Pt (110) surfaces [94]. In that case the structure was explained by intrinsic surface stress and its size limitation by kinetic effects.

Whether this explanation holds true or not, the spacing between the valley is very likely limited by surface diffusion, otherwise the temperature dependence of the valley spacing shown in figure 8.7 can be hardly explained, and the spacing would not increase during buffer growth as measured (fig. 8.6).

From the ascent of the valley spacing with increasing temperature (lines in figure 8.7) the activation energies for diffusion along [1$\bar{1}$0] in table 8.1 were calculated. The mean value is about 0.4 eV, which is much less than the value of 2.8 eV for diffusion on (001) surface (sec. 6.6.1 and 6.6.2).

Using equation (3.7) and an activation energy of 0.38 eV the values for the diffusion coefficients $\sqrt{D_0 N_r}$ can be calculated. The right side of figure 8.7 shows the results. The

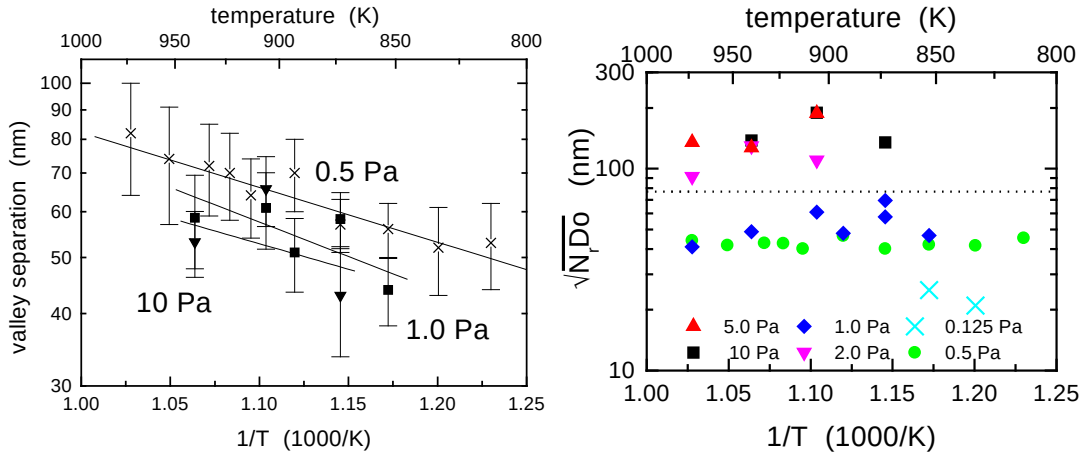

Figure 8.7: *Temperature and partial dependence of the valley separation for different partial pressures after one hour buffer growth (left) and calculated diffusion coefficients from these data (right).*

surface	P_{TMGa} in Pa	E_{Diff} in eV
(113)	0.5	0.38 ± 0.06
(113)	1.0	0.48 ± 0.28
(113)	10.0	0.4 ± 0.6
(001)	var.	2.7

Table 8.1: *Activation energies for diffusion E_{Diff} along [1$\bar{1}$0] direction.*

points show no tilt for higher or lower temperatures, thus the activation energy for diffusion is correctly chosen. However, the values for different partial pressures shows a systematical deviation, the smaller the partial pressure, the lower the diffusion coefficient.

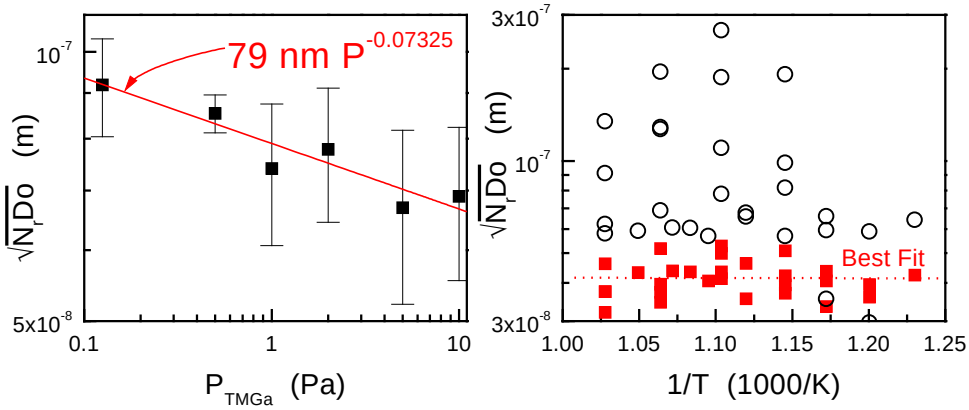

Figure 8.8: *Partial pressure dependence of the mean value of the diffusion coefficients $\sqrt{D_0 N_r}$ (left) and the diffusion coefficients $\sqrt{D_0 N_r}$ using the fitted pressure dependency (right) calculated with $P^{-0.5}$ (hollow) and $P^{-0.07325}$ (filled).*

The mean values for the diffusion coefficients $\sqrt{D_0 N_r}$ for different partial pressures from figure 8.7 are plotted in the left side of figure 8.8. The partial pressure dependence is very obvious: instead of $P_{TMGa}^{-\frac{1}{2}} \propto \sqrt{D_0 N_r}$ it is more like $P_{TMGa}^{-0.07325 \approx -\frac{3}{41}} \propto \sqrt{D_0 N_r}$. Either the valley spacing is not entirely diffusion limited, or the nucleation probability behaves strangely. The diffusion coefficients are changing accordingly (right side of fig. 8.8), but the

mean value changes only from about 60 nm to 42 nm. However, for comparison the same pressure dependency ($P_{TMGa}^{-\frac{1}{2}} \propto \sqrt{D_0 N_r}$) as on the (001) surface was used.

Comparing diffusion coefficients of the (113) surface $\sqrt{D_0 N_{r(113)}} = (60 \pm 40)10^{-9}$ m, and the one of the (001) surface $\sqrt{D_0 N_{r(001)}} = (0.9 \pm 0.3)$ m, the coefficient for the (113) surface is seven magnitudes smaller. Since the activation energy is also much smaller (0.4 eV for the (113) instead of 2.7 eV for (001), tab. 8.1), the diffusion lengths are in the same scale on both surfaces (50 to 100 nm).

9 (110) Surface

The (110) surface is called a non-polar surface, because simply due to mathematical reasons the (110) and the $(\overline{1}10)$=(11$\overline{0}$)=(110) surfaces are identical. It has an equal number of arsenic and gallium atoms in its outer layer.

The $\{110\}$ planes are the only cleavage planes of GaAs, and a clean (110) surface can be prepared very easily by cleaving. Due to this simple preparation the (110) surface is often used to try out new measurement methods: e.g. the first RAS measurements were made on this surface [95].

The (110) surface prepared by cleaving does not reconstruct but relax: the arsenic atoms at the surface relax outwards after taking $\frac{3}{4}$ electron from the gallium atoms. The resulting surface unit mesh is very small, consisting of only two atoms, which makes it relatively easy to calculate surface properties of this surface.

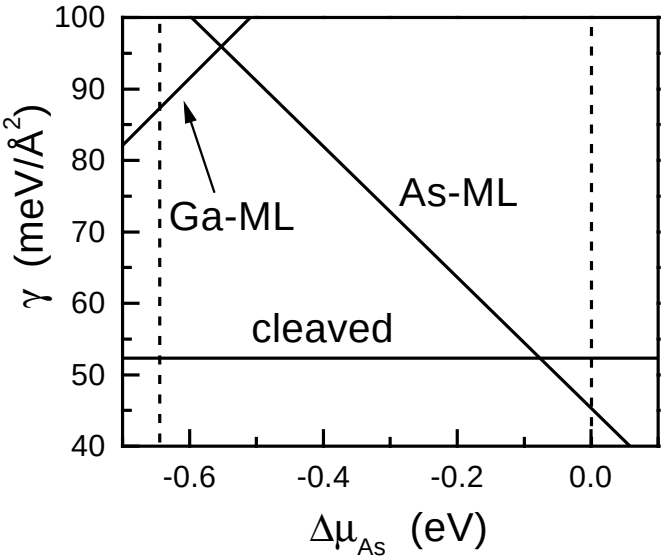

Figure 9.1: *DFT-LDA-Total energy calculation for the GaAs (110) surface [39]*

Therefore, the exact positions of the atoms, bond lengths, interaction with light, surface phonons, as well as the change due to adsorbates throughout the periodic table of elements, and many more aspects are known to a great detail. Epitaxy on this surface however, was not of great interest, since early studies discouraged the use of the (110) surface due to very small growth rates [96, 5]. These small growth rates result in very high, but anisotropic lateral growth rates. These highly anisotropic lateral growth rates [97] practically prevent selective area growth, which is needed for many devices. Finally, the surfaces for epitaxy are not prepared by cleavage but by wet chemical etching prior to epitaxy, which is harder to do on the (110) surface.

The interest on epitaxy on the (110) came back in the mid-90s. Two topics, the “cleaved edge overgrowth” of a (001) quantum well to produce nearly ideal quantum wires, and also the fundamental interest in the growth on high-index (11n) surfaces, were the driving forces. It was found that the (110) surface has several peculiarities: step-bunching (see sec. 3.3) [98, 99, 100], a two-monolayer step regime, a single monolayer step regime and finally simple step-flow growth [101]. All this with (1x1) symmetry, i.e. a very simple and small surface unit mesh.

9.1 Well-ordered Surfaces

Although the (110) surface shows only (1x1) symmetry, two different RAS spectra have been found. These RAS spectra are related to two different reconstructions, which have been predicted by total energy DFT calculations [39] (fig. 9.1).

9.1.1 (1x1) Bulk Truncated Structure

This reconstruction is prepared easily by cleaving in UHV. The arsenic atom relaxes outward, the gallium atom inward due to a charge transfer to the arsenic atom. This was also the first surface which was measured by RAS [95]. Also the RAS spectrum has been first calculated on this surface [102, 103].

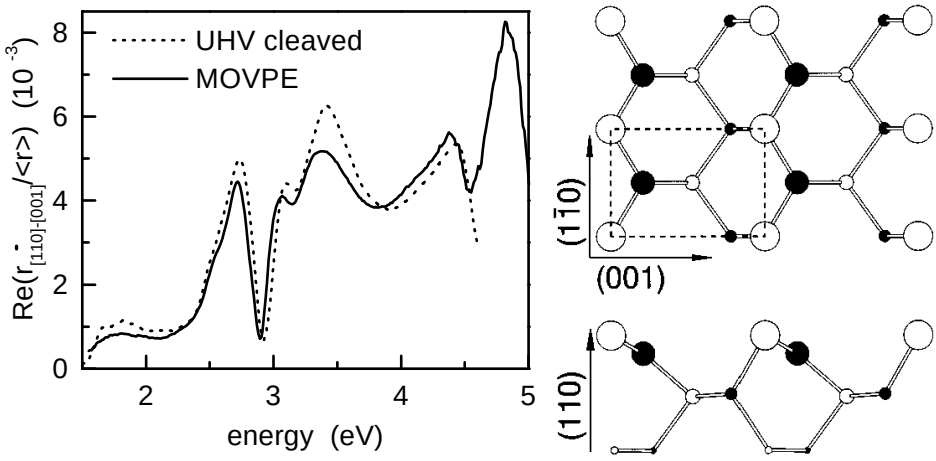

Figure 9.2: *RAS spectra at room temperature in MOVPE and UHV [104] and ball and stick model of the GaAs (110) bulk truncated surface.*

In MOVPE this surface is found at higher temperatures, typically above 900 K.

9.1.2 (1x1) Arsenic Terminated Structure

Total energy calculations proposed a second structure with (1x1) symmetry for arsenic rich conditions [39, 105]. This surface is entirely covered with an arsenic monolayer. A somewhat similar chemical structure is the antimony (Sb) monolayer on the GaAs (110) surface [104], since Sb is also a group V element. Such an arrangement is also called Epitaxial Continued Monolayer Structure (ECLS).

Together with arsenic rich conditions in MOVPE another type of RAS spectrum was observed, shown in figure 9.3. This spectrum is supposed to be the arsenic terminated structure, but unfortunately there have been no other studies using RAS to verify this. However, the RAS spectrum can be compared to the one of an antimony terminated reconstruction in figure 9.3. The RAS spectra are somewhat similar, if one takes the smaller bandgap of Sb alloys, and thus a shift to lower energies of surface related features of the Sb-RAS spectrum, into account. Essentially the RAS structures at about 2 eV and at 4.3 eV are changing sign accordingly (fig. 9.3) compared to the bulk truncated surface (fig. 9.2.

Very recently DFT calculations of the arsenic rich reconstruction has been performed to obtain the RAS spectrum [106]. The agreement is good, if the calculated spectrum is shifted a little bit to higher energies (fig. 9.3).

A very early work using LEED I/V curves suggested, that an arsenic rich surface prepared by MBE is covered by an arsenic adlayer, and the relaxation vanishs [107]. Even more,

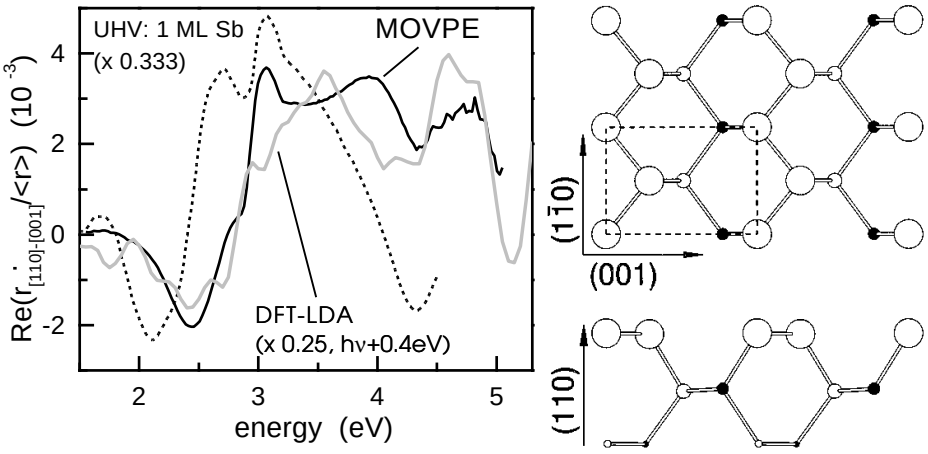

Figure 9.3: *RAS spectra (see text) and ball and stick model of the GaAs (110) arsenic terminated structure.*

it was not possible to adsorb more than one monolayer of arsenic, which strongly support the ECLS model. Further evidence of the existence of an arsenic adlayer structure comes from PES (PhotoElectron Spectroscopy) measurements on decapped MBE grown samples. An (1x1) symmetry and no shifts of the gallium core-level together with two shifted arsenic core-levels was reported [108], which agrees well with the structure in figure 9.3.

9.2 Arsenic Desorption

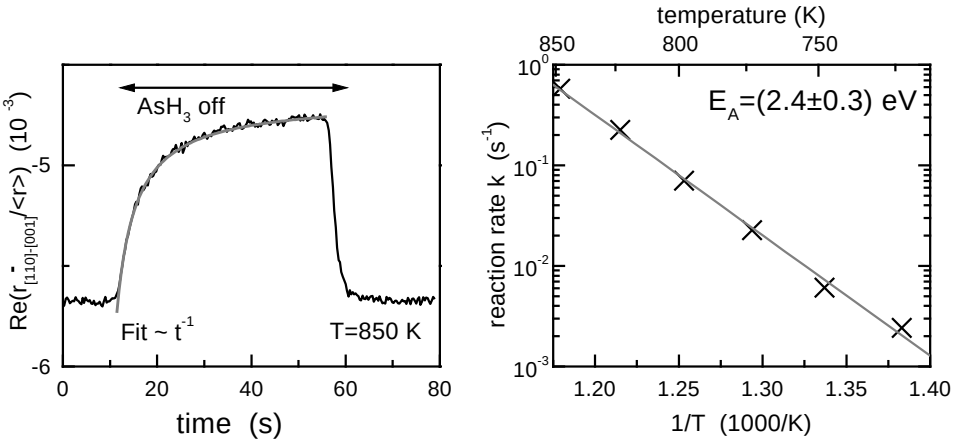

Figure 9.4: *RAS transient at $h\nu$=3.5 eV and an Arrhenius plot for arsenic desorption.*

The arsenic desorption from the arsenic terminated to the bulk truncated surface is a second order reaction. The activation energy determined from the Arrhenius plot is (2.4 ± 0.3) eV.

9.3 Growth

Many interesting phenomena have been reported for the GaAs (110) surface, which can be at least partly understood by the existence of two different reconstructions. For example doping with silicon yields n-type layer for growth temperatures below 800 K but p-type above [109]. Since the incorporation of silicon atoms on a gallium site (which is necessary

for n-type doping) is higher on an arsenic terminated surface, the transition temperature between n- and p-type doping marks simply the transition between the two reconstructions.

The existence of an arsenic monolayer on the surface at arsenic rich conditions can also explain the large step-bunching observed below at certain temperature on vicinal (110) substrates [98, 99, 100], because gallium is only easily incorporated on the bulk terminated surface. Hence large areas of the arsenic monolayer terminated surface at arsenic rich conditions lead to a large gallium diffusion length and consequently to very high lateral growth rates. Since the separation of steps is limited by the gallium diffusion length, the step-bunching should disappear at higher temperatures or less arsenic rich conditions. But the disappearance of step-bunching may be also due to a change of the termination of the steps and hence a change in the energy barrier necessary for step-bunching.

However, the observed double layer growth mode [101] cannot be explained straight forward by the existence of the arsenic terminated reconstruction.

10 $(\overline{113})$ Surface

In the mid-nineties the $(\overline{113})$ surface got a lot of attention due to the growth of self-organized "quantum discs" by growing InAlGaAs in MOVPE on GaAs $(\overline{113})$ [110, 111].

The topography of the plain $(\overline{113})$ GaAs surface, however, is very much dependent on growth conditions, e.g. during MBE growth it tends to form facets [85, 90, 91]. However after MOVPE growth the surfaces are atomically flat with monoatomic steps, which was measured by AFM (fig 10.1 and [112]). The LEED patterns of MOVPE grown samples showed no facet spots, confirming the AFM results.

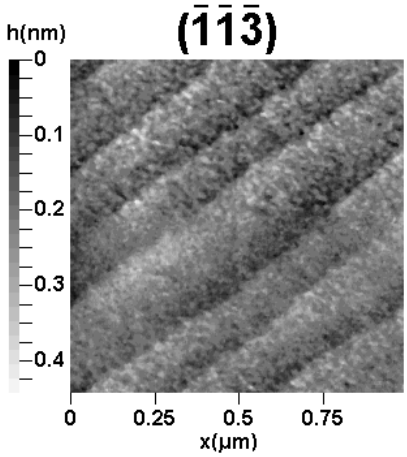

Figure 10.1: *Typical AFM image after 500 nm buffer growth in MOVPE, showing smooth terraces and monoatomic steps.*

After prolonged annealing without arsenic in MOVPE or UHV above 800 K the $(\overline{113})$ surface develops facets. Therefore, at gallium rich conditions there is very likely no stable surface. The facets could be very easily detected with LEED. The RAS amplitude of the faceted surface becomes very small, so the facets must be more or less isotropic (probably $\{111\}$ planes).

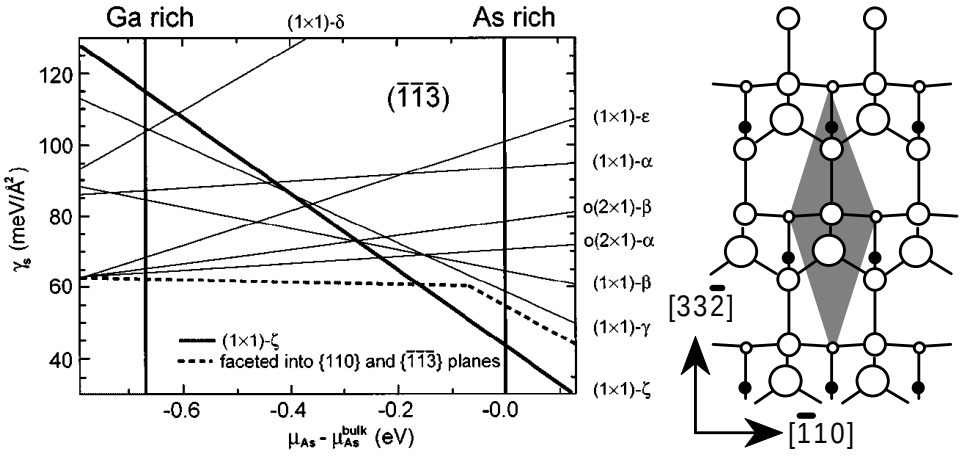

Figure 10.2: *Calculated total energy of several reconstructions of the GaAs $(\overline{113})$ surface [91] (left) and a model of the stable $(1 \times 1) - \zeta$ reconstruction (right).*

Total energy DFT-LDA-calculations found a stable surface (fig. 10.2) for arsenic rich conditions. At more gallium rich conditions faceting was predicted, as it was also found

experimentally [90]. The proposed structure of the stable p(1x1) reconstruction is shown in figure 10.2. This reconstruction is somewhat similar to the arsenic rich structure on the (113) surface (sec. 8.1.2).

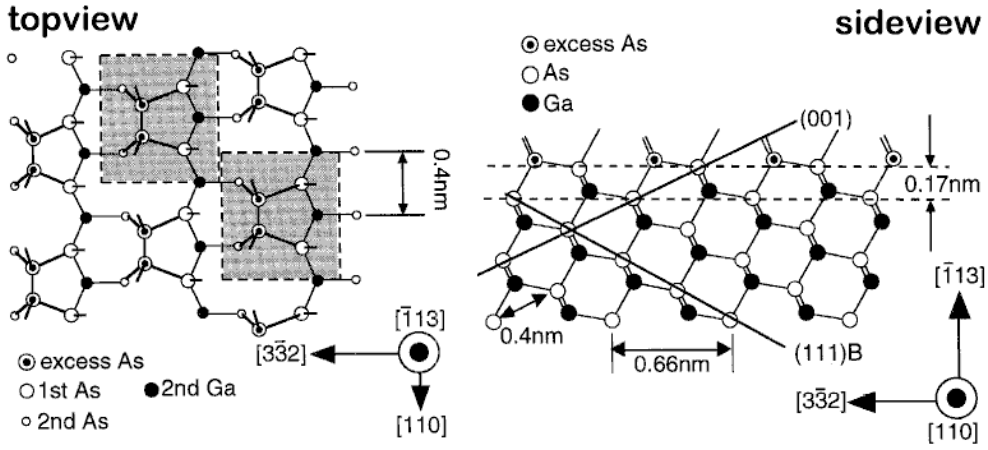

Figure 10.3: *Proposed model for the p(2x1) reconstruction on GaAs ($\overline{113}$) from STM and RHEED measurements [112].*

An AFM, RHEED and STM study of ($\overline{113}$) surfaces of in-situ capped MOVPE grown layers reported very smooth layers in AFM, comparable to the AFM image in figure 10.1. STM in UHV on the decapped samples revealed many holes and some disorder on the terraces. The RHEED pattern measured on the surfaces had a p(2x1) symmetry (fig. 10.3). The proposed model of an arsenic dimer along [$\bar{1}$10] in a unit mesh does not fulfill the electron counting rule. Unfortunately a p(2x1) structure was not included in the DFT-LDA calculations shown in figure 10.2.

The observation of large growth rates during ALE (up to 2.5 ML/cycle), which did not saturate, [57] indicates a faceting during ALE growth. Thus no information about the arsenic coverage can be extracted from these data.

10.1 Well-ordered Surfaces

10.1.1 p(1x2) Reconstruction

At very arsenic rich conditions a p(1x2) reconstruction was found. The RAS spectrum and the LEED image are shown in figure 10.4. Clearly the unit mesh indicated in the LEED images corresponds to a p(1x2) symmetry. This unit mesh is very small but long, as the right side of figure 10.4 indicates. This makes it very hard to come up with a reasonable structural model for this surface. A possible structure is the presence of an arsenic dimer on top of an arsenic layer (as the c(4x4) reconstruction on the (001) surface) or a missing ad-atom structure on an arsenic terminated layer (as on the $\{111\}$ surfaces).

The presence of this reconstruction turned out to be a good test of our MOVPE systems, since it reproducibly appears only in the MOVPE system, which was optimized for yielding very arsenic rich conditions. However, at temperatures above 750 K this reconstruction was not stable any more.

10.1.2 p(2x1) Reconstruction

The RAS spectrum normally found in MOVPE is shown in figure 10.5 together with a LEED-image. A p(2x1) symmetry is compatible to the measured LEED images. There are

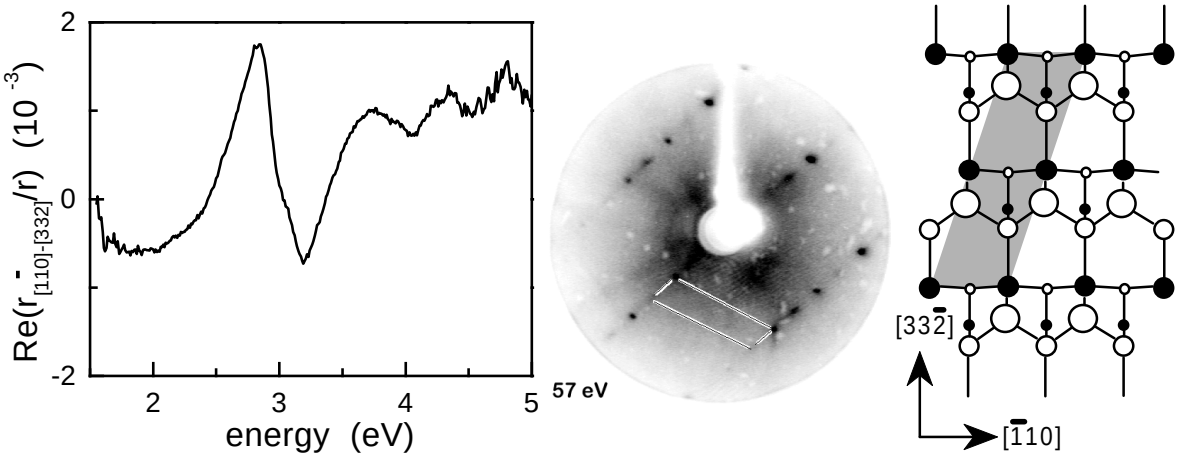

Figure 10.4: *RAS spectrum at room temperature and LEED image of the arsenic rich p(1x2) reconstruction after MOVPE growth and in-situ UHV transfer and the p(1x2) unit mesh on the ($\overline{113}$) surface.*

bands at semi-order positions between the primitive (1x1) spots, but the primitive (1x1) spots are relatively strong, indicating disorder on the surface. Therefore, this reconstruction is identical to the proposed p(2x1) structure proposed in [112] (see fig. 10.3), which reported a p(2x1) symmetry together with a lot of disorder.

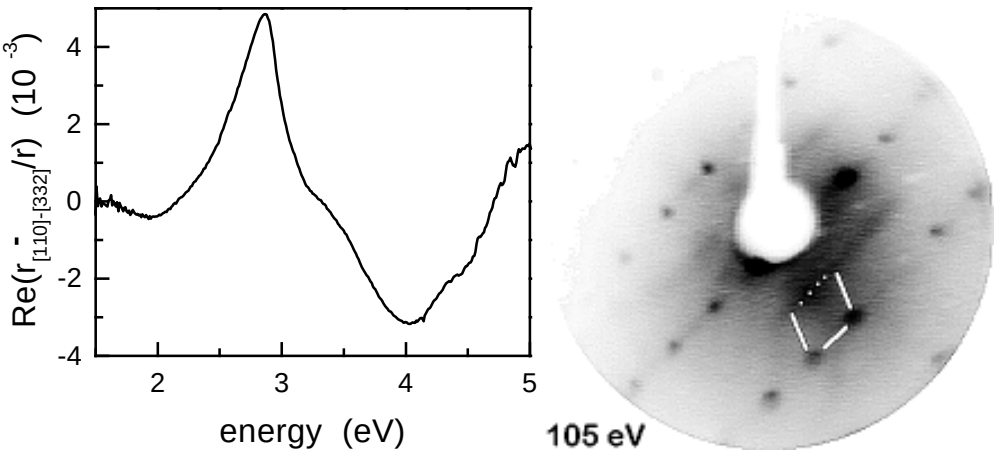

Figure 10.5: *RAS spectrum at room temperature and LEED image of the less arsenic rich p(2x1) reconstruction after MOVPE growth and in-situ UHV transfer.*

Recently an (8x1) structure – like the one on the (113) surface discussed in section 8.1.1, but made out of gallium dimers – has been proposed and is now under closer investigation [113]. However, the p(2x1) surface is usually obtained at an AsH_3 partial pressure of 100 Pa and more; the presence of gallium dimers at such conditions seems very unlikely.

10.2 Arsenic Desorption

Figure 10.6 shows a typical RAS transient for an arsenic desorption experiment. After a slow start (due to the poor layout of the gas-switching manifold of the MOVPE system used) the arsenic desorption is exponential with time. The desorption is a first order reaction like many desorption processes on the (001) surface.

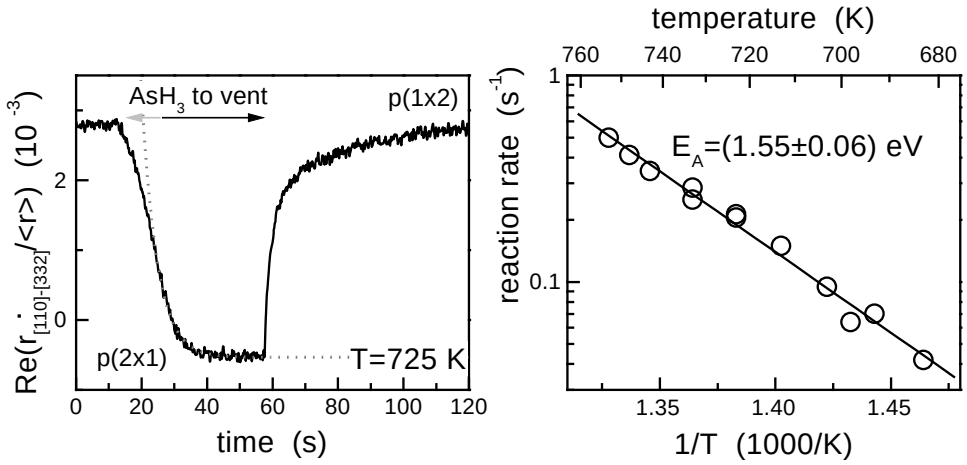

Figure 10.6: *RAS transient at 3.75 eV together with fit (dotted line) during arsenic desorption and Arrhenius plot for arsenic desorption from (113) surface.*

The activation energy for arsenic desorption is 1.55 eV, which is very close to the value of 1.5 eV on the (113) surface (sec. 8.2), although the orders of reaction differ (2nd order on (113), 1st on (113)).

10.3 Surfaces During Growth

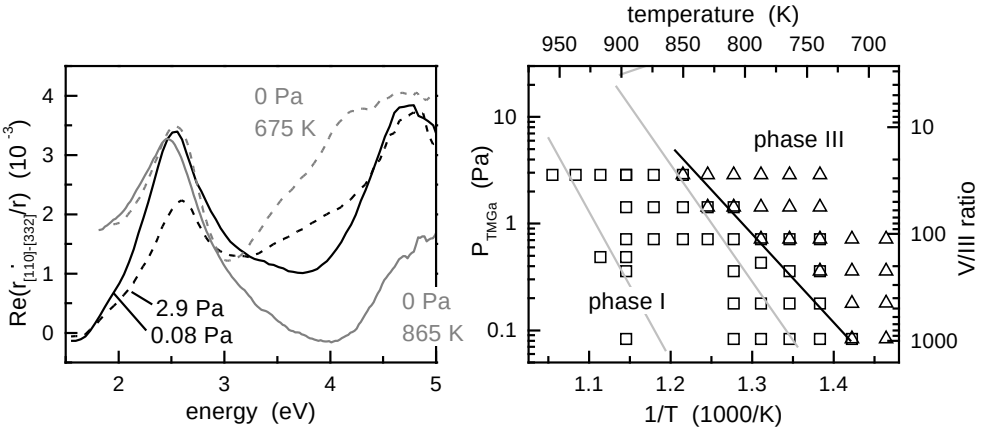

Figure 10.7: *RAS spectra observed during growth at 783 K (black) and static spectra (gray) and a phase diagram from GaAs (113) (right side). The gray lines in the phase diagram are the phase boundaries on GaAs (001). The AsH_3 partial pressure was always 100 Pa.*

Figure 10.7 (left) shows the two typical RAS spectra obtained during growth, together with spectra of the static surfaces (in gray). The characteristic spectrum (black dotted) at phase III conditions (i.e. low temperatures/high TMGa fluxes) is similar to that of the p(1x2) reconstructions at 675 K (gray dotted). This is similar to the behavior of the (001) and (113) surfaces, where the phase III RAS spectra resemble the static arsenic rich RAS spectra.

However, as mentioned earlier the growth rate during ALE growth does not saturate [57], contrary to the case of GaAs (113). Either the phase III reconstruction on the (113) surface is not completely covered by adsorbates, or simply facets appear during ALE growth.

The phase boundary between phase I and phase III in figure 10.7 is identical to the one between phase II and III on the (113) surface (fig. 8.5) (black line). However, both (113) and ($\overline{113}$) surfaces show the same small deviation of the transition to phase III compared to the (001) surface. That is, because the binding of surface species depends mostly on the geometry (strain, bond length etc.) of the $\{113\}$ and $\{\overline{113}\}$ surfaces than on different reconstructions of these surfaces.

11 $(\overline{1}\overline{1}5)$ Surface

The AFM image of a buffer layer grown on the $(\overline{1}\overline{1}5)$ surface in figure 11.1 is quite noisy. However, the noise apparently comes from many small structures on the surface itself and large terraces can also be observed. Compared with the (115) surface (sec. 7 fig. 7.1), the $(\overline{1}\overline{1}5)$ surface is smoother. A similar finding was reported by Scanning Electron Microscopy (SEM) micrographs of 180 nm thick MBE grown buffer layers which measured a smooth $(\overline{1}\overline{1}5)$ surface, but a slightly rougher the (115) surface [83].

At gallium rich conditions in MBE and MOVPE the $(\overline{1}\overline{1}5)$ surface shows a tendency towards faceting, although it was not as strong as on the $(\overline{1}\overline{1}3)$ surface.

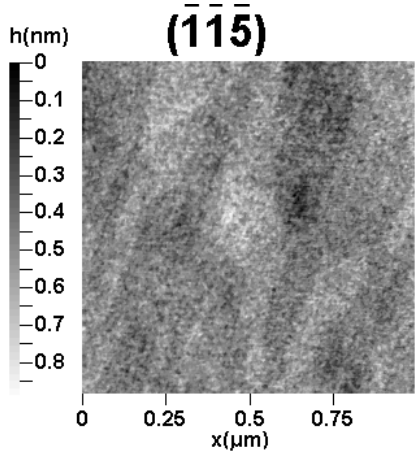

Figure 11.1: *Typical AFM-image after 500 nm buffer growth in MOVPE.*

The surface symmetry measured by LEED during and after MBE growth was a primitive (1x1) symmetry [83].

11.1 Well-ordered Surfaces

11.1.1 Arsenic Rich Reconstruction

This is the surface usually found in MOVPE at low temperatures. Figure 11.2 shows the RAS spectrum of this surface. Unfortunately, no MOVPE to UHV-transfer succeeded, thus no LEED images and no symmetry information are available.

11.1.2 Less Arsenic Rich Reconstruction

Another RAS spectrum was measured at higher temperature. However, this surface was not measured at room temperature. In any case the RAS spectrum in figure 11.3 is clearly very different from the one of the arsenic rich reconstruction in figure 11.2. Therefore this is really a new reconstruction.

A reconstruction with p(2x2) symmetry was measured on a sample prepared at less arsenic rich conditions by MBE [85]. Such symmetry would allow for dimers. However, the RAS spectrum of this surface does not resemble any of the RAS spectra measured in MOVPE.

Neither arsenic desorption experiments nor a phase diagram of the $(\overline{1}\overline{1}5)$ surface was measured.

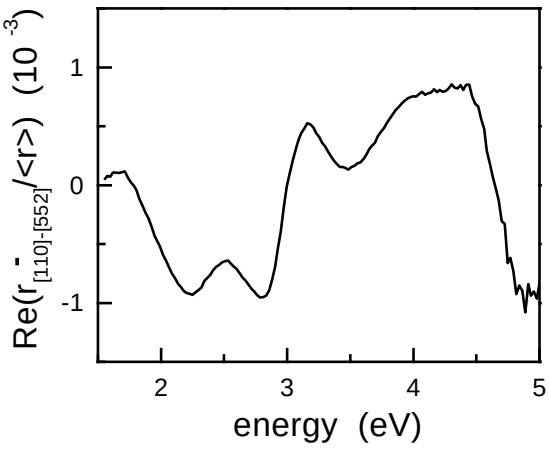

Figure 11.2: *RAS spectrum of the arsenic rich reconstruction at room temperature in MOVPE.*

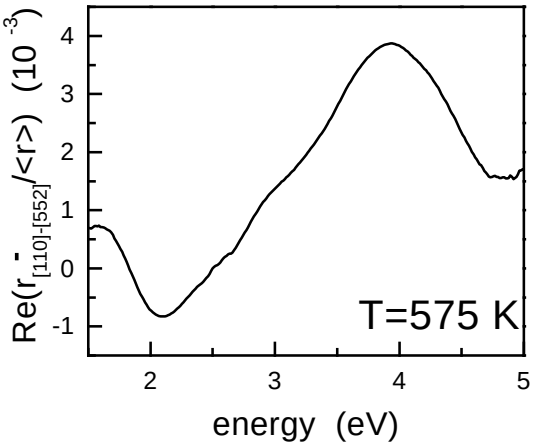

Figure 11.3: *RAS spectrum of the less arsenic rich reconstruction at 575 K in MOVPE.*

Summary

All investigated GaAs surfaces have showed at least two different reconstructions. At less arsenic rich conditions nearly all surfaces are covered by a reconstruction of arsenic dimers. The prototype for these reconstructions is the $\beta 2$(2x4) reconstruction on the (001) surface. Similar structures are the (8x1) reconstruction on the (113) surface, the p(2x2) on the (115) surface and probably also the p(2x1) on the (113) surface.

Another type of arsenic rich reconstruction consists of arsenic ad-atoms. The p(1x1) reconstructions on the (113) and (115) surfaces, as well as the arsenic monolayer on top of the (110) surface are such structures. The (4x3) reconstruction on the (001) surface might be an ad-atom structure too.

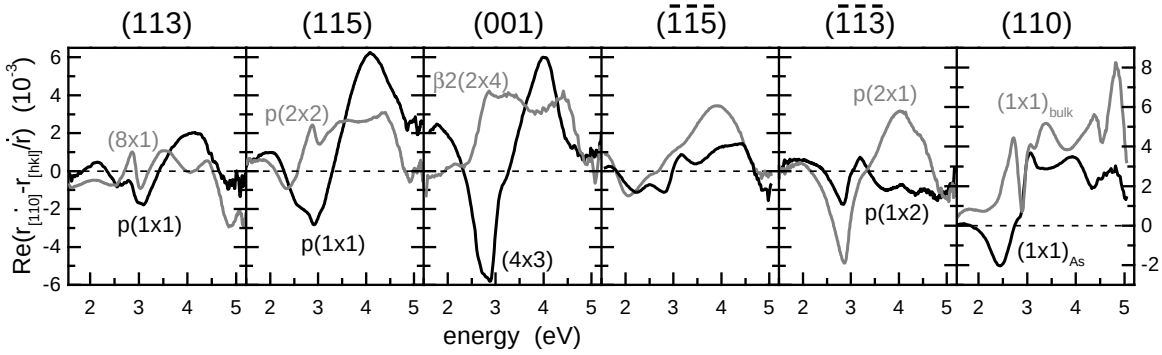

Figure 12.1: *RAS spectra at room temperature of the two most prominent reconstructions of different (hkl) surfaces (Black: arsenic rich, Gray: less arsenic rich).*

The RAS spectra of the two main reconstructions for each investigated surface are plotted in figure 12.1, grey lines correspond to less arsenic rich and black lines to very arsenic rich conditions. As a general trend the amplitude of the RAS spectra decreases from (001) over (115) to (113). This may be due to geometrical reasons: from (001) to (113) the surfaces become more and more tilted towards an isotropic (111)-like configuration. Thus the contribution of the dimers to the optical anisotropy becomes smaller. If this theory is true, the RAS spectra of the (331) and (551) towards (110) should increase again in amplitude.

The RAS spectra of the (001), (115) and (113) surfaces of the arsenic rich reconstructions (black lines in figure 12.1) all feature minima at 2.5 eV and at 2.96 eV (the E_1 transition) and a maximum at 4.0 eV. However, the line-shapes of the RAS spectra of (113), (115) and (110) surfaces are completely different.

The same can be found by comparing the less arsenic rich surface (gray lines in figure 12.1): (113), (115) and (001) surfaces are again quite similar, while the rest differs strongly.

The similarity of the RAS spectra is most likely due to a similar structure of the reconstructions, because an RAS spectrum is mostly sensitive to the surrounding of an atom or dimer. It seems that if an arsenic atom is bound on top of an arsenic monolayer, it causes a signal at 2.5 eV, 2.96 eV and 4.0 eV, and these energies do not change much with symmetry or orientation (the latter only damping the amplitude).

On these well-ordered surfaces arsenic desorption was investigated. The Arrhenius plot in figure 12.2 (left) shows slow reaction rates for the low-index (001) and (110) surfaces. The reaction rates are increasing with an increasing tilt up to the $\{113\}$ and $\{\bar{1}13\}$ surfaces, while the activation energy for arsenic desorption on the other hand decreases (table 12.1). The arsenic seems to be bound less tightly on the high index surfaces and therefore comes off more easily. Probably this is due to the strain on the arsenic bounds on the high-index surface, and the strain becomes larger, the higher their misorientation towards (001) surface.

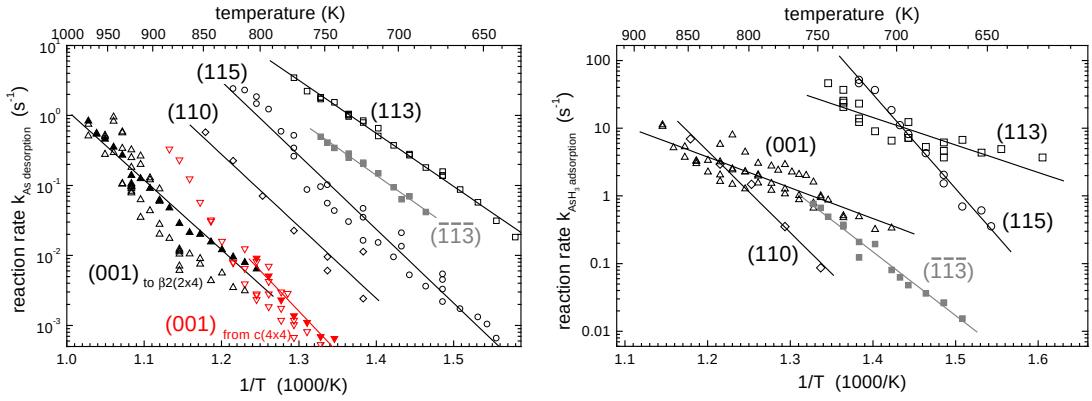

Figure 12.2: *Arrhenius plots of the arsenic desorption (left) and the AsH_3 adsorption (right) on all high-index surfaces in this study.*

surface	(113)	(115)	(001)	$(\bar{1}15)$	$(\bar{1}13)$	(110)
			reconstructions			
arsenic rich	p(1x1)	p(1x1)	(4x3) & c(4x4)	*	p(1x2)*	As-ML
less arsenic rich	(8x1)	p(2x2)*	β2(2x4) & α(2x4)	p(2x2)*	p(2x1)	bulk term.
gallium rich	–	–	(nx6) & (4x2)	–	??	
			arsenic desorption			
order of reaction	2.	2.	0. & 1.	??	1.	2.
activation energy	(1.50±0.02) eV	(2.09±0.07) eV	≈2.6 eV	??	(1.55±0.06) eV	(2.4±0.3) eV
			AsH_3 adsorption			
order of reaction	2.	2.	2.	??	2.	2.
activation energy	(1.38±0.15) eV	(4.09±0.14) eV	(1.1±0.2) eV	??	(1.87±0.08) eV	(2.4±0.4) eV
			gallium diffusion along $[\bar{1}10]$			
diffusion constant	(60± 40) nm	??	(0.6±0.4) m	??	??	??
activation energy	0.4 eV	??	2.8 eV	??	??	??

Table 12.1: *The different type of reconstructions on the different surfaces (??: not measured, *: structure not known, –: does not exist).*

The AsH_3 adsorption plotted in figure 12.2 (right) behaves quite differently. The adsorption on (113) and (115) surface is very fast, because these reconstructions consist of ad-atoms. Every arsenic atom sticks whenever it impinges on the surface. However, the very high activation energy of 4.09 eV for the (115) surface is very puzzling. This energy is higher than the desorption energy; it is even higher than the activation energy for the decomposition of AsH_3 in the vapor phase.

The (110), $(\bar{1}13)$, and (001) surfaces change much slower, and also have lower activation energies. On these surfaces a reordering of the reconstruction takes place, because the arsenic rich surfaces are more complex than the simple ad-atom structures on the (113) and (115) surfaces.

Finally, the diffusion along $[1\bar{1}0]$ direction was compared for the (113) and the (001) surfaces. Like the arsenic, the gallium species during diffusion seems to be bound less tightly to the (113) surface than on the (001) surface (see table 12.1). However, the diffusion constant on the (113) surface is much smaller than the one on the (001) surface, and thus the resulting diffusion lengths are comparable.

Appendix

Bibliography

[1] M. Pashley, Physical Review B **40**, 10481 (1989). 1.2

[2] S. B. Zhang and A. Zunger, Phys. Rev. B **53**, 1343 (1996). 1.4, 6.1.1, 6.4, 6.1.3

[3] A. Kley, pers. com., 1997. 1.6, 8.2

[4] L. Hollan and C. Shiller, J. Crystal Growth **13/14**, 319 (1972). 2.1, 2, 2.2

[5] W. Shaw, J. Electrochem. Soc. **115**, 405 (1968). 2.2, 9

[6] H. Haken, *Synergetics – An Introduction* (Springer-Verlag, Berlin Heidelberg New York, 1977). 3.1

[7] D. Kisker, G. Stephenson, P. Fuoss, and S. Brennan, J. Crystal Growth **146**, 104 (1995). 3.1.1, 6.6.1, 6.6.1, 6.6.1, 6.35, 3

[8] J. Amar and F. Family, Phys. Rev. B. **50**, 8781 (1994). 3.2.1, 3.2

[9] W. Burton, N. Cabrera, and F. Frank, Phil. Trans. Roy. Soc. Ldn A **243**, 299 (1951). 3.2.2

[10] J.-T. Zettler, J. Rumberg, K. Ploska, K. Stahrenberg, M. Pristovsek, W. Richter, M. Wassermeier, P. Schützendüwe, J. Behrend, and L. Däweritz, phys. stat. sol. (a) **152**, 35 (1995). 4.2.2, 6.6.1

[11] H. Manasewit, Appl. Phys. Lett. **12**, 156 (1968). 5

[12] M. Yoshida, H. Watanabe, and F. Usegi, J. Electrochem. Soc. **132**, 677 (1985). 5.1, 1, 5.2

[13] P. Lee, T. Omstead, D. McKenna, and K. Jensen, J. Crystal Growth **85**, 165 (1987). 5.1, 1

[14] J. Williams, R. Hoare, N. Hunt, and M. Parrot, Mat. Res. Soc.? 113 (1988?). 5.1, 1, 5.2

[15] C. Larsen, N. Buchan, and G. Stringfellow, Appl. Phys. Lett. **52**, 480 (1988). 5.1, 1, 1, 5.2, 6.28, 2, 6.7

[16] R. Lückerath, CARS-Untersuchungen der Reaktionskinetik im MOVPE-Prozess, Dissertation RWTH Aachen (1990). 5.1, 1, 1, 1, 5.2

[17] D. Gutsche, Untersuchung zum Wachstumsmechanismus neuer Ausgangsstoffe in der MOVPE, Diplomarbeit, TU-Berlin (1992). 5.1, 1, 5.2

[18] M. Jacko and S. Price, Can. J. Chem. **41**, 1560 (1963). 1

[19] S. Horiguchi, K. Kimura, S. Takagishi, K. Kamon, M. Mashita, M. Mihara, and M. Ishii, Jap. J. Appl. Phys. **26**, 2002 (1987). 1, 1, 2

[20] G. Stringfellow, *Organometallic Vapour-Phase Epitaxy: Theory and Practice* (Academic Press, San Diego, 1989). 1, 1, 1, 1, 1, 5.2

[21] D. Reep and S. Ghandhi, J. Electrochem. Soc. **130**, 675 (1983). 5.3, 1, 5.4

[22] P. Balk, M. Fischer, D. Grundmann, R. Lückerath, H. Lüth, and W. Richter, J. Vac Sci. Tech. B **5**, 1453 (1987). 5.3

[23] A. Robertson, T. Chiu, W. Tsang, and J. Cunningham, J. Appl. Phys. **64**, 877 (1988). 5.3

[24] W. Richter, P. Kurpas, and M. Waschbüsch, Appl. Surf. Sci. **54**, 1 (1992). 5.4

[25] L. Däweritz and R. Hey, Surf. Sci. **236**, 15 (1990). 6.1, 6.1.4, 6.5

[26] H. Qi, P. E. Gee, and R. F. Hicks, Surf. Sci. **347**, 289 (1996). 6.1.1, 6.3.1

[27] X.-Y. Zhu, M. Wolf, T. Huett, J. Nail, B.A.Banse, J. Creighton, and J. White, Appl. Phys. Lett. **60**, 977 (1992). 6.1.1

[28] B. Banse and J. Creighton, Appl. Phys. Lett. **60**, 856 (1992). 6.1.1, 6.1.2, 6.3.1, 6.3.2, 6.3.2, 6.3.4

[29] C. Sasaoka, Y. Kato, and A. Usui, Surf. Sci. Lett. **265**, L239 (1992). 6.1.1, 6.1.2, 6.3.2

[30] I. Chizhov, G. Lee, R. F. Willis, D. Lubyshev, and D. L. Miller, Phys. Rev. B **56**, 1013 (1997). 6.1.1

[31] C. Morgan, P. Kratzer, and M. Scheffler, Phys. Rev. Lett. **82**, 4886 (1999). 6.1.1

[32] A. P. Payne, P. H. Fouss, D. W. Kisker, G. B. Stephenson, and S. Brennan, Phys. Rev. B **49**, 14427 (1994). 6.1.2

[33] D. Kisker, G. Stephenson, I. Kamiya, P. Fuoss, D. Aspnes, L. Mantese, and S. Brennan, phys. stat. sol. (a) **152**, 9 (1995). 6.1.2, 6.1.4, 6.7, 6.6.1, 6.6.1

[34] B.-K. Han, L. Li, Q. Fu, and R. F. Hicks, J. Appl. Phys. **78**, 3347 (1998). 6.1.2, 6.1.6, 6.9

[35] D. Biegelsen, R. Bringans, J. Northrup, and L.-E. Swartz, Phys. Rev. B **41**, 5701 (1990). 6.1.2, 6.1.4, 6.1.5, 6.7

[36] V. Etgens, M. Sauvage-Simkin, R. Pinchaux, J. Massies, N. Jedrecy, A. Waldhauer, and N. Greiser, Surf. Sci. **320**, 252 (1994). 6.1.2, 6.3.2, 6.15

[37] K. Kanisawa and H. Yamaguchi, Phys. Rev. B **56**, 12080 (1997). 6.1.2, 6.3.2, 6.15

[38] U. Resch-Esser, N. Esser, D. Wang, , M. Kuball, J. Zegenhagen, B. Fimland, and W. Richter, Surf. Sci. **352-354**, 71 (1996). 6.1.2

[39] N. Moll, A. Kley, E. Pehlke, and M. Scheffler, Phys. Rev. B **54**, 8844 (1996). 6.1.3, 9.1, 9.1, 9.1.2

[40] V. P. LaBella, H. Yang, D. W. Bullock, P. M. Thibado, P. Kratzer, and M. Scheffler, Phys. Rev. Lett. **83**, 2989 (1999). 6.1.3

[41] T. Hashizume, Q.-K. Xue, A. Ichimiya, and T. Sakurai, Phys. Rev. B **51**, 4200 (1995). 6.1.3

[42] I. Kamiya, D. Aspnes, L. Florenz, and J. Harbison, Phys. Rev. B **46**, 15894 (1992). 6.1.4, 6.7, 6.8, 6.3.3

[43] L. Li, B.-K. Han, S. Gan, H. Qi, and R. Hicks, Surf. Sci. **398**, 386 (1998). 6.1.4, C

[44] I. Chizhov, G. Lee, R. F. Willis, D. Lubyshev, and D. L. Miller, Surf. Sci. **419**, 1 (1998). 6.1.4, 6.3.3

[45] M. Kuball, D. Wang, N. Esser, M. Cardona, J. Zegenhagen, and B. Fimland, Phys. Rev. B **51**, 13880 (1995). 6.1.4

[46] Q. Xue, T. Hashizume, J. Zhou, T. Sakata, T. Ohno, and T. Sakurai, Phys. Rev. Lett. **74**, 3177 (1995). 6.1.5, 6.4.2

[47] J. R. Creighton and K. Baucomm, Surf. Sci. **409**, 372 (1998). 6.1.6, 6.1.6, 6.9, 6.1.7, 6.10, 6.4.2, 6.4.2, 6.22, 6.7

[48] I. Kamiya, L. Mantese, D. Aspnes, D. Kisker, P. Fuoss, G. Stephenson, and S. Brennan, J. Crystal Growth **163**, 67 (1996). 6.1.6, 6.5, 6.6.1

[49] Q. Fu, L. L. M. Begarney, , B.-K. Han, D. Law, and R. Hicks, J. de Physique IV **9**, Pr8.3 (1999). 6.1.6, 6.1.7

[50] J. R. Creighton, B. Bansenauer, T. Huett, and J. White, J. Vac. Sci. Tech. A **11**, 876 (1993). 6.1.7, 6.4.2

[51] P. E. Gee, H. Qi, and R. F. Hicks, Surf. Sci. **330**, 135 (1995). 6.1.7, 6.4.2

[52] D. E. Aspnes, I. Kamiya, H. Tanaka, and R. Bhat, J. Vac. Sci. Tech. B **10**, 1725 (1992). 6.1.7, 6.4.2, 6.4.2

[53] R. Arès, S. Watkins, P. Yeo, G. Horley, P. O'Brian, and A. Jones, J. Appl. Phys. **83**, 3390 (1998). 6.1.7, 6.4.1, 6.4.1, 6.4.2, 6.4.2

[54] Y. Yamauchi, K. Uwai, and N. Kobayashi, Jpn. J. Appl. Phys. **32**, 3363 (1993). 6.3.1, 6.3.2, 6.3.4

[55] J. Rumberg, J.-T. Zettler, K. Stahrenberg, K. Ploska, W. Richter, L. Däweritz, P. Schützendüwe, and M. Wassermeier, Surf. Sci. **337**, 103 (1995). 6.3.2, 6.6.1

[56] S. Tsukamoto, Natinal Research Institut for Metals Tsukuba, pers. com., 2000. 6.3.2

[57] J. Nishizawa, T. Kurbayashi, H. Abe, and A. Nozoe, Surf. Sci. **185**, 249 (1987). 6.4.2, 8, 8.1.2, 8.1.2, 10, 10.3

[58] H. Hardtdegen, M. Pristovsek, H. Menhal, J.-T. Zettler, W. Richter, and D. Schmitz, J. Crystal Growth **195**, 211 (1998). 2, 6.6.1

[59] K. Ploska, M. Pristovsek, W. Richter, J. Jönsson, I. Kamiya, and J.-T. Zettler, phys. stat. sol. (a) **152**, 49 (1995). 2, 6.6.1

[60] J. Nishizawa and T. Kurbayashi, J. Cryst. Growth **93**, 98 (1988). 6.28, 2

[61] S. Armstrong, R. Hoare, M. Pemble, I. Povey, A. Stafford, A. Taylor, and J. Williams, J. Cryst. Growth **124**, 10 (1992). 6.28, 2

[62] F. Reinhardt, W. Richter, A. Müller, D. Gutsche, P. Kurpas, K. Ploska, K. Rose, and M. Zorn, J. Vac. Sci. Tech. B **11**, 1427 (1993). 6.6.1, 6.6.1

[63] J. Neave, B. Joyce, P. Dobson, and N. Norton, Appl. Phys. A **31**, 1 (1983). 6.6.1

[64] J. van Hove, C. Lent, P. Pukite, and P. Cohen, J. Vac. Sci. Tech. B **1**, 714 (1983). 6.6.1

[65] K. Ploska, J.-T. Zettler, W. Richter, F. Reinhardt, J. Rumberg, M. Pristovsek, M. Zorn, D. Westwood, and R. Williams, J. Crystal Growth **145**, 44 (1994). 6.6.1

[66] J. Neave, P. Dobson, B. Joyce, and J. Zhang, Appl. Phys. Lett. **47**, 100 (1985). 6.6.1, 6.6.1, 3

[67] T. Shitara, D. Vvendensky, M. Wilby, J. Zhang, J. Neave, and B. Joyce, Phys. Rev. B **46**, 6825 (1992). 6.6.1, 6.32, 6.6.1, 3

[68] T. Shitara, J. Zhang, J. Neave, and B. Joyce, J. Appl. Phys. **71**, 4299 (1992). 6.6.1

[69] C. Heyn and M. Harsdorff, Phys. Rev. B **55**, 7034 (1997). 6.6.1, 3

[70] C. Heyn, T. Franke, R. Anton, and M. Harsdorff, Phys. Rev. B **56**, 13483 (1997). 6.6.1

[71] T. Fukui, J. Ishizaki, S. Hara, J. Motohisa, and H. Hasegawa, J. Crystal Growth **146**, 183 (1995). 6.35, 3

[72] M. Kasu and N. Kobayashi, J. Appl. Phys. **78**, 3026 (1995). 6.35, 3, 6.6.3

[73] M. Pristovsek, H. Menhal, J.-T. Zettler, and W. Richter, Appl. Surf. Sci. **166**, 433 (2000). 3

[74] D. Law, L. Li, M. Begarney, and R. Hicks, J. Appl. Phys **88**, 508 (2000). 3, 6.6.3

[75] J. LePage, M. Alouani, D. L. Dorsey, J. Wilkins, and P. Blöchl, Phys. Rev. B **58**, 1499 (1998). 3

[76] N. Kobayashi, T. Makimoto, and Y. Horikoshi, Appl. Phys. Lett. **50**, 1435 (1987). 6.7

[77] W. Nakwaski, phys. stat. sol (a) **132**, K47 (1992). 6.7

[78] M. Kondo and T. Tanahashi, J. Crystal Growth **145**, 390 (1994). 6.7

[79] Y. Ashizawa, T. Noda, K. Morizuka, and M. Obara, J. Crystal Growth **107**, 903 (1991). 6.36, 6.38

[80] S. Tanaka, S. Kato, S. Hattori, S. Kojima, M. Ikeda, and K. Kitamura, J. Crystal Growth **145**, 947 (1994). 6.36

[81] F. Dimroth, U. Schubert, F. Schienle, and A. Bett, J. Electr. Mat. **29**, 47 (2000). 6.36

[82] M. Kushibe, K. Eguchi, M. Funamizu, and Y. Ohba, Appl. Phys. Lett. **56**, 1248 (1990). 6.7

[83] K. Young, A. Kahn, and J. Philips, J. Vac. Sci. Tech. B **10**, 71 (1992). 7, 7, 11, 11

[84] M.-S. Kim, Y. Kim, M. Lee, Y. Park, S. Kim, and S. Min, J. Crystal Growth **139**, 231 (1994). 7

[85] C. Setzer, Die geometrische und elektronische Struktur epitaktisch gewachsener GaAs{111}-, {113}- und {115}-Oberflächen, Dissertation Fritz-Haber-Institut Berlin, Wissenschaft & Technik Verlag Berlin, ISBN 3-89685-455-0 (1997). 7.1.2, 10, 11.1.2

[86] R. Nötzel, L. Däweritz, and K. Ploog, Phys. Rev. B **46**, 4736 (1992). 8

[87] M. Wassermeier, J. Sudijono, M. Johnson, K. Leung, B. Orr, and L. D. und K. Ploog, J. Crystal Growth **150**, 425 (1995). 8, 8, 8.1.1

[88] P. Moriaty, Y.-R. Ma, A. Dunn, P. Beton, M. Henini, C. McGinley, E. McLoughlin, A. Cafolla, G. Hughes, S. Downes, D. Teehan, and B. Murphy, Proc. of the 23. ICPS Berlin **2**, 879 (1996). 8, 8, 8.1.2

[89] C. Setzer, J. Platen, P. Geng, W. Ranke, and K. Jacobi, Surf. Sci. **377-379**, 125 (1997). 8, 8.1.1

[90] C. Setzer, J. Platen, W. Ranke, and K. Jacobi, Surf. Sci. **419**, 291–302 (1999). 8, 10, 10

[91] J. Platen, A. Kley, C. Setzer, K. Jacobi, P. Ruggerone, and M. Scheffler, J. Appl. Phys. **85**, 3597 (1999). 8, 8.1, 8.1.1, 8.1.2, 10, 10.2

[92] R. Nötzel, J. Temmyo, and T. Tamamura, Appl. Phys. Lett. **64**, 3557 (1994). 8, 8.4, 8.6

[93] M. Pristovsek, H. Menhal, J.-T. Zettler, T. Schmidtling, N. Esser, W. Richter, C. Setzer, J. Platen, and K. Jacobi, J. Crystal Growth **195**, 1 (1998). 8.4

[94] P. Hanesch and E. Bertel, Phys. Rev. Lett. **79**, 1523 (1997). 8.4

[95] V. Berkovits, I. Marenko, T. Minashvili, and V. Safarow, Sol. State Comm. **56**, 449 (1985). 9, 9.1.1, B.2

[96] W. Shaw, Symposium on GaAs **paper 8**, 51 (1968). 9

[97] K. Okamoto, M. Furuta, and K. Yamaguchi, Jap. J. Appl. Phys. Lett. **27**, L437 (1988). 9

[98] M. Takeuchi, K. Shiba, K. Sato, H. K. Huang, K. Inoue, and H. Nakashima, Jpn. J. Appl. Phys. **34**, 4411 (1995). 9, 9.3

[99] P. Tejedor, F. Allegretti, P. Šmilauer, and B. Joyce, Surf. Sci **407**, 82 (1998). 9, 9.3

[100] H. Kiziku, Y. Kajikawa, Y. Hisa, and Y. Mihashi, J. Crystal Growth **194**, 277 (1998). 9, 9.3

[101] D. Holmes, E. Tok, J. Sudijono, T. Jones, and B. Joyce, J. Crystal Growth **192**, 33 (1998). 9, 9.3

[102] F. Manghi, R. D. Sole, A. Selloni, and E. Molinari, Phys. Rev. B **41**, 9935 (1990). 9.1.1

[103] O. Pulci, G. Onida, C. Kress, A. Shkrebtii, and R. D. Sole, Proc. of the 23. ICPS, Berlin 815 (1996). 9.1.1

[104] N. Esser, R. Hunger, J. Rumberg, W. Richter, R. Del Sole, and A. I. Shkrebtii, Surf. Sci. **307-309**, 1045 (1994). 9.2, 9.1.2

[105] J.-H. Cho, Z. Zhang, S.-H. Lee, and M.-H. Kang, Phys. Rev. B **59**, 12200 (1999). 9.1.2

[106] O. Pulci, Universität Jena, pers. com., 2000. 9.1.2

[107] B. Kübler, W. Ranke, and K. Jacobi, Surf. Sci. **92**, 519 (1980). 9.1.2

[108] Z. He, Y. Khazmi, J. Kanski, L. Ilver, P. Nilsson, and U. Karlsson, J. Vac. Sci. Tech. A **15**, 1515 (1997). 9.1.2

[109] E. Tok, J. Neave, M. Fahy, F. Allegretti, J. Zhang, T. Jones, and B. Joyce, Microelectronics Journal **28**, 833 (1997). 9.3

[110] R. Nötzel, J. Temmyo, and T. Tamamura, letters to nature **369**, 131 (1994). 10

[111] J. Temmyoa, E. Kuramochia, H. Kamadab, and T. Tamamura, J. Crystal Growth **195**, 516 (1998). 10

[112] M. Kawase, Y. Ishikawa, and T. Fukui, Appl. Surf. Sci. **130-132**, 457 (1998). 10, 10.3, 10.1.2

[113] K. Jacobi, Fritz-Haber-Institut Berlin, pers. com., 2000. 10.1.2

[114] D. E. Aspnes, J. P. Harbison, A. A. Studna, L. T. Florez, and M. K. Kelly, J. Vac. Sci. Tech. A **6**, 1327 (1988). B.2

[115] J.-T. Zettler, Progress in Crystal Growth and Characterization of Materials **35**, 27 (1997). B.2

[116] J. Rumberg, Development and Optimization of the Reflectance Anisotropy Spectroscopy (RAS) Technique with Respect to Online Growth Control, Diplomarbeit, TU-Berlin (1993). B.1, B.2

[117] P. Redhead, Vacuum **12**, 203 (1962). B.2

[118] T. Schmidtling, Entwicklung einer MOVPE-Anlage mit UHV-Transfer, Diplomarbeit, TU-Berlin (1998). C

[119] M. Kasu and N. Kobayashi, Jpn. J. Appl. Phys. **33**, 712 (1994). C

[120] T. Hannappel, S. Visbeck, K. Knorr, J. Mahrt, M. Zorn, and F. Willig, Appl. Phys. A **69**, 427 (1999). C

B Compendium of the Methods Used in this Work

B.1 Epitaxial Growth

ALE – Atomic Layer Epitaxy

This is a special growth mode using an alternating supply of precursors. In MOVPE, in several material systems, it is possible to achieve a self-limiting growth rate, i.e. the growth rate is constant for a wide range of parameters. However, self-limiting ALE growth is only possible with special precursors.

In MBE a growth mode using alternating supplies is often called Migration Enhanced Epitaxy (MEE). Usually MEE growth is not self-limiting.

UHV – Ultra-High Vacuum

Not a growth method, but simply the abbreviation of Ultra-High Vacuum.

MBE – Molecular Beam Epitaxy

Growth using molecular beams from effusion cells (i.e. ovens with only a small opening). Due to the use of molecular beams this method requires UHV conditions. Many in-situ (i.e. during growth) investigations are possible, since nearly all UHV-based surface science methods can be used. Usually an MBE growth chamber is equipped with a RHEED (Reflection High Energy Electron Diffraction) measurement system.

MOMBE – Metal-Organic Molecular Beam Epitaxy

MOMBE is also called CBE (Chemical Beam Epitaxy) or GS-MBE (Gas Source MBE). Instead of effusion cells, beams of partly cracked precursors are used. Since the cracking of precursors usually produces a lot of methane or hydrogen, the background pressure during growth is quite high (about 10^{-7} Pa). Therefore, UHV-based surface science methods are difficult to use during MOMBE growth.

MOVPE – Metal-Organic Vapor Phase Epitaxy

MOVPE is also called MOCVD (Metal-Organic Chemical Vapor-phase Deposition), OMVPE (Organo-Metallic …), or OMCVD. Many materials can be grown by MOVPE, such as single crystal layers, coatings, or even superconductors.

The principle is very simple. Precursor molecules are transported by a carrier gas into a reactor. In the reactor the precursor(s) are decomposed, usually by heating, but plasma discharge and other methods are also possible. The precursors decompose and release the atoms or molecules which are deposited.

There are many different layouts of MOVPE reactors. There are double wall systems or hot wall reactors, the gas may enter vertically or flows horizontally through the reactor. The sample(s) may rotate along different axes, or it is tilted towards the gas flow.

All MOVPE reactors have working pressures during growth in the range of 100 up to 100 kPa. MOVPE processes using atmospheric pressure are sometimes denoted as AP-MOVPE, and low pressure MOVPE, consequently, LP-MOVPE. A typical LP-MOVPE process has a pressure of 2 or 10 kPa.

These pressures are far too high for the use of electron based methods for growth analysis. Therefore only optical and scanning probe methods can be used to analyze MOVPE growth.

VPE – Vapor Phase Epitaxy

This term is often used with two meaning: first as a general classification of growth processes that use precursors and a carrier gas. However, VPE often means Cl-VPE, a growth method which uses $AsCl_3$ or HCl to etch a "solid" gallium source and to form in-situ $GaCl_3$ which decomposes on the hot substrate.

Cl-VPE has two advantages, firstly a very high growth rate. Secondly, due to the in-situ etching during the heating of the substrate no pretreatment of the wafers is needed. But nowadays substrates of good "epi-ready" quality are widely used, and instead of high growth rate a very precise control of layer thickness is needed.

B.2 Surface Science Methods

The methods used for the investigation of the GaAs surfaces will very briefly reviewed in this section, together with a short discussion of their relevance towards the understanding of the growth process. In principle there are three different classes of methods. First the "traditional" ones using electrons, which need Ultra-High Vacuum (UHV). Then there are light based methods (X-Ray, visible or infra red (IR)), which only need a transparent ambient. And finally, since about ten years the new class of scanning probe microscopes (SPM) have been available.

Electrons have been the standard tools for surface science since the beginning, because by using the right energy, their wavelength can be tuned to the length scale of interatomic distances. Free electrons also interact very directly with the bound electrons of the target atoms. However, electrons require a vacuum less than 10^{-3} Pa, otherwise their mean free path becomes too short, and they lose all their information in scattering events. Light and the SPM however, can be used at any pressure. Hence these are very interesting for investigation in-situ in MOVPE.

To investigate samples with traditional surface science methods, transfer procedures from MOVPE reactors to UHV chambers were established (see appendix C).

AES - Auger Electron Spectroscopy

Electrons of the inner shells are excited and relax by an Auger process. As a result an electron is emitted which has a characteristic energy. These electrons are detected, and from their energy the presence of certain elements can be measured. Usually the excitation is done by electrons with energies of a few keV. Because of the use of electrons, AES works only in UHV.

Dependent on the energy of the transition used, the composition of the first few monolayers can be deduced from an Auger spectrum.

GIXD - Gracing Incidence X-ray Diffraction

X-rays with a wavelength of the order of the interatomic distances are irradiated at shallow angles (typical less than $0.2°$) on to the surface. The diffracted X-rays are directly measured by scanning a hemisphere with the detector. Therefore, GIXD is the optical equivalent to LEED.

Many different kinds of information can be obtained by GIXD, apart from simple symmetry measurements. There is, for example, the crystal truncation rod (CTR) which tells us about the degree of roughness on the surface. The intensity of different diffraction peaks can also be compared to calculated peak intensities to decide between different models for a surface. And since X-rays are only weakly interacting with matter, GIXD can also be done in-situ in an MOVPE reactor.

These are many advantages which make this method very attractive for in-situ investigations of MOVPE growth. But there are some severe disadvantages. Firstly, the typical high-intensity X-ray source is a synchrotron, thus many safety concerns have to be taken into account and one has to apply for beam-time (typically available only for a few weeks a year and quite expensive). Secondly, the whole MOVPE reactor and sample mount must be extremely stable, since the change of the incident angle must be less than a percent. Thirdly, the data acquisition times for a scan to determine the symmetry of a surface are long and may take several hours (depending on the number of peaks scanned).

HREELS - High Resolution Electron Energy Loss Spectroscopy

HREELS can detect vibrations on a surface, which are usually caused by adsorbates. The loss of the kinetic energy of very slow electrons (less than 10 eV kinetic energy) is measured with high accuracy. Peaks in the resulting energy loss spectrum correspond to elementary excitations of phonons or vibrational modes in the range of 10 to 500 meV. Since electrons are very slow and measurement times are long (some hours) a very good vacuum is needed. Thus, to apply HREELS to an MOVPE grown surface, an MOVPE to UHV sample transfer system is needed.

The corresponding optical method, IR-spectroscopy, which measures directly IR active vibrations, is in principle a true in-situ method, but due to very small signals, it is experimentally very difficult to use.

LEED - Low Energy Electron Diffraction

LEED has its origin in the 1920s, because its principle is simple. Electrons with kinetic energies between 20 and 200 eV impinge perpendicular on to a surface. Since the *de-Broglie* wavelength of such electrons is close to the interatomic distances on the surface, a good part of the electrons are diffracted. The reflected, scattered, and diffracted electrons are focused on to a phosphorous screen.

The distances between the diffraction spots on the screen are reciprocal to the periodicities on the real surface. If there is a gap every two atoms, then the LEED image will have a spot at one half of the reciprocal unit mesh. Thus, a LEED image is showing the periodicity of the structures on a surface. By comparing images recorded at different energies, one can also get information about facets (if present).

The complicated part of LEED is quantitative analysis. For that purpose a special set-up, called SPA-LEED (Spot-Profile Analyzing LEED) is used. The change of the brightness of different spots in the LEED images at different electron energies is then compared with calculated brightness curves for different models of the surface.

Since LEED needs high vacuum conditions, it can only be used after MOVPE growth, with an MOVPE to UHV transfer system.

RHEED (Reflection High Energy Electron Diffraction), a technique related to LEED, is normally used in MBE for in-situ measurements of reconstructions and growth rates. However, due to its different geometry and energies only symmetries perpendicular to the incident beam are measured.

RAS - Reflectance Anisotropy Spectroscopy

RAS measures the spectral dependence of the change of polarization of linear polarized light after reflection from the surface [95, 114, 115]. Usually only the real part of the complex reflection is used.

RAS is a linear optical method. Therefore the size of signals can be directly related to the coverage (see sec. 4). The time resolution is of the order of 50 ms, a tenth of the time for the growth of a monolayer, which makes RAS a very fast method.

RAS is very sensitive to the bond arrangement of a reconstruction but not to symmetry. This makes diffraction techniques and RAS ideal complementary partners to detect a well-ordered reconstruction, since there often exists different reconstructions with the same symmetry, which can be separated by their RAS spectra.

However, to interprete an RAS spectrum, one has to have a set of reference RAS spectra, measured on well-ordered reconstructions which were characterized by other methods. In the near future good reference RAS spectra might also be obtained by calculations.

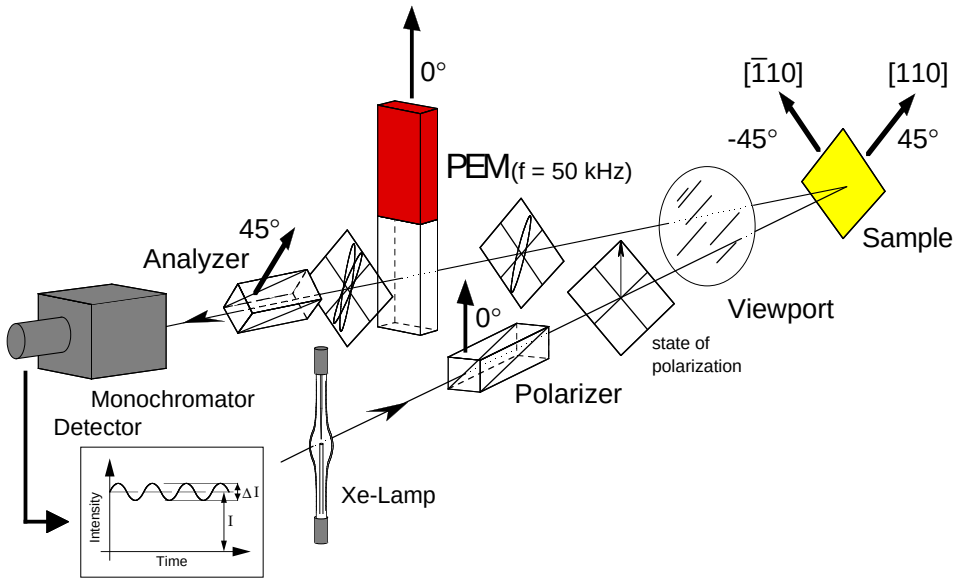

Figure B.1: *Principal set-up of the RAS spectrometers used in this work [116].*

RAS works with any transparent media. It only needs an optical port perpendicular to the surface, and the optical setup is quite simple. Thus RAS has become the standard technique for the analysis of MOVPE growth. However, RAS does not work on any single crystal surface. It needs two perpendicular main axes on the surface. Table B.1 lists the axes for different high-index surfaces. The general formula is:

$$\left(\frac{\Delta r}{r}\right)_{(hkl)} = 2\frac{r_{[1\bar{1}0]} - r_{[xyz]}}{r_{[1\bar{1}0]} + r_{[xyz]}} \tag{B.1}$$

with (hkl), $[xyz]$ and $[1\bar{1}0]$ being three perpendicular directions.

Therefore RAS works well on most fcc crystals surfaces, but not on the $\{111\}$ and $\{\overline{111}\}$ surfaces. The main axes on these surfaces have an angle of 60°, therefore any anisotropy signal at 90° is canceled out due to geometrical reasons.

surface	direction – direction	
(001)	$[1\bar{1}0]$ $[110]$	
(113)	$[1\bar{1}0]$ $[33\bar{2}]$	
(114)	$[1\bar{1}0]$ $[22\bar{1}]$	"A"-surfaces
(115)	$[1\bar{1}0]$ $[552]$	
(111)	_ not possible	
$(11\bar{0})$	$[1\bar{1}0]$ $[001]$	
$(11\bar{1})$	_ not possible	
$(11\bar{3})$	$[1\bar{1}0]$ $[332]$	
$(11\bar{4})$	$[1\bar{1}0]$ $[221]$	"B" surfaces
$(11\bar{5})$	$[1\bar{1}0]$ $[552]$	

Table B.1: *The two axes along the optical anisotropy is measured for different high-index surfaces.*

The most common set-up which is used by many groups is shown in figure B.1. In this case, linear polarised light is shone onto the surface at 45˚ to the surface eigen-axis (see table B.1). The reflected light is slightly elliptical polarised. The polarisation state is analysed using a photo-elastic modulator (PEM) and an analyser (polariser at 45˚ to the PEM main axis orientation). The modulator usually works at 50 kHz. The change of polarisation is now converted into an intensity modulation, which is measured by a Lock-In amplifier. The signal for real part $Re(\Delta r)$ is is at 2ω=100 kHz, while the signal for imaginary part can be found at ω=50 kHz. Since Δr is then normalised to the total intensity r it is possible to make absolute measurements, i.e. there is no need for a reference surface.

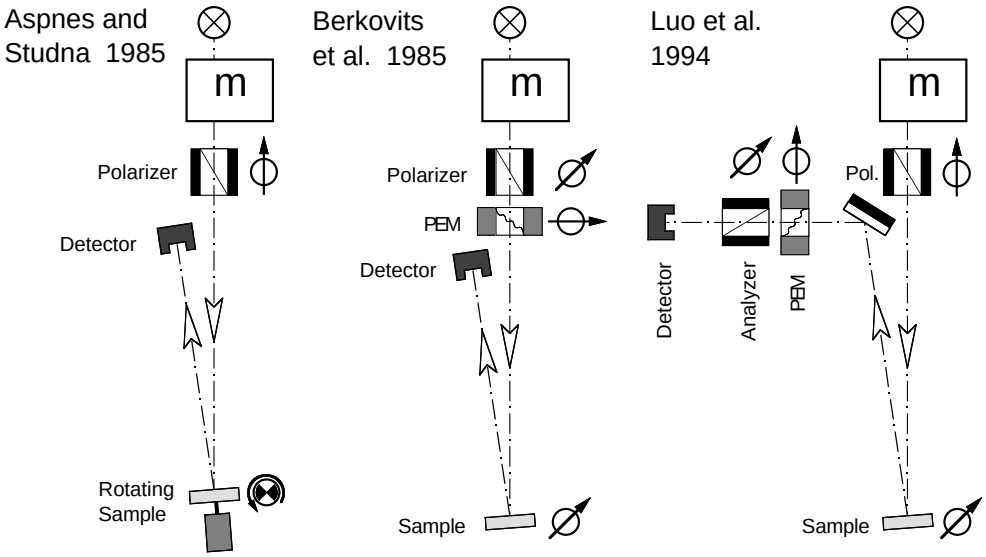

Figure B.2: *Other RAS set-up used in literature (after [116]).*

There have been other ways of measuring $\frac{\Delta r}{r}$. Since the PEM is quite expensive, simple set-up just rotate the sample (fig. B.2 left). Such set-up can measure absolute values with high accuracy and are not effected by and non-idealities from windows, if only the sample does not wobble during rotation. Other set-up using a PEM just modulated the polarisation

of the incident light, i.e. put the PEM in the incident beam (fig. B.2 middle). Then only a single polarizer is needed. However, the set-up show here is quite sensitve to stray light, and only the real part of an RAS signal can be measured.

SPA - Surface Photo Absorption

This optical technique is a close relative of RAS, and has also been used in MOVPE. SPA measures the intensity polarized light reflected by the surface. For high sensitivity the incident angle of the light is close to the Brewster angle.

This technique has the advantage of being able to measure the anisotropic as well as the isotropic part of the surface dielectric function. Therefore SPA works even on $\{111\}$ surfaces, where RAS does not work. Also SPA can made very fast by using multichannel detection (CCD), i.e. a full spectrum can be measured in less than 100 ms.

However, there are also some severe disadvantages. Firstly, two optical viewports near the Brewster angle are needed. Secondly it is hard (if not impossible) to measure absolute data. Usually only the change in the signal relative to a reference surface is recorded. All further analysis relies on the reference surface, or the results cannot be properly interpreted. These two disadvantages discourage greatly the use of SPA.

SPM - Scanning Probe Microscopes

SPM is the name for a whole class of methods. Using piezo-electric scanners a sensor is moved by a feed-back loop very close to the surface. There are different method of maintaining a feed-back. The oldest and most commonly used is Scanning Tunneling Microscopy (STM). The sensor is a sharp tungsten or platinum tip very close to the surface. A voltage difference is applied between the surface and the tip. The resulting tiny tunneling current (typically pA or nA) depends exponentially on the distance of the tip from the surface. The surface is now scanned line by line, and from the tunneling current (or a feedback loop, which keeps the current constant) the height information of the surface can be extracted.

STM works at pressures below 10^{-2} Pa and above 10 Pa, otherwise a glow discharge takes place instead of proper tunneling. Although STM at elevated pressures or temperatures has been done, up to now no successful in-situ operation in an MOVPE reactor has been reported.

Another commonly used technique is Atomic Force Microscopy (AFM). The height information in this case is the force of the surface on the probing tip. AFM is usually used for ex-situ characterization, although AFM can be measured in UHV, at elevated pressures, and even in liquids. But again no results of in-situ AFM during MOVPE growth exists.

TDS - Thermal Desorption Spectroscopy

TDS measures the increase of pressure while increasing the sample temperature. More sophisticated set-ups use mass spectroscopy and constant heating rates. At certain surface temperatures, adsorbed atoms desorb, resulting in high (partial) pressure rises. When all atoms are desorbed the pressure drops again, until the next species can desorb. Thus, each desorption process leads to a peak in the TDS spectrum. From the desorption temperature and peak shape the reaction order and activation energies of the respective desorption process can be calculated. However, the activation energies have an uncertainty of about 50 %, since the pre-exponential factor has to be guessed for the calculation [117] (see sec. 4).

While TDS, in principle, works at any pressure (as long as partial pressure measurements are possible), to my knowledge, TDS has only been used in UHV. (At atmospheric

pressure conditions partial pressure measurements could be done using optical absorption spectroscopy, where sensitivities for C_xH_y of ppb can be reached.)

C MOVPE – UHV Transfer System

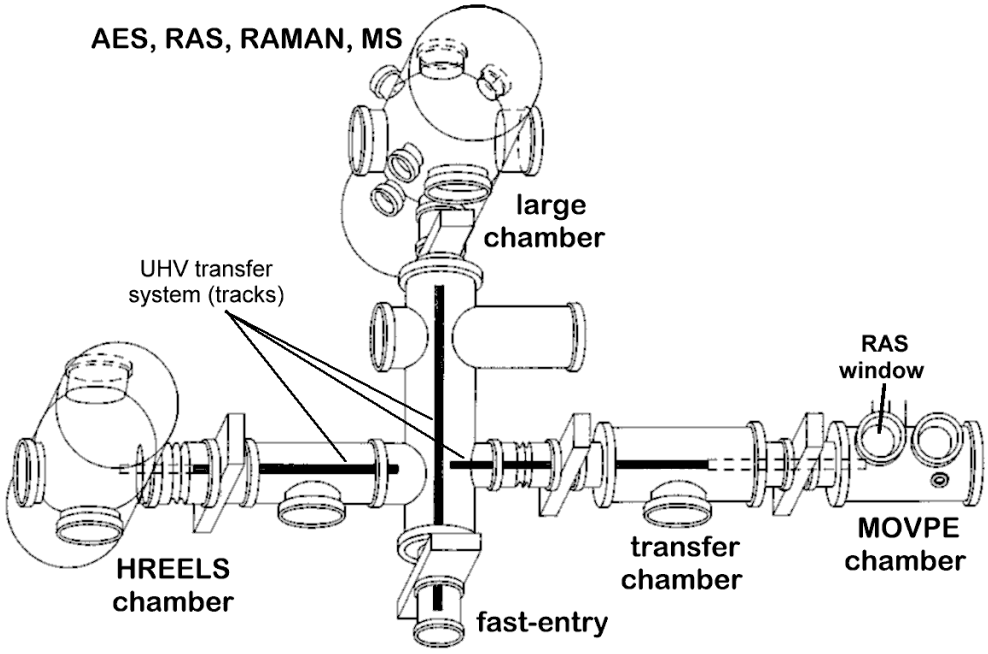

Figure C.1: *Overview of the MOVPE to UHV transfer chamber set-up.*

Figure C.1 show the systematic set-up of our UHV-MOVPE chamber system [118]. The growth chamber is equipped with an graphite susceptor heated by a boron nitride resistor in an inner round quartz liner tube. Samples can be either loaded by the fast entry or directly via a KF-flange at the MOVPE chamber. Details of the transfer system as one the optimization of the transfer procedure can be found in [118]. Since the subject of connecting MOVPE to UHV is of special interest, as works of other groups proved [119, 120, 43], a detailed description of the sample transfer procedure used is given here.

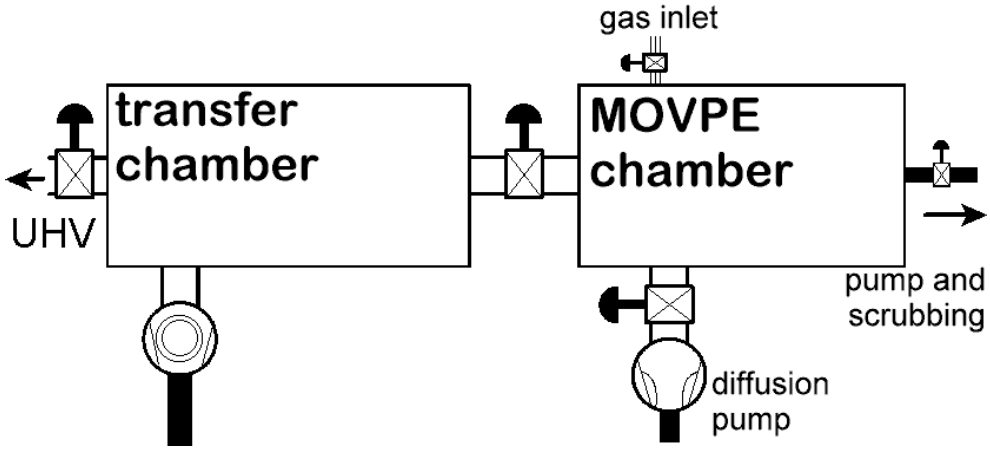

Figure C.2: *Old set-up of the transfer mechanism.*

In the first experiments the whole MOVPE chamber was evacuated by a strong pump (either a diffusion pump or a rotary pump). This set-up is shown in figure C.2. However,

it turned out that the residual hydro-carbon from the growth process goes into the stainless steel chamber walls, and came back to the sample's surface, when the MOVPE chamber was evacuated. The HREELS spectrum in figure C.4 showed strong C-H-contaminations (upper spectrum).

With these result in mind the set-up was changed. This new set-up is shown in figure C.3. A purging line for purified hydrogen was attached to the transfer chamber, and the high vacuum pumping system was completely removed from the MOVPE chamber. Only the MOVPE process pump remained, which was regulated by a throttle valve to a chamber pressure of 10 kPa during MOVPE.

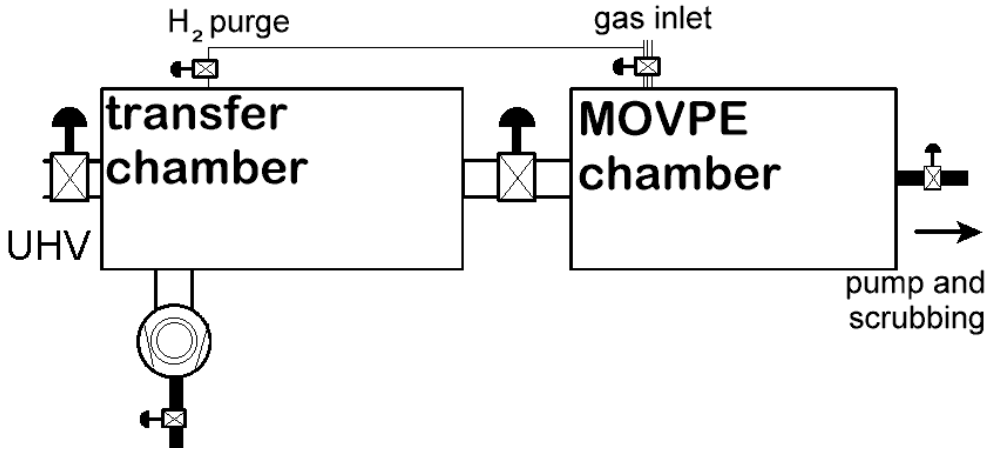

Figure C.3: *Set-up of the optimized transfer mechanism.*

The samples were prepared in the MOVPE chamber with an inner quartz liner tube at standard conditions: 1 l/min of 10 kPa H_2 Pd-diffused and 200 Pa AsH_3. The buffer was grown at 900 K with 0.5 Pa TMGa resulting in a growth rate of 850 nm/h. After buffer growth the samples were cooled under an AsH_3 flow down to 475 K and after that with pure H_2 to room temperature.

Before transfer, the transfer chamber was purged three times and then flooded with Pd-diffused H_2 before the connection valve between the MOVPE and transfer chamber was opened. After the sample was loaded into the transfer chamber, the connection valve was closed again, the H_2 purge was stopped and the transfer chamber was evacuated by a rotary pump (usually reaching 10^{-4} Pa after two minutes). Then the second valve to the UHV analysis transfer system was opened, and the sample was transfered to one of the UHV analysis chambers.

AES measurements of such prepared samples have shown no oxygen and only very minor carbon contamination. The C-H-vibration related peaks found in HREELS were smaller than the one of decapped MBE grown samples (fig. C.4).

RAS spectra before and after transfer in the analysis chamber were identical, confirming that the transfer method indeed preserves the reconstruction.

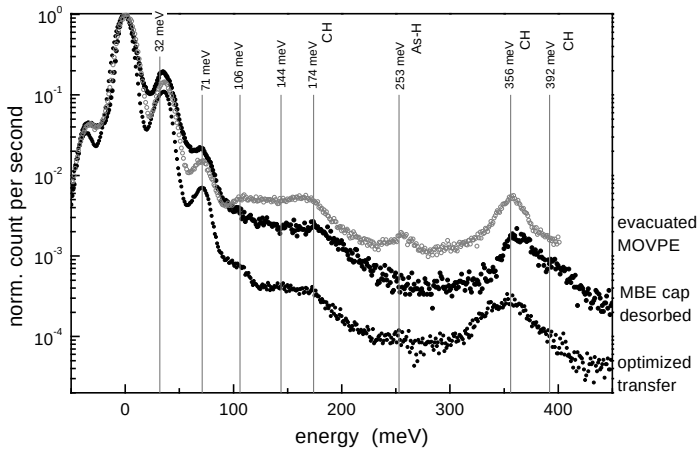

Figure C.4: *HREELS measurements of different samples. Evacuated MOVPE means that the MOVPE chamber was directly evacuated to transfer the sample. Optimized transfer means the transfer process under H_2 purge, as described in the text.*

D Thanks to . . .

. . . Prof. Dr. Wolfgang Richter for the chance to work in his group, which was much more than only physics.

. . . Dr. Jörg-Thomas Zettler for working together in many experiments, for his many ideas concerning experiments in the MOVPE, and for being always open for discussion. No to forget his efforts to organize at least an excursion a year.

. . . Dr. Norbert Esser for telling me the UHV surface analysis secrets, and for many discussions about the properties of surfaces.

. . . Prof. Dr. Karl Jacobi from the Fritz-Haber-Institute for the chance to make (unfortunately too few) RAS measurements in MBE, and for the freely discussion of the latest results of his MBE-STM group.

. . . Dr. Kerstin Knorr, Dr. Martin Zorn for sharing the up and down of maintaining MOVPE together with:

. . . Elisabeth Steimetz, Christian Meyne, Florian Poser, Torsten Schmidtling and Kolja Haberland, the next generation MOVPE PhDs.

. . . Dr. Klaus Tempelhoff for his previous work on the UHV-MOVPE.

. . . Karsten Fleischer and Patrick Vogt for proof-reading.

. . . the students which did their diploma work under my supervision: Housni Menhal and Bing Han.

. . . poor uncle network, as there have been Dr. Veit Wagner, Dr. Martin Zorn, Thomas Trepk, Florian Poser and Karsten Fleischer, who certainly wished for less users and more stable computer software.

. . . all other members of the Richter group, especially the former members Silvia Schintke, Thomas Trepk, Dr. Paul Kurpas, Frank Schienle, Timon Wehnert, but also to the current members Christoph Cobet, Kathy Lüdge, and Dr. Anne-Marie Frisch. Hey, without you and many others not mentioned (“Duracell”) there would have been only boring physics; no strange mensa-talk, no Heimbach-seminars, and no nice excursions. It was fun to work with you!

. . . the former PhD-students at the FHI, Dr. Carsten Setzer, Dr. Jutta Platen, Juan Mártinez, and Lutz Geelhaar for discussion about GaAs high-index surface, and also for a nice evening in Madrid.

. . . Dr. Lars Hofmann at the FBH for discussions and sharing results about MOVPE growth on (113) surfaces.

. . . the technical workshop and the glass blower of the institute of Festkörperphysik. After visiting some institutes I am quite happy, that here was such a good workshop.

. . . the many people, which had contributed on one way or the other. Be it moral and monetary support, like by my parents, or just my friends to help me to forget physics at the weekend and do sailing, scouting, . . .

E Curriculum Vitae

Name	Markus Pristovsek
Sex	Male
Birthday	9th June 1970 in Berlin-Wedding
Nationality	Germany and Austria
Status	Single

Since 1984 Divers activities in the Graue Jungenschaft (kind of scouting organisation), including working with children groups

Between 1985 and 1989 Delivering and charging of weekly television journals

23rd May 1989 Finished Abitur at the Gabriele-von-Bulow Oberschule (Gynasium)

17th July 1989 until 13th October 1989 Industrial Training at Siemens, Berlin (Required preparation for some course of studies). Earned skills in metalworking, welding and technical drawings.

3rd November 1989 Inscribed as a student of physics at the Technische Universität Berlin.

1st October 1991 Passed the Vordiplom (kind of bachelor degree) with the optional subject of astrophysics.

In 1992 Sold an editor program for the ATARI ST computer to the company BELA GmbH.

1th April 1993 until 31th September 1995 Work as a student tutor, first in the Grundpraktikum (fundamental experimental training), then for maintaining an MOVPE (MetalOrganic Vapor Phase Epitaxy) growth system.

1st November 1994 until 25th December 1994 Participant of an Atlantic Ocean crossing with a traditional square rigged sailship.

28th September 1995 Finished Diploma in Fundamental Physics (kind of master thesis) about *Wachstum und Passivierung von III/V Halbleitern in der MOVPE* (Growth and passivation of III/V semiconductor in MOVPE). Optinal subjects were solid state physics and astrophysics.

25th November 1995 until 31st December 1995 Worked for a project at BESSY (Berlin electron synchrotron).

Until end of March 1996 Contract work on a computer program for the analysis of optical spectra.

Since 1st April 1996 Start of my doctorate (PhD studies). Work on several positions, as project money allowed. Since 2nd December 1999 employed as a full position assistent with teaching assignment.

December 1998 Foundation of the company *3P Messsoftware Markus Pristovsek GbR* to sell our home-made Scanning Near-field Optical Mircoscopy system and software *snomputz*.

1st November 2000 Finishing of my doctorate (PhD thesis) and oral examination.

4th November 2001 till 30th March 2001 Working as a COE fellow at the National Research Institute for Metals in Tsukuba, Japan.